1   **Cretaceous tectonic evolution of the Neo-Tethys in Central Iran: Evidence from**

2   **petrology and age of the Nain-Ashin ophiolitic basalts**

3

4

5

6   Tahmineh Pirnia[1], Emilio Saccani[1], Ghodrat Torabi[2], Marco Chiari[3], Špela Goričan[4], Edoardo

7   Barbero[1]

8

9   [1] Department of Physics and Earth Sciences, Ferrara University, Ferrara 44122, Italy

10   [2] Department of Geology, Faculty of Science, University of Isfahan, Iran.

11   [3] CNR, Istituto di Geoscienze e Georisorse, Florence, Italy

12   [4] Paleontološki inštitut Ivana Rakovca ZRC SAZU, Ljubljana, Slovenia

13

14

15

16

17   Corresponding author: Tahmineh Pirnia, e-mail: tahmineh.pirnia@gmail.com

18

19

20

21

22

23

24

25   **Abstract**

26

27   The Nain and Ashin ophiolites consist Mesozoic mélange units that were emplaced in the

28   Late Cretaceous onto the continental basement of the Central-East Iran microplate (CEIM).

29   They largely consist of serpentinized peridotites slices; nonetheless, minor tectonic slices of

30   sheeted dykes and pillow lavas - locally stratigraphically associated with radiolarian cherts -

31   can be found in these ophiolitic mélanges. Based on their whole rock geochemistry and

32   mineral chemistry, these rocks can be divided into two geochemical groups. The sheeted

33   dykes and most of the pillow lavas show island arc tholeiitic (IAT) affinity, whereas a few

34   pillow lavas from the Nain ophiolites show calc-alkaline (CA) affinity. Petrogenetic modeling

35   based on trace elements composition indicates that both IAT and CA rocks derived from

36   partial melting of depleted mantle sources that underwent enrichment in subduction-derived

37   components prior to melting. Petrogenetic modeling shows that these components were

38   represented by pure aqueous fluids, or sediment melts, or a combination of both, suggesting

39   that the studied rocks were formed in an arc-forearc tectonic setting. Our new biostratigraphic

40   data indicate this arc-forearc setting was active in the Early Cretaceous. Previous tectonic

41   interpretations suggested that the Nain ophiolites formed, in a Late Cretaceous backarc basin

42   located in the south of the CEIM (the so-called Nain-Baft basin). However, recent studies

43   showed that the CEIM underwent a counter-clockwise rotation in the Cenozoic, which

44   displaced the Nain and Ashin ophiolites in their present day position from an original

45   northeastward location. This evidence combined with our new data and a comparison of the

46   chemical features of volcanic rocks from different ophiolites around the CEIM allow us to

47   suggest that the Nain-Ashin volcanic rocks and dykes were formed in a volcanic arc that

48   developed on the northern margin of the CEIM during the Early Cretaceous in association

49   with the subduction, below the CEIM, of a Neo-Tethys oceanic branch that was existing

50   between the CEIM and the southern margin of Eurasia. As a major conclusion of this paper, a

new geodynamic model for the Cretaceous evolution of the CEIM and surrounding Neo-

Tethyan oceanic basins is proposed.

Keywords: Ophiolite, Volcanic arc, Early Cretaceous, Nain, Ashin, Iran

1. Introduction

The geology of Iran is characterized by the outstanding occurrence of a number of

ophiolitic complexes (Fig. 1a). A few of them represent remnants of the Paleo-Tethys Ocean

and mainly crop out in northern Iran along the Alborz Range (Lensch and Davoudzadeh,

1982). However, most of the Iranian ophiolites are Mesozoic in age and record the complex

and long-lived geodynamic history of the different branches of the Neo-Tethys that developed

between the Arabian plate and the composite puzzle of microplates, which characterized the

southern margin of the Eurasian continent from Late Triassic to early Cenozoic (e.g.,

Desmons and Beccaluva, 1983; Sengör, 1990; Barrier and Vrielynck, 2008). The Iranian

Mesozoic ophiolites have classically been divided into three major belts (Stöcklin, 1974,

Lensch and Davoudzadeh, 1982) (Fig. 1a): 1) ophiolites of the Zagros suture belt representing

remnants of the Southern Neo-Tethys, which opened during the Triassic between the Arabian

plate and the Central Iran continental block (e.g., Robertson, 2007, and references therein); 2)

ophiolites of the Makran accretionary prism, which includes the incomplete ophiolitic

sequences and ophiolitic mélanges of Band-e-Zeyarat, Dar Anar, and Fanuj-Maskutan (e.g.,

McCall, 2002; Delavari et al., 2016; Saccani et al., 2017a); 3) ophiolites and ophiolitic

mélanges (the so called "Coloured Mélanges") that mark the boundaries of the Central-East

Iranian microcontinent (CEIM). These include the Sabzevar ophiolites in the north, the Nain,

Dehshir, Shahr-e-Babak, Baft ophiolites (or, simply, the Nain-Baft ophiolitic belt) in the

southwest, and the Sistan zone ophiolites in the east of the CEIM (e.g., Camp and Griffis,

1982; Ghazi and Hassanipak, 2000; Shojaat et al., 2003; Rahmani et al., 2007; Rossetti et al.,

2010; Shafaii Moghadam et al., 2009; Saccani et al., 2010; Angiboust et al., 2013; Omrani et

al., 2013; Rezaei et al., 2018). The Nain and Ashin ophiolites are of particular interest as they

crop out at the westernmost corner of the CEIM, which is marked in this area by the

intersection of two major regional-scale fault systems, namely, the Nain-Baft and the

Dorouneh (also known as Great Kavir-Dorouneh) fault systems (Fig. 1a). They consist of

ophiolitic mélange units ("Coloured Mélange") that were emplaced during Late Cretaceous-

lower Paleocene times onto the continental basement of the CEIM (Davoudzade, 1972;

Stöcklin, 1974; Stoneley, 1975). Several studies have been carried out on these ophiolites.

However, no general consensus still exists on their tectono-magmatic implication, and

different hypotheses have been suggested about the nature and geodynamic significance of the

oceanic branch in which they were formed. Some authors have indicated a supra-subduction

zone (SSZ) geochemical affinity for the Nain ophiolites, as well as for the neighbouring

Shahr-e-Babak ophiolites, and suggested that they were formed in an intra-oceanic island arc

setting during the Late Cretaceous (e.g., Ghazi and Hassanipak, 2000; Rahmani et al., 2007).

Geochemical studies on the mafic lavas of the Nain and Dehshir ophiolites (Shafaii

Moghadam et al., 2008, 2009), as well as on the mantle peridotites (Mehdipour Ghazi et al.,

2010; Pirnia et al., 2010) have suggested that the Nain-Baft ophiolites were originated in a

backarc basin, which opened between the Sanandaj-Sirjan zone and the CEIM in the Late

Cretaceous in response to the subduction of the Southern Neo-Tethys below the Sanandaj-

Sirjan block (see Takin, 1972; McCall, 2002; Shahabpour, 2005; Barrier and Vrielynck,

102   2008). However, a recent petrological study has suggested that mantle lherzolites in the Nain

103   ophiolites represent sub-continental mantle exhumed at an Iberia-type ocean-continent

104   transition zone (Pirnia et al., 2018) and a recent biostratigraphic study has shown that the

105   Ashin ophiolites are mid Cretaceous in age (Shirdashtzadeh et al., 2015). In addition, recent

106   paleomagnetic studies have shown that the CEIM underwent significant counter-clockwise

107   rotation of about 30° during the Late Jurassic - Early Cretaceous and again after the Middle–

108   Late Miocene (Mattei et al., 2012, 2014). As a consequence, it is reasonable to hypothesize

109   that the Nain and Ashin ophiolites were displaced in their present day position by the rotation

110   of the CEIM, implying that they were formed in an oceanic sector that was located during the

111   mid Cretaceous to the northeast with respect their current position. These recent studies show

112   robust evidence in contrast to the most accepted hypothesis of formation of the Nain and

113   Ashin ophiolites in the Nain-Baft backarc basin in the southwest of the CEIM (Barrier and

114   Vrielynck, 2008; Shafaii Moghadam et al., 2009). For this reason, we present new whole rock

115   geochemical and petrological data, as well as mineral chemistry data on sheeted dykes and

116   pillow lavas from the Nain and Ashin ophiolitic complexes with the aim of constraining their

117   petrogenetic processes and their tectono-magmatic setting of formation. We also present new

118   biostratigraphic data on radiolarian cherts stratigraphically associated with the studied pillow

119   lavas. These data will allow the type and age of the magmatic events to be constrained in

120   detail. Several models for the geodynamic evolution of the oceanic branches of the Neo-

121   Tethys that existed in Mesozoic times around the CEIM are available in literature (e.g.,

122   Shojaat et al., 2003; Barrier and Vrielynck, 2008; Shafaii Moghadam et al., 2009; Rossetti et

123   al., 2010; Omrani et al., 2013; Mattei et al., 2014; Shirdashtzadeh et al., 2015). Hence, one of

124   the main goals of this paper is to use our new data for testing and developing the extant

125   tectonic models. We anticipate that the data presented herein allow us to propose a new model

126   for the tectonic evolution of the CEIM and surrounding oceanic seaways during the

127   Cretaceous.

128

129

130   **2. Geological setting, field evidence, and sampling**

131

132   *2.1. General geological setting*

133

134   The Nain and Ashin ophiolites are located in the northeast of the Isfahan province in

135   Central Iran (Fig. 1a). These ophiolites are emplaced onto the westernmost corner of the

136   CEIM, which is defined in this area by the intersection of two major regional-scale fault

137   systems, namely, the Nain-Baft and the Dorouneh fault systems (Fig. 1a). These ophiolites

138   were classically considered as part of the Mesozoic, discontinuous ophiolitic belt that

139   surround the northern, western, and southern borders of the CEIM (Lensch and Davoudzadeh,

140   1982). In fact, this ophiolitic belt also includes the Sabzevar ophiolites, to the north and the

141   Dehshir and Baft ophiolites, to the southwest (Fig. 1a).

142   The Nain and Ashin ophiolitic complexes both consist of an ophiolitic mélange (also

143   known as "Coloured Mélange") including relics of the Mesozoic Neo-Tethys Ocean that were

144   emplaced onto the CEIM continental margin in Late Cretaceous-lower Paleocene (e.g.,

145   Davoudzadeh, 1972; Torabi et al., 2011a, b). The Nain and Ashin ophiolitic mélanges both

146   include very similar rock assemblages, and are formed by tectonic slices or blocks of different

147   types of ophiolitic and metaophiolitic rocks (Figs. 1b, c). Mantle peridotites largely prevail in

148   volume. They consist of serpentinites, harzburgites, and lherzolites generally showing a

149   marked foliation (Pirnia et al., 2010, 2013, 2014). Harzburgites locally include subordinate

150   amounts of dunites and podiform chromitites, as well as several dykes of pyroxenites,

151 wehrlites and rodingites (Davoudzadeh, 1972). Pirnia et al. (2018) have recently shown that

152 most lherzolites represent sub-continental type mantle, which is very similar to that cropping

153 out in the Alpine Tethys ophiolites. These authors have suggested that, similar to the Alpine

154 Tethys ophiolites (see Saccani et al., 2015), these lherzolites represent sub-continental mantle

155 exhumed, through an asymmetric passive extension, during the continental breakup that

156 preceded the oceanic formation.

157   Crustal rocks are very subordinate in volume. The scarce intrusive rocks are represented by

158 pegmatitic and isotropic gabbros, diorites, gabbronorites, always occurring as small-sized

159 bodies and dykes within the mantle peridotites. Plagiogranites, sheeted dykes (Fig. 2a) and

160 pillow lavas (Figs. 2b-d) are found as distinct slices in tectonic contact with the mantle

161 sequences. Pillow lavas are commonly stratigraphically covered by pelagic sedimentary

162 rocks, which clearly indicate that they were erupted in a sub-marine environment. These

163 pelagic sedimentary rocks are represented by radiolarian cherts (Figs. 2e, f) and Campanian-

164 Maastrichtian Globotruncana limestones (Davoudzadeh, 1972). All magmatic crustal rocks

165 underwent spilitization and sea floor metamorphisms (Torabi et al., 2008). Pillow lavas are

166 mostly found close to the sheeted dykes, but not in stratigraphic contact, in the western part of

167 the Nain ophiolites and in the eastern side of the Ashin ophiolites (Figs. 1b, c). In the Nain

168 ophiolites, they are discontinuously exposed along a N-S trend in the southwest of Soheyl-e-

169 Pakuh and near Separab (Rahmani et al., 2007) (Fig. 1b). The sheeted dyke complex cover an

170 area of about 5 km^2 and the thickness of single dykes ranges from 10 cm to 3 m (Rahmani et

171 al., 2007). Dykes locally cut high-level amphibole gabbros and plagiogranites. The pillow

172 lavas form thin individual tectonic slices that can reach up to 10 m in thickness. In the Ashin

173 ophiolite, sheeted dykes and pillow lavas crop out near Chah-e-Senjed (Fig. 1c). Similar to

174 the Nain ophiolite, pillow lavas slices are relatively thin; they reach ~25 m in thickness, on

175 average (Torabi, 2004). A K-Ar age of 98 Ma determined on plagiogranites (Sharkovski et al.,

176   1984) suggests a Cenomanian age for the formation of the intrusive rocks from the Ashin

177   ophiolite. In addition, $^{40}Ar/^{39}Ar$ ages ranging from 101.2 ± 0.9 to 99 ± 1.2 Ma have been

178   determined for one hornblende-gabbro (Hassanipak and Ghazi, 2000). Unfortunately, no

179   indication is given by these authors about the geochemical nature (i.e., subduction-related or

180   subduction-unrelated) of the dated gabbro.

181   In both ophiolitic mélanges, metaophiolitic rocks include metagabbros, metaplagiogranites,

182   amphibolites, banded metacherts, and successions of marbles and schists (Sharkovski et al.,

183   1984; Shirdashtzadeh et al., 2010). Shirdashtzadeh et al. (2010) and Torabi et al. (2011b)

184   suggested that the protholiths of the amphibolitic rocks from both Nain and Ashin ophiolites

185   were represented by diabasic dykes and basaltic pillow lavas both showing normal mid-ocean

186   ridge affinity (N-MORB). However, Shirdashtzadeh et al. (2011) also proposed an IAT

187   affinity for the amphibolites. According to these authors, metacherts and marble-schists

188   successions can be regarded as the original sedimentary cover of the pillow lava basalts.

189   Shirdashtzadeh et al. (2010) suggested that the metamorphic slices included within the Nain

190   and Ashin mélanges represent relics a Jurassic oceanic crust that underwent a Late Cretaceous

191   metamorphic event (Shafaii Moghadam et al., 2009).

192   Cenozoic volcanic rocks associated with small coeval dioritic intrusions, as well as

193   Cenozoic sedimentary rocks extensively crop out in both Nain and Ashin areas

194   (Davoudzadeh, 1972). However, in the Nain area, the volcanic and sedimentary rocks are

195   separated and crop out to the west and to the east of the ophiolitic mélange, respectively (Fig.

196   1b). In contrast, in the Ashin area, Cenozoic sedimentary rocks largely prevail and entirely

197   surround the ophiolitic mélange, whereas Cenozoic volcanic rocks locally crop out on the top

198   of the ophiolitic mélange, as well as to the east of the Tertiary sedimentary succession (Fig.

199   1c). In addition, in the Ashin area, Paleozoic metamorphic rocks, including metaophiolitic

200   rocks (Anarak Complex) largely crop out in the easternmost side (Zanchi et al., 2015; Berra et

201 al., 2017; Zanchetta et al., 2017) (Fig. 1c). It has been suggested that the emplacement of both

202 Nain and Ashin Mesozoic ophiolitic mélanges onto the CEIM occurred before Paleocene

203 times, since they are unconformably covered by Paleocene-Eocene sedimentary rocks

204 (Davoudzade, 1972). However, some authors suggested that their emplacement took place in

205 the Late Cretaceous (Stöcklin, 1974; Stoneley, 1975).

206 Rahmani et al. (2007) have suggested that the Nain sheeted dykes display island arc tholeiitic

207 (IAT) affinity and concluded that their formation is related to an intra-oceanic SSZ setting.

208 However, other authors suggested that ophiolitic rocks from both Nain and Ashin ophiolitic

209 mélanges were originated in a back-arc basin setting (e.g., Torabi et al., 2008; Shafaii

210 Moghadam et al., 2009; Pirnia et al., 2010, 2014).

211

212 *2.2. Field evidence and sampling*

213

214   Sampling was focused on the mafic sheeted dykes and pillow lavas cropping out as distinct

215 tectonic slices in the Nain and Ashin ophiolitic mélanges. Radiolarian cherts showing clear

216 stratigraphic contacts with pillow lavas have also been sampled in some localities in order to

217 constrain the age of the associated pillow lavas in detail.

218   In the Nain area (Fig. 1b), a total of four sheeted dyke, fourteen pillow lava, and six

219 radiolarian chert samples were collected from the ophiolitic mélange. Sheeted dykes were

220 sampled along the road from Separab to Soheyl-e-Pakuh. In this locality, dykes show variable

221 thickness, ranging from 0.5 to 3 m (Fig. 2a). They form a small (some tens of m) tectonic

222 slice juxtaposed onto a thick harzburgite slice. Pillow lavas were collected in some distinct

223 tectonic slices cropping out in the neighborhood of Soheyl-e-Pakuh, mainly in the northwest

224 of this village. In a couple of these tectonic slices, pillow lavas are stratigraphically covered

225 by radiolarian cherts. The thicknesses of these slices are difficult to be determined because

226 their boundary contacts are poorly exposed due to a widespread Quaternary sedimentary

227 cover. However, their thickness can be estimated to be from 10 to 50 m and they generally lie

228 onto the top of mantle peridotites. Pillow lavas commonly show spherical to elliptical shapes

229 (Fig. 2b), thought tubular and irregular shapes can also be seen. The interstitial spaces

230 between the pillows are often filled by hyaloclastite breccia (Fig. 2d) and, rarely, by

231 interpillow radiolarian cherts. The pillows are very variable in size, ranging from 0.2 to 2

232 meter in diameter. The pillow lava series are locally cross-cut by deeply altered individual

233 dykes of variable nature. In the tectonic slices consisting of pillow lava – radiolarian chert

234 sequences, the contact between pillow lava and overlying radiolarian cherts can be abrupt or

235 transitional depending on localities. The transitional contact is characterized by lenses and

236 patches of chert embedded in the top of the pillow lava series and vice versa by pillow lava

237 lenses embedded in the bottom of the radiolarian chert sequences. The radiolarian cherts are

238 characterized by a red-brownish colour. The radiolarian cherts generally show layering with

239 very variable thickness (1 – 5 cm) or massive bedding. The thickness of radiolarian chert

240 sequences ranges from 10 to 40 m. Radiolarian cherts were taken from both the tectonic slices

241 consisting of pillow lava – radiolarian chert sequences. In detail, radiolarian cherts NA424

242 and NA425 were stratigraphically associated with pillow lava sample NA421, whereas

243 radiolarian cherts NA501, NA502, NA503, and NA510 were associated with pillow lava

244 NA509.

245   In the Ashin ophiolite, a total of ten samples of pillow lavas, and three samples of

246 radiolarian cherts were taken from the ophiolitic mélange. Sheeted dykes where sampled in

247 small and tectonized outcrops. In fact, after preliminary petrographical and chemical analyses

248 they resulted totally altered and therefore they will not be treated in this paper. Pillow lavas

249 were collected in two distinct tectonic slices cropping out in the Chah-e-Senjed area (Fig. 1c)

250 where the best preserved outcrops are found. Pillow lavas show general features that are very

251 similar to those of pillow lavas in the Nain ophiolite (Fig. 2c). Similar to Nain ophiolite, the

252 thicknesses of the tectonic slices made up of pillow lava or pillow lava – radiolarian chert

253 sequences are difficult to be determined, but it can be estimated to be about 25 m for pillow

254 lavas and about 50 m for pillow lava – radiolarian chert sequences (Fig. 2e). These tectonic

255 slices are found onto the top of mantle peridotites. In the pillow lava – radiolarian chert

256 sequences, the contact between pillow lava and overlying radiolarian cherts are mainly

257 transitional. Interpillow patches of radiolarian chert are common (Fig 2f). The thickness of

258 radiolarian chert sequences range is about 25 m. The sampled radiolarian cherts AS1010,

259 AS1012/1, and AS1021 were stratigraphically associated with pillow lava sample AS1012.

260

261

262 **3. Radiolarian Biostratigraphy**

263

264   The radiolarian samples were etched with hydrochloric and hydrofluoric acid following the

265 method proposed by Dumitrica (1970), Pessagno and Newport (1972), Baumgartner et al.

266 (1981) and De Wever (1982). Unfortunately, some of them were barren or yielded

267 radiolarians with very poor preservation. Three samples were however suitable for

268 biostratigraphical analysis, thought two samples from the Nain ophiolite yielded

269 radiolarians with moderate preservation. The principal marker taxa are illustrated in Figure 3.

270 From the analysed cherts radiolarian assemblages and ages were obtained as follows.

271   Sample AS1010 contains a moderately well-preserved radiolarian assemblage dominated

272 by nassellarians. All identified species are illustrated in Figure 3. Age determination is

273 primarily based on the zonation proposed by O'Dogherty (1994) and we mostly followed his

274 systematics for determination of species. The names of genera are updated according to more

275 recent publications (O'Dogherty et al., 2009, 2017).

276   The sample is assignable to UA 10 of the Romanus Subzone, the lower subzone of the

277   Spoletoensis Zone. This assignment is constrained with the first occurrence of *Mita gracilis*

278   (Squinabol) and the last occurrence of *Crococapsa asseni* (Tan). The Romanus Subzone is

279   calibrated to the Middle Albian but we also note that the Early to early Middle Albian is not

280   recorded in this zonation (see Fig. 10c and Fig. 11 in O'Dogherty, 1994). The first occurrence

281   of *Mita gracilis* (Squinabol) was later determined at the base of the Albian (Danelian, 2008).

282   Based on these ranges, the inferred age for sample 1010 is Early–Middle Albian.

283   Samples NA424 and NA510 contain very few radiolarians determinable only at genus

284   level. Both samples contain the genus *Dictyomitra*, which first appears in the Berriasian

285   (O'Dogherty et al., 2009). The samples indicate the Cretaceous but a more precise age

286   assignment is not possible.

287

288

289   **4. Petrography of the sheeted dykes and pillow lavas**

290

291   Most of the rocks studied in this paper are affected by various degrees of low-grade ocean-

292   floor hydrothermal alteration, which resulted in different extent of replacement of the primary

293   igneous phases. However, regardless of the extent of mineralogical alteration, the primary

294   igneous textures are always well preserved. Olivine is never preserved, and it is always

295   replaced by iddingsite and/or chlorite. Fresh plagioclase is very rare, since it is usually

296   replaced by albite and calcite. Clinopyroxene alteration normally occurs as pseudomorphic

297   replacement by chlorite or actinolitic amphibole; however, some samples display fresh

298   clinopyroxene relics as both phenocrysts and groundmass minerals. Volcanic glass in the

299   groundmass has been altered into an assemblage of chlorite and prehnite. Few samples exhibit

300   variolitic textures, with varioles filled by calcite and, subordinately, by chlorite and zeolite. In

301 addition, small calcite veins are frequent. Regardless of the secondary mineralogical

302 transformations, the following petrographic description will be made on the bases of the

303 primary igneous phases.

304

305 *4.1. Nain Pillow lavas*

306

307 Samples from NA400 to NA421 are olivine-basalt in composition, whereas sample NA509

308 is represented by a ferrobasalt. All these rocks belong to the geochemical Group 1, as will be

309 defined in Section 6.2. Olivine-basalts show porphyritic, hypoialine textures with

310 phenocrysts and microphenocrysts mainly represented by olivine (Fig. 4a) and plagioclase.

311 Some samples display glomeroporphyritic texture with clusters made up of 3 - 4 plagioclase

312 phenocrysts. Olivines form euhedral crystals, which often contain inclusions of glass

313 (completely altered) and/or chromian spinel. Plagioclase phenocrysts commonly show albite-

314 carlsbad twinning. The groundmass mainly shows hypoialine, intersertal textures with

315 plagioclase laths and intergranular clinopyroxene, glass, and minor opaque minerals. (Fig.

316 4a). In samples NA229 and NA230 (i.e. the samples belonging to the geochemical Group 2,

317 as defined in Section 6.3) olivine is absent and the phenocryst assemblage is composed of

318 plagioclase and plagioclase + clinopyroxene, respectively (Fig. 4b). In all samples, the

319 groundmass shows intersertal and subophitic texture with plagioclase, clinopyroxene, altered

320 glass, chromian spinel, and minor opaque minerals. The chromian spinels often contain

321 inclusions of altered silicate minerals. The groundmass of sample NA230 show fluidal

322 texture marked by the alignment of plagioclase laths.

323

324 *4.2. Nain sheeted dykes*

325

326   Nain sheeted dykes are basalt and basaltic andesite in composition. They show

327   intergranular texture and are mainly composed of plagioclase, altered clinopyroxene and

328   hornblende (Fig. 4c). Minor amounts of quartz, Fe-Ti oxides and sulfides are in interstitial

329   position between the major rock-forming minerals. Small apatite crystals occasionally occur

330   as inclusions within plagioclases.

331

332   *4.3 Ashin pillow lavas*

333

334   Ashin pillow lavas range in composition from olivine-basalt to basaltic andesite. They

335   show porphyritic to vitrophyric textures similar to those of the Nain pillow lavas.

336   Phenocrysts and microphenocrysts are mainly represented by olivine, plagioclase, and

337   clinopyroxene. The groundmass is intergranular, hypoialine in texture and is composed of

338   plagioclase laths, granular clinopyroxene, altered glass, chromian spinel, and Fe-Ti oxides.

339   Locally, the groundmass also includes sulfide minerals. Samples AS1007/2 and AS1008 also

340   include minor amounts of primary hornblende as microphenocrysts. The chromian spinel is

341   commonly represented by coarse-grained, euhedral crystals with inclusions of silicate

342   minerals (Fig. 4d).

343

344

345   **5. Analytical methods**

346

347   Whole-rock major and some trace element were analyzed by X-ray fluorescence (XRF) on

348   pressed-powder pellets, using an ARL Advant-XP automated X-ray spectrometer. The matrix

349   correction methods proposed by Lachance and Traill (1966) were applied. Volatile contents

350   were determined as loss on ignition (L.O.I.) at 1000°C. In addition, Rb, Sr, Zr, Y, Nb, Hf, Ta,

351 Th, U, and the rare earth elements (REE) were determined by inductively coupled plasma-

352 mass spectrometry (ICP-MS) using a Thermo Series X-I spectrometer. The results are shown

353 in Table 1. However, for the discussion of the geochemical characteristics major element

354 composition has been re-calculated on L.O.I.-free bases. The accuracy of the data for XRF

355 and ICP-MS analyses were evaluated using results for international standard rocks run as

356 unknown. The detection limits for XRF and ICP-MS analyses were evaluated using results

357 from several runs of twenty-nine international standards. Results are given in Appendix A1.

358 All whole-rock analyses were performed at the Department of Physics and Earth Science,

359 University of Ferrara.

360   Major element compositions of mineral phases were determined by electron microprobe

361 spectrometry using a JEOL JXA8200 Superprobe at Leoben University, Austria. An

362 accelerating voltage of 15 kV and a beam current of 10 nA were applied for 25 seconds

363 counting interval, whereas the beam spot size was ~5 μm. The obtained major element results,

364 corrected by an on-line ZAF program, are shown in Tables 2 to 4.

365

366

367 **6. Whole rock chemistry of sheeted dykes and pillow lavas**

368

369 *6.1. Evaluation of the alteration effects*

370

371   The geochemical features of the Nain and Ashin pillow lavas and dykes are described

372 using basically those elements that are virtually immobile during low-temperature alteration

373 and metamorphism. They include some incompatible trace elements (e.g., Ti, P, Zr, Y, Sc,

374 Nb, Ta, Hf, Th), middle REE (M-REE) and heavy REE (H-REE), as well as some transition

375 metals (e.g., Ni, Co, Cr, V). Large ion lithophile elements (LILE) and many major elements

376   are commonly mobilized during alteration (e.g., Pearce and Norry, 1979). In addition, light

377   REE (LREE) may also be affected to some degree of mobilization induced by alteration (e.g.,

378   Valsami and Cann, 1992). Some mobility tests were therefore made for SiO_2, Al_2O_3, FeO,

379   CaO, Na_2O, K_2O, Ba, Rb, Sr, Pb, U, La, and Ce by plotting these elements versus some

380   immobile elements (e.g., Zr, Y) and then by calculating the correlation coefficients (r^2) for

381   samples from the different rock-types. These tests indicate that La (e.g., r^2 vs. Zr = 0.73 -

382   0.93), Ce (e.g., r^2 vs. Y = 0.82 - 0.99), and Ba (e.g., r^2 vs. Y = 0.67 - 0.88) show good

383   correlation with immobile elements suggesting that the amount of mobilization of these

384   elements was limited. Al_2O_3 (r^2 vs. Y = 0.55 - 0.72) resulted moderately mobilized in all the

385   studied samples. In consequence, this element can be used, thought with some caution. Tests

386   on SiO_2, FeO, CaO, Na_2O, and U returned different results depending on the rock-type. SiO_2,

387   Na_2O, and U were little mobilized in samples from the Ashin pillow lavas and Nain sheeted

388   dykes (r^2 vs. Y > 0.75, > 0.80, and > 0.72 for SiO_2, Na_2O, and U, respectively), whereas these

389   elements were mobilized in samples from the Nain pillow lavas (r^2 vs. Y = 0.28, = 0.45, and =

390   0.11, respectively). FeO and CaO contents show good correlation with immobile elements for

391   pillow lava samples from both the Nain and Ashin (e.g., r^2 for FeO vs. Y = 0.77-0.92 and r^2

392   for CaO vs. Y = 0.75-0.82). In contrast, these elements resulted fairly mobilized in samples

393   from the Nain sheeted dykes (e.g., r^2 for FeO vs. Y = 0.24 and r^2 for CaO vs. Y = 0.48). K_2O

394   (r^2 vs. Y < 0.48), Rb (r^2 vs. Y < 0.23), Pb (r^2 vs. Y < 0.36), and Sr (r^2 vs. Y < 0.22) contents

395   resulted affected by high degrees of alteration-induced mobilization and therefore these

396   elements cannot be used. The results obtained from the mobility tests carried out on the

397   studied rocks are in agreement with previous works, which show that alteration of arc

398   lithosphere by seawater or hydrothermal fluids increases the content of volatiles and trace

399   elements, such as K, Rb, U, Pb, and Sr (e.g., Kelley et al., 2003).

400

401   *6.2. Group 1 basaltic rocks*

402

403   Group 1 rocks is represented by pillow lavas from both Nain and Ashin ophiolites, as well

404   as by the Nain sheeted dykes. Group 1 pillow lavas from both Nain and Ashin pillow lava

405   series show similar compositions and therefore they will be treated together in the following

406   description. They are mainly represented by basalts, though one sample (NA509) showing

407   ferrobasaltic composition and one sample (AS1012) showing basaltic andesitic composition

408   are found in the pillow lava series of the Nain and Ashin ophiolites, respectively (Table 1). In

409   basalts, SiO_2 contents range between 45.88 and 50.94 wt.% and Mg# range between 74.5 and

410   55.9, whereas in the ferrobasalt Mg# is low (40.7). The basaltic andesite shows comparatively

411   higher fractionation degree with SiO_2 = 54.39 wt.% and Mg# = 30.1. These rocks display a

412   sub-alkaline, tholeiitic nature exemplified by generally low Nb/Y ratios (Fig. 5), as well as by

413   sharp Ti, Fe, P_2O_5, Sc, and V increase from basalt to ferrobasalt followed by a significant

414   decrease in the basaltic andesite (Fig. 6). Basalts are characterized by variable, but generally

415   low TiO_2 (0.60-1.05 wt.%), P_2O_5 (0.03 - 0.20 wt%), Zr (37-78 ppm) and Y (13 - 24 ppm)

416   contents. Compatible element contents are very variable (e.g., Cr = 352 - 619 ppm).

417   Nonetheless, these elements generally show high contents in most samples (Table 4). The

418   ferrobasaltic sample obviously show very high FeO_{tot} (17.74 wt.%), TiO_2 (3.06 wt.%), and V

419   (807 ppm) contents. Normal-type MORB (N-MORB) normalized spiderdiagrams (Figs. 7a, c)

420   display incompatible element patterns with a slight Th relative enrichment and marked Ta and

421   Nb negative anomalies. High-field-strength element (HFSE) abundance is generally low

422   ranging from 0.3 to 3 times N-MORB composition (Sun and McDonough, 1989). Most

423   samples show REE patterns slightly increasing from LREE to HREE, whereas a few samples

424   show almost flat patterns (Figs. 7b, d) as testified by the $(La/Sm)_N$ and $(La/Yb)_N$ ratios (0.54-

425   0.98 and 0.50-1.14, respectively).

426 Group 1 rocks from the sheeted dykes of the Nain ophiolites show chemical features that

427 are similar to those of Group 1 pillow lavas, though some minor differences can be observed.

428 They are represented by basalts and basaltic andesites (Table 1), with SiO_2 contents ranging

429 between 50.55 and 52.61 wt.%. Similar to pillow lava samples, these rocks display a sub-

430 alkaline nature with low Nb/Y ratios (Fig. 5). They show uniform chemical composition

431 (Table 1), as exemplified by the quite restricted range of variation of the Mg# values (66.2 -

432 61.9). Group 1 sheeted dykes are characterized by low TiO_2 (0.63-0.69 wt.%), P_2O_5 (0.06-

433 0.09 wt%), Zr (27-39 ppm), and Y (12-15 ppm) contents. Compatible element contents are

434 generally low (e.g., Cr = 38-117 ppm) and comparatively lower, at comparable MgO

435 contents, with respect to those observed in pillow lavas (Table 1). N-MORB normalized

436 spiderdiagrams display incompatible element patterns with a slight Th relative enrichment

437 and Ta and Nb negative anomalies (Fig. 7e). In particular, the Th relative enrichment ($Th_N =$

438 2.35 − 3.90) is higher compared to that of Group 1 pillow lava basaltic rocks ($Th_N = 1.06 −$

439 2.03). HFSE abundance is generally low ranging from 0.3 to 0.9 times N-MORB composition

440 (Sun and McDonough, 1989). Chondrite-normalized REE abundance show either patterns

441 slightly depleted in LREE compared to HREE ($La_N/Yb_N = 0.80$) or slightly enriched in LREE

442 compared to HREE ($La_N/Yb_N = 1.14$) (Fig. 7f).

443 The overall geochemical features of Group 1 rocks from both Nain and Ashin pillow lavas

444 and Nain sheeted dykes are similar to those of IAT from many ophiolitic complexes, as

445 exemplified by the incompatible elements and REE concentrations (see Figs. 7g, h for a

446 comparison). Based on Th-Co co-variation, Group 1 rocks can be classified as IAT (Fig. 8).

447 Accordingly, in the discrimination diagrams in Figure 9a they plot in the field for IAT rocks

448 forming in volcanic arc settings with no significant contribution from polygenetic crust (Fig.

449 9b).

450

451   *6.3. Group 2 basaltic rocks*

452

453   Group 2 rocks include only a couple of samples from the Nain pillow lavas series. They

454   are represented by basalts with SiO_2 contents ranging from 50.04 to 51.83 wt.%, whereas

455   Mg# range from 68.4 to 49.6. These rocks display sub-alkaline nature as testified by low

456   Nb/Y ratios (Fig. 5). Ti and Fe show a mild increase with decreasing Mg# (Fig. 6). Although

457   generally low, TiO_2 (0.90-0.96 wt%) and Y (15-25 ppm) contents are comparatively higher

458   than those observed in Group 1 rocks. In contrast, P_2O_5 (0.15-0.24 wt.%) and Zr (107 - 136

459   ppm) contents are significantly higher than those of Group 1 rocks. Compatible element

460   contents (Table 1) are very low (e.g., Ni < 12 ppm, Cr = 17-77 ppm). The incompatible

461   element abundance (Fig. 7i) exhibits patterns, which are very similar to those of calc-alkaline

462   (CA) basalts (e.g., Pearce, 1983) with marked positive anomalies in Th, U, La, and Ce, and

463   negative anomalies in Ta, Nb, and Ti. The chondrite-normalized REE abundances (Fig. 7j) of

464   the Group 2 pillow lavas have sub-parallel patterns, regularly decreasing from LREE to

465   HREE. The enrichment in LREE compared to HREE is rather uniform with $(La/Yb)_N$ ratios

466   ranging from 3.19 to 4.33. La generally varies from ~26 to ~60 times chondrite abundance.

467   The incompatible elements and REE patterns (Figs. 7i, j) are consistent with a CA affinity for

468   these rocks (see Figs. 7g, h for a comparison). In fact, Group 2 rocks plot in the field for CA

469   basalts and basaltic andesites in the Th-Co diagram (Fig. 8). Accordingly, these samples plot

470   in the field for CA basalts (Fig. 9a) formed at continental margin volcanic arc (Fig.9b).

471

472

473   **7. Mineral chemistry and geothermobarometry**

474

475   Unfortunately, due to alteration effects, many of the studied samples were not suitable for

476   electron microprobe analysis. In addition, in most of the analyzed samples, only one type of

477   mineral phase was fresh enough to be analyzed, whereas only very few samples included two

478   or three different types of fresh mineral phases. Nonetheless, we performed mineral chemistry

479   analyses on a total of twelve samples for determining the compositions of clinopyroxene, Cr-

480   spinel, plagioclase and amphibole. Most of the analyzed plagioclase showed, however, albite-

481   oligoclase composition clearly reflecting a severe alteration of this mineral. Only in a couple

482   of samples from the Nain pillow lava series (samples NA403 and NA404) few plagioclase

483   crystals resulted relatively fresh, ranging in composition from labradorite to bytownite.

484   However, the number of reliable plagioclase analyses is very limited and therefore this

485   mineral will not be discussed in this work.

486

487   *7.1. Clinopyroxene*

488

489   Fresh primary clinopyroxenes crystals were found in samples of Group 1 and Group 2

490   pillow lavas from both Nain and Ashin ophiolites, whereas no fresh crystals were found in

491   Group 1 rocks from the Nain sheeted dykes. Representative analyses of fresh clinopyroxene

492   crystals are given in Table 2. Clinopyroxenes in Group 1 pillow lavas from both Nain and

493   Ashin ophiolites show augitic composition, according to the classification of Morimoto

494   (1989). No significant chemical differed can be seen between clinopyroxenes from

495   samples from the Nain and Ashin Group 1 pillow lavas and therefore these samples will be

496   described together in the following discussion. Clinopyroxenes from Group 1 rocks are

497   characterized by low TiO_2 (0.21-0.48 wt.%) and Na_2O (0.19-0.29 wt.%) contents, whereas

498   Mg# are relatively high (77.2-87.1). Cr_2O_3 contents are rather low, ranging from 0.03 to 0.09

499   wt.% in most samples. However, comparatively higher values can be seen in sample NA400,

500   where Cr_2O_3 content varies from 0.12 to 0.16 wt.%). The Ti/Al ratio is assumed to vary as a

501 function of the Ti-Al substitution in pyroxene, which, in turn, is strongly controlled by the

502 magma composition. Ti/Al ratios displayed by clinopyroxenes from Group 1 basalts are

503 generally very low (0.05-0.10). In these minerals, no definite correlations between Mg# and

504 Ti, Na and Al are observed. Only clinopyroxenes in sample NA403, which shows the highest

505 whole rock Mg#, display the lowest Ti and Na contents when compared to other

506 clinopyroxenes (Table 2). In contrast, Ti and Na contents are positively correlated in all

507 samples.

508 Clinopyroxenes from Group 2 basalts from the Nain pillow lava series are augitic in

509 composition (Morimoto, 1989). Compared to clinopyroxenes from Group 1 basalts, they

510 show higher TiO_2 (0.46-0.61 wt.%) and Na_2O (0.36-0.42 wt%) contents (see Table 2).

511 Accordingly, their Ti/Al ratios are generally higher than those observed in clinopyroxenes

512 from Group 1 rocks, ranging from 0.10 to 0.12. However, Mg# (82.4-84.0) and Cr_2O_3

513 contents (0.04-0.12 wt.%) show values perfectly overlapping those observed in

514 clinopyroxenes from Group 1 rocks (Table 2). In contrast to what observed for

515 clinopyroxenes from Group 1 basalts, Ti, Na and Al are negatively correlated with increasing

516 Mg#.

517 It is commonly accepted that clinopyroxene compositions represent a suitable indicator of

518 the magmatic affinity of basalts from different tectonic settings, as well as from different

519 ophiolitic types (e.g., Leterrier et al., 1982; Beccaluva et al., 1989). In fact, the chemical

520 composition of clinopyroxenes, beside to be controlled by crystal-chemical constrain, is also

521 strongly influenced by the composition of magmas from which they crystallize. Using Ti–

522 (Ca+Na), (Ti+Cr)–Ca, and Al-Ti covariation diagrams of Leterrier et al., (1982)

523 clinopyroxenes from Group 1 pillow lavas plot in the fields for tholeiitic-type volcanic arc

524 basalts (Fig. 10). Accordingly, in the TiO_2-SiO_2-Na_2O discrimination diagram of Beccaluva et

525 al. (1989) they plot in the fields for volcanic arc tholeiites (not shown). In contrast,

526 clinopyroxene from Group 2 pillow lavas plot in the field for CA basalts in the diagram in

527 Figure 10.

528

529 *7.2. Spinel*

530

531   Fresh primary chromian spinels were found in samples of Group 1 pillow lavas from both

532 Nain and Ashin ophiolites. In contrast, no spinels were found in Group 2 basalts and in the

533 Nain sheeted dyke series. Representative analyses of chromian spinels are given in Table 3.

534 Chromian spinels occurring in pillow lava basalts from the Nain and Ashin ophiolites show

535 quite similar chemical compositions (Table 3) and therefore they will be hereafter described

536 as a whole. In the Cr-Al-Fe^{3+} classification diagram (Stevens, 1944), spinels can be classified

537 as Al-chromites (not shown). They are characterized by 1:1 replacement of chromite end-

538 member [Fe(Cr, Fe^{3+})$_2$O$_4$] by the spinel end-member [MgAl$_2$O$_4$]. The proportions of these

539 two end-members range from 1.2 spinel - 1.8 chromite to 1.4 spinel - 1.6 chromite. These

540 minerals are characterized by variable, but generally low Al$_2$O$_3$ contents (16.44-23.70 wt.%)

541 and moderate Cr$_2$O$_3$ contents (42.08-50.21 wt.%). As a consequence, the Cr# is fairly high

542 (54.63-66.83, Fig. 11). MgO contents are relatively low (10.07-12.94 wt.%), whereas FeO

543 contents are relatively high (19.86-23.85 wt.%). TiO$_2$ contents, though generally low, are

544 highly variable, as they range from 0.16 to 0.56 wt.%. The lowest TiO$_2$ contents are observed

545 in spinels from most samples of the Nain pillow lava series (TiO$_2$ = 0.16-0.35 wt.%). In

546 contrast, spinels in the Ashin pillow lava basalts, as well as in sample NA421 (Nain pillow

547 lava series) show comparatively higher TiO$_2$ contents (TiO$_2$ = 0.35-0.56 wt.%). Individual

548 grains commonly show little compositional variation from core to rim. In most samples,

549 spinels have cores slightly richer in Cr$_2$O$_3$ and Al$_2$O$_3$ than the rims (Table 3). In these

550 samples, Cr$_2$O$_3$ and Al$_2$O$_3$ contents in core are less than ~4 relative percent higher than in rim.

551   Spinels from many samples show MgO, FeO, and TiO_2 contents that are slightly increasing

552   from cores to rims.

553   It is commonly recognized that the chemical composition of chromian spinel is a sensitive

554   petrogenetic indicator. Indeed, experimental studies have indicated that Al_2O_3 and TiO_2

555   contents in chromian spinel are strictly controlled by the contents of these elements in the

556   parental melt (e.g., Maurel and Maurel, 1982; Kamenetsky et al., 2001; Rollinson, 2008). In

557   many cases, the chemical composition of chromian spinels has been used for inferring the

558   parental melt composition (e.g., Kepezhinskas et al., 1993; Zhou et al., 1996; Kamenetsky et

559   al., 2001; Rollinson, 2008; Allahyari et al., 2014; Saccani and Tassinari, 2015). In fact,

560   Maurel and Maurel (1982) have proposed an empirical formula for calculating the Al_2O_3

561   content of the parental melt starting from the Al_2O_3 content in spinel. Similarly, Rollinson

562   (2008) proposed some empirical formulae that relate the Al_2O_3 and TiO_2 content of chromian

563   spinels and in parental melts. In this study, we use the empirical formulae proposed by

564   Rollinson (2008) in order to verify if chromian spinels have crystallized in equilibrium with

565   the liquid composition of their host rocks. Results are shown in Table 3. The calculated Al_2O_3

566   contents in the liquids are, on average, from 0.5 to 1 wt.% higher than those observed in the

567   whole rocks for all samples from the Nain pillow lavas and from sample AS1009 from the

568   Ashin pillow lavas, whereas in the other basalts from the Ashin ophiolites the calculated

569   Al_2O_3 contents are, on average, from 0.4 to 0.7 wt.% lower than those observed in the whole

570   rocks (Table 3). In general, the differences between calculated and observed Al_2O_3 values are

571   little and are included within the uncertainty of the methods. Therefore, we can conclude that

572   both Al_2O_3 and TiO_2 contents calculated from spinel compositions are very similar to those

573   observed in the parental rocks. In fact, the differences between calculated and observed TiO_2

574   contents range from 0 to 0.04 wt.% for all samples (Table 3). In summary, the close similarity

575   between calculated and observed Al_2O_3 and TiO_2 contents suggests that chromian spinels

576   have crystallized in equilibrium with the composition of their host rocks. Therefore, their

577   compositions can be plotted in the discrimination diagram in Figure 11, where it can be seen

578   that chromian spinels from both Nain and Ashin pillow lavas show quite similar compositions

579   and plot within or close to the field for island arc tholeiitic spinels.

580

581   *7.3. Amphibole*

582

583   Fresh primary amphiboles were found in few samples of Group 1 rocks in sheeted

584   dykes and pillow lavas from the Nain and Ashin ophiolites, respectively. Chemical

585   compositions of representative fresh amphiboles are given in Table 3. All amphiboles

586   have Ca > 1.50, (Na+K) < 0.5, Si included between 6.5 and 7.5, and $[Mg/(Mg+Fe^{2+})] >$

587   0.5 (Table 4) and thus they classify as magnesio-hornblende (Leake et al., 1997).

588   Compositional variation for the analysed amphiboles shows smooth correlation with

589   increasing differentiation (Table 4). This correlation is exemplified by the variation in

590   Mg#, which are 84.9-93.2 in basalts, and 78.8-83.9 in the basaltic andesite. (Na_2O+K_2O)

591   contents are slightly lower in amphiboles in basalts (0.59 – 0.99 wt.%) than in those in the

592   basaltic andesite (1.14-1.84 wt.%). Likewise, the TiO_2 content in amphiboles from the

593   Nain sheeted dyke series is comparatively lower in basalt (0.36-0.68 wt.%) than in the

594   basaltic andesite (0.59-1.14 wt.%). However, the TiO_2 content in amphiboles from these

595   samples is lower than that of amphiboles from the Ashin pillow lavas series, where it

596   ranges from 1.11 to 2.18 wt.%. Amphiboles from the Nain sheeted dyke series are

597   chemically zoned. In fact, TiO_2, Na_2O, and K_2O contents significantly increase from cores

598   to rims (Table 4).

599

600   *7.4. Geothermobarometers*

601

602   Due to the limited occurrence of fresh mineral phases, the geothermobarometers based

603   on clinopyroxene composition and the geobarometers based on amphibole composition

604   are the only methods that can be used for estimating crystallization temperatures and

605   pressures for the studied rocks. In fact, we applied the thermobarometric methods

606   proposed by Putirka et al. (2003) and Putirka (2008) based on clinopyroxene–whole rock

607   equilibrium for estimating crystallization temperatures and pressures of the pillow lavas

608   from both Nain and Ashin ophiolites, as only these rocks included fresh clinopyroxenes.

609   Results are shown in Table 2. Unfortunately, no fresh clinopyroxene is preserved in the

610   sheeted dyke basaltic rocks and therefore the temperature of crystallization of these rocks

611   cannot be estimated. Using the method proposed by Putirka (2008), the estimated

612   magmatic temperatures for both Group 1 and Group 2 basalts from different localities are

613   similar and range from $1195 \pm 3°C$ to $1224 \pm 8°C$. Interestingly, the estimated

614   crystallization pressures vary depending on both rock group and locality. The estimated

615   crystallization pressures for the Nain pillow lavas range from 0.22 ± 0.05 to 0.29 ± 0.06

616   GPa. Relatively higher pressures were estimated for the Group 1 Ashin pillow lavas, being

617   in the range $0.52 – 0.54 \pm 0.01$ GPa. However, the highest pressures were estimated for

618   the Group 2 pillow lavas from the Nain pillow lavas ($P = 0.61 \pm 0.03$ GPa).

619   The magmatic pressure of formation of the Nain sheeted dykes and one pillow lava

620   basalt from the Ashin ophiolites were also calculated using different methods based on the

621   Al-content in amphibole (Hammarstrom and Zen, 1986; Hollister et al., 1987; Johnson and

622   Rutherford, 1989). Results are shown in Table 4. Though these methods were calibrated

623   for different temperature ranges, they gave similar estimated pressures for the analyzed

624   magnesio-hornblendes (see Table 4). The estimated pressures for the Nain sheeted dykes

625   are in the range of $0.20 \pm 0.05 - 0.27 \pm 0.05$ GPa for both basalt and basaltic andesite. No

626   significant differences between pressures estimated from crystal cores and rims were

627   observed. In contrast, the estimated pressures of crystallization for amphiboles in the

628   Ashin pillow lava basalts are comparatively higher, being in the range of 0.51 – 0.52 GPa.

629   Sample AS1007/2 from the Ashin pillow lava series is the only sample in which both fresh

630   clinopyroxenes and amphiboles can be found. Therefore, a comparison of the

631   crystallization pressures estimated using these minerals can be made. For this sample,

632   pressures estimated using amphibole composition (0.42 – 0.55 GPa) are very similar to

633   those estimated using clinopyroxene composition (0.52 GPa). According to these

634   calculations, clinopyroxenes in Group 1 Nain pillow lavas were generated in magma

635   chamber(s) at depths ranging from ~8 to ~11 km, whereas in similar rocks from the Ashin

636   ophiolites clinopyroxenes and amphiboles crystallized at about 19 km depth. In contrast,

637   clinopyroxenes from in Group 2 pillow lavas from the Nain ophiolites crystallized in

638   magma chamber(s) located at ~23 km depth. Crystallization pressures estimated from

639   amphiboles suggest that the Group 1 Nain sheeted dykes were formed at ~8 km depth.

640

641   **8. Discussion**

642

643   *8.1. Melt petrogenesis and mantle sources*

644

645   According to many authors (e.g., Pearce and Norry, 1979; Pearce, 1983), the incompatible

646   element composition of basaltic rocks largely depends on the composition and degree of

647   melting of the associated mantle source, whereas it is little influenced by fractional

648   crystallization (e.g., Pearce, 1983). The trace element composition of different magma-types

649   is therefore primarily related to different source characteristics that are associated, in turn,

650   with distinct tectono-magmatic settings of formation. It follows that the chemical

651   characteristics of the different rock-types forming the volcanic and sheeted dyke series of the

652   Nain and Ashin (hereafter, Nain-Ashin) ophiolites can be used for determining the nature and

653   tectonic significance of the magmatic events that occurred in the oceanic sectors of the Neo-

654   Tethys, which surrounded the CEIM. We will therefore focus our petrogenetic discussion to

655   the identification of the possible mantle sources and related tectonic setting of formation of

656   the different rock-groups forming the sheeted dyke and pillow lava units cropping out in the

657   Nain-Ashin ophiolites. Some trace elements contents (e.g., Nb, Th, and REE) and their degree

658   of depletion or enrichment, as well as trace element ratios (e.g., Nb/Yb, Th/Ta, Th/Nb, Ba/Th)

659   are moderately affected by fractional crystallization of predominantly olivine + clinopyroxene

660   + plagioclase. Therefore, in presence of moderate amounts of fractionation, they are believed

661   to represent the elemental ratios in the source (e.g., Allègre and Minster, 1978; Beker et al.,

662   1997). For this reason, the following discussion will be based on the relatively less

663   fractionated basalts and basaltic andesites of the different magmatic groups. Figure 9a shows

664   that Group 1 (IAT) and Group 2 (CA) rocks plot in the fields for volcanic arc basalts and

665   show variable extents of Th enrichment relative to Nb, which suggest variable addition of

666   subduction-derived components. These rocks are commonly interpreted as originating from

667   partial melting of sub-arc residual peridotites that experienced Nb and Ti depletion during

668   previous partial melting events followed by Ba, Th, and LREE enrichment carried by

669   subduction-derived fluids or melts (e.g., Pearce, 1982, 1983; Gribble et al., 1996; Parkinson

670   and Pearce, 1998). Pearce and Norry (1979) and Beccaluva et al. (1989) suggested that low Ti

671   contents in clinopyroxenes reflect a depleted nature of the mantle source(s) that generated the

672   clinopyroxene parental magma. The generally low Ti content in clinopyroxenes from both

673   Group 1 and Group 2 pillow lavas (Table 2) also support the hypothesis that they crystallized

674   from primary magmas generated from mantle sources, which underwent Ti removal by

675   previous partial melting events (e.g., Hébert and Laurent, 1990).

676   A method that is commonly used for estimating the degree of depletion (i.e., degree of

677   melting) of the mantle source(s) is to plot a compatible versus an incompatible element. In

678   fact, compatible element abundance is not significantly modified during the progressive

679   mantle source depletion, whereas the abundance of incompatible elements is closely related to

680   source depletion and degree of melting (Pearce, 1982; 1983). We therefore use the Cr vs. Y

681   diagram (Pearce, 1983, Murton, 1989) shown in Figure 12 for inferring the composition of

682   mantle sources and the degrees of partial melting generating Group 1 and Group 2 rock-types.

683   In this Figure, two possible mantle sources are assumed: 1) a depleted mantle lherzolite,

684   which represents residual mantle after ~12% MORB-type melt extraction (lherzolite EP22

685   from the Pindos ophiolite in Greece); 2) a comparatively more depleted mantle lherzolite,

686   which represents residual mantle after ~20% MORB-type melt extraction (lherzolite A19

687   from the Othrys ophiolite in Greece). Both these mantle lherzolites were chosen because they

688   did not undergo detectable enrichment in subduction components (Saccani et al., 2017b).

689   However, the model in Figure 12 is not appropriate for estimating the possible contribution of

690   subduction-derived components to the mantle source(s). Therefore, in order to qualitatively

691   evaluate the different chemical contributions from subduction-derived components, the Ba/Th

692   ratios are plotted vs. Th/Nb ratios (Fig. 13) and we have applied REE modelling in order to

693   find the mantle peridotite compositions, the partial melting degree, and the nature and extent

694   of enrichment in LREE due to subduction-related fluids and/or melts that best fit the

695   compositions of the less fractionated basaltic rocks for each magmatic type (Fig. 14).

696   However, in supra-subduction zone settings, the fluid flux from a subducted slab may be

697   either localized or pervasive, and fluid-mobile trace elements may be added at every melting

698   increment (see Barth et al, 2003). In addition, the compositions and the amounts of

699   subduction-related trace elements incorporated into the overlying mantle wedge depend on a

700   number of factors, such as the mineralogical compositions of the subducting rocks,

701   temperatures, pressures, and distance from a subduction zone (see, for example, Pearce and

702   Parkinson, 1993; Gribble et al., 1996; Elliott, 2003, Mibe et al., 2011). Given these

703   uncertainties, a rigorous quantification of the melting processes (i.e., composition of mantle

704   sources and degrees of partial melting) generating the different rock-types is not possible as

705   the mantle source compositions cannot be constrained in detail. Nonetheless, the semi-

706   quantitative modelling of REE shown in Figure 14 can place some solid constraints on the

707   petrogenesis of basaltic rocks in subduction-related settings. Some authors have shown that

708   two distinct components from the slab can be identified in island arc lavas. One component is

709   argued to be a melt of the down-going sediment, while the second is a fluid flux derived from

710   the dehydration of the down-going oceanic crust (e.g., Hochstaedter et al., 2001; Elliott, 2003;

711   Ikeda et al., 2016). The most significant material flux from the slab beneath the fore-arc is

712   water, which is initially represented by seawater released during compaction and porosity

713   reduction in sediments and altered oceanic crust, and then by dehydration of clay minerals

714   (e.g., Kelley et al., 2003; Saffer and Tobin, 2011). For this reason, in the models in Figure 14,

715   the possible contributions from a melt derived from oceanic pelagic sediments (Taylor and

716   McLennan, 1985) and from seawater (Li, 2000) are taken into account. For the sake of

717   consistency, the depleted peridotites used in the models in Figure 14 are the same used in the

718   model in Figure 12.

719

720   *8.1.1. Group 1 pillow lavas*

721

722   In the Cr-Y model (Fig. 12), Group 1 pillow lavas from the Nain-Ashin ophiolites are

723   compatible with partial melting degrees of a depleted lherzolite mantle source residual after

724   12% MORB-type melt extraction (lherzolite EP22), which range from ~8 % (for samples with

725   relatively higher Y content) to ~15 % (for samples with relatively lower Y contents). The

726   Ba/Th enrichment relative to Th/Nb suggests that the mantle sources of these rocks were

727   predominantly influenced by aqueous fluid addition (Fig. 13). The LREE/MREE depleted

728   nature of most samples suggests however that hydration of the sub-arc mantle wedge was

729   accompanied by a moderate transfer of LREE-enriched subduction zone components (e.g.,

730   Barth et al., 2003). Therefore, in Figure 14a a theoretical mantle source has been calculated by

731   adding 0.5% aqueous fluid to the depleted lherzolite EP22. According to the results obtained

732   from the model in Figure 12, the REE composition of Group 1 pillow lavas from the Nain-

733   Ashin ophiolites are compatible with 10 -15 % partial melting of the calculated theoretical

734   mantle source. The low fractionation of HREE with respect to MREE observed in Group 1

735   (Fig. 7b, d) suggests that the melting of sub-arc mantle source occurred in the spinel-facies.

736

737   *8.1.2. Group 1 sheeted dykes*

738

739   Although Group 1 sheeted dykes represent slightly fractionated melts, in the Cr-Y model

740   (Fig. 12) these rocks are compatible with ~20 % partial melting of the depleted lherzolite

741   EP22, or, alternatively, with ~12 % partial melting of the relatively more depleted lherzolite

742   residual after 20% MORB-type melt extraction (lherzolite A19). However, Figure 13 shows

743   that the mantle source of these rocks was influenced by both aqueous fluid and sediment melt

744   additions. Moreover, these rocks are relatively more enriched in Th with respect to Nb and Ta

745   and show a lower LREE/MREE depletion when compared to similar pillow lava basalts (Figs.

746   7e, 9a) further suggesting an involvement of a subduction component relatively rich in Th and

747   LREE. For this reason, the REE composition of the possible mantle source for Group 1

748   sheeted dykes has been calculated by adding 0.1 % aqueous fluid components and 0.2 %

749   sediment melt component to the depleted lherzolite A19. The model in Figure 14b shows that

750   the REE composition of the relatively less fractionated Group 1 sheeted dyke basalts is

751   consistent with 10-12 % partial melting of the assumed theoretical mantle source in the spinel

752   stability field.

753

754   *8.1.3. Group 2 pillow lavas*

755

756   In the Cr-Y model (Fig. 12), the relatively less fractionated Group 2 basalt (sample

757   NA229) is compatible with ~17 % partial melting of the depleted lherzolite EP22, or,

758   alternatively, with ~8 % partial melting of the depleted lherzolite A19. The Th/Nb enrichment

759   relative to Ba/Th (Fig. 13), as well as the high La/Yb ratios displayed by these basalts (Table

760   1, Fig. 7j) suggests that the mantle source of Group 2 rocks was predominantly influenced by

761   a subduction component significantly enriched in Th and LREE. Therefore, we assume that

762   the subduction component that affected the mantle source of Group 2 basalts was likely

763   represented by sediment melt addition (Fig. 13). For the REE models, we therefore calculated

764   two possible theoretical mantle source compositions by adding 0.5 % sediment melt to both

765   lherzolite EP22 (Fig. 14c) and lherzolite A19 (Fig. 14d). According to the Cr-Y model (Fig.

766   12), the REE models show that the REE composition of Group 2 basalt NA229 can be either

767   compatible with 15-18 % partial melting of the depleted lherzolite EP22 (Fig. 14c), or with ~8

768   % partial melting of the relatively more depleted lherzolite A19 (Fig. 14d). With the available

769   data, it not possible to assess in detail which of these models is the most appropriate one for

770   explaining the formation of Group 2 primary melts. In any case, a first order conclusion is

771   that Group 2 primary melts were originated from partial melting of a depleted peridotite

772   residual after 12 – 20% MORB-melt extraction, which underwent subsequent incompatible

773   element input due to sediment melt addition. Finally, the low MREE/HREE fractionation of

774   both sample NA229 ($Sm_N/Yb_N = 1.66$) and calculated melts ($Sm_N/Yb_N = 1.33\text{-}1.43$) suggest

775   that partial melting occurred in the spinel-facies mantle. In fact, the Sm/Yb ratios calculated

776   for partial melting in the garnet-facies mantle starting from the same mantle compositions

777   would be much higher ($Sm_N/Yb_N > 4.0$) than that observed in Group 2 basalts.

778

779   *8.2. Tectono-magmatic significance and geodynamic implications*

780

781   It is widely accepted that the study of igneous rocks incorporated within ophiolitic

782   mélanges may provide robust constraints for the magmatic and geodynamic evolution of the

783   oceanic basins from which they were derived: from continental rifting and break-up to the

784   development of an oceanic lithosphere, its consumption in a converging setting and, finally,

785   ophiolite emplacement (e.g., Floyd et al., 1991; Tankut et al., 1998; Bortolotti et al., 2004). In

786   fact, the petrological evidence presented in Section 8.1 allows us to conclude that pillow lavas

787   and sheeted dykes from the Nain-Ashin ophiolitic mélanges were formed from primary melts

788   generated, in turn, from depleted mantle sources that experienced variable extents of

789   subduction-related metasomatisms prior to melting. Therefore, all these rocks were generated

790   in a volcanic arc tectonic setting. Nonetheless, the different nature of the inferred mantle

791   sources associated with each single rock-group suggests that they were likely formed in

792   different portions of the same volcanic arc setting. The CA nature and the marked influence

793   from sediment melts shown by Group 2 rocks (Figs. 9a and 13) suggest formation in a

794   continental margin volcanic arc or in an intra-oceanic arc characterized by a thick polygenetic

795   crust (see Dilek and Furnes, 2011; Saccani, 2015). In contrast, the island arc tholeiitic affinity

796   of Group 1 rocks and their moderate subduction-type geochemical signature suggest that these

797   rocks were influenced by subduction-released fluids and likely formed in the forearc sector of

798   a volcanic arc setting.

799   Several models for the geodynamic evolution of the oceanic branches of the Neo-Tethys

800   that were existing in Mesozoic times around the CEIM have been suggested by many authors

801   (e.g., Shojaat et al., 2003; Barrier and Vrielynck, 2008; Shafaii Moghadam et al., 2009;

802   Rossetti et al., 2010; Omrani et al., 2013; Mattei et al., 2014; Shirdashtzadeh et al., 2015).

803   Rahmani et al. (2007) suggested that the Nain ophiolites were formed in an intra-oceanic

804   island arc setting during the Late Cretaceous. Likewise, Ghazi and Hassanipak (2000) and

805   Khalatbari Jafari et al. (2015) suggested a similar tectonic setting of formation for the

806   neighbouring Shahr-e-Babak and Dehshir ophiolites, respectively. Unfortunately, these

807   authors did not suggest any hypothesis about the original location of the supposed intra-

808   oceanic arc with respect to the CEIM. Based on geochemical studies on a quite limited

809   number of mafic volcanic rocks from the Nain, Dehshir, Shahr-e-Babak, and Baft ophiolites

810   (Shafaii Moghadam et al., 2009), as well as on the Nain mantle peridotites (Mehdipour Ghazi

811   et al., 2010; Pirnia et al., 2010), these authors have suggested that the Nain-Baft belt

812   ophiolites were formed in a backarc basin. This backarc basin opened in the southern margin

813   of the CEIM in the upper Early Cretaceous and developed in the Late Cretaceous in response

814   to the subduction of the southern branch of the Neo-Tethys below the CEIM (Fig. 15a). The

815   opening of this backarc also resulted in the formation and drifting of the Sanandaj-Sirjan

816   continental block from the CEIM (e.g., Takin, 1972; McCall, 2002; Shahabpour, 2005;

817   Barrier and Vrielynck, 2008).

818   However, recent paleomagnetic studies in Central Iran were used to reconstruct the history

819   of rotations and latitudinal drift of the CEIM during the Mesozoic and Cenozoic times (Mattei

820   et al., 2012, 2014). These studies indicate that the CEIM underwent two distinct phases of

821   significant counter-clockwise rotation: a) during the Early Cretaceous and b) after the Middle-

822   Late Miocene. In particular, the Cenozoic counter-clockwise rotation resulted in a rotation of

823   20°–35° of the CEIM along of the Great Kavir – Dorouneh fault system. The amount of

824   crustal shortening that could be accommodated by this rotation along right-lateral strike-slip

825   faults is estimated to be ~400 km in length and ~100 km apart. According to Mattei et al.

826 (2012), the effects of this rotation are particularly evident in the Anarak-Nain-Ashin area (Fig.

827 1a). In particular, these authors have shown that the Paleozoic continental basement in the

828 Anarak area and the overlying Mesozoic ophiolites of Nain and Ashin were displaced along

829 the Great Kavir – Dorouneh fault system, from a northeasternmost original location as a result

830 of the Cenozoic phase of the counter-clockwise rotation of the CEIM.

831 The overall geochemical characteristics of the Nain-Ashin volcanic rocks and dykes show

832 close similarities with their equivalents from the Sabzevar ophiolites, which were interpreted

833 as formed in a volcanic arc setting (Lensch et al., 1979; Baroz and Macaudiere, 1984; Shojaat

834 et al., 2003; Rezaei et al., 2018) (Fig. 5). In contrast, they show significantly different

835 compositions compared to the volcanic rocks from the Baft, Dehshir, and Shar-e-Babak

836 ophiolites, which have been interpreted as formed in a backarc basin (Shafaii Moghadam et

837 al., 2009) (Fig. 5). A recent petrological study on the mantle lherzolites from the Nain

838 ophiolites has shown that they do not represent relicts of backarc mantle peridotites. Rather,

839 they represent sub-continental mantle (i.e., the Continental Margin ophiolites of Dilek and

840 Furnes, 2011; Saccani et al., 2015) exhumed at an Iberia-type ocean-continent transition zone

841 (Pirnia et al., 2018). Finally, the radiolarian biostratigraphic data presented in this paper

842 indicate that the Ashin volcanic arc rocks were formed during the Aptian.

843 All these data show robust evidence in contrast with the hypothesis of formation of the

844 Nain-Ashin ophiolites in the Nain-Baft backarc basin in the southwest of the CEIM during the

845 Late Cretaceous (Barrier and Vrielynck, 2008; Shafaii Moghadam et al., 2009). For example,

846 the Continental Margin peridotites (Pirnia et al., 2018) are genetically unrelated to the

847 chromitite-bearing harzburgites, as well as to the volcanic rocks and dykes cropping out in the

848 Nain-Ashin ophiolites. In fact, the association of chromite-bearing harzburgites and volcanic

849 arc rocks cropping out in the Nain-Ashin ophiolites point out for their formation in a supra-

850 subduction tectonic setting during the closure phase of the oceanic basin. In contrast,

851   Continental Margin lherzolites, such as the Nain Lherzolites (Pirnia et al., 2018) typically

852   represent subcontinental mantle exhumed during the continental rifting that precede the early

853   stage of formation of a subduction-unrelated oceanic basin (see Dilek and Furnes, 2011;

854   Saccani et al., 2015).

855   A possible tectono-magmatic model that can explain the formation in the Early Cretaceous

856   of the different volcanic arc rock-types in the Nain-Ashin ophiolites is shown in Figures 15b,

857   c. In this model, we suggest that, similar to the Sabzevar ophiolites, the Nain-Ashin volcanic

858   arc rocks were formed in a volcanic arc that was active between the northern margin of the

859   CEIM and the southern margin of Eurasia during the Early Cretaceous (Fig. 15b). Based on

860   evidence shown by Mattei et al. (2012, 2014), we postulate that this volcanic arc was

861   associated with the subduction below the Eurasian margin of the Sabzevar-Nain-Ashin sector

862   of the Sistan Ocean (Fig. 15c), which was driven, in turn, by the Early Cretaceous counter-

863   clock wise rotation and drifting toward the northwest of the CEIM. In the same times, the

864   Sistan Ocean was still opening to the west of the CEIM, as suggested by radiolarian

865   biostratigraphic data (Babazadeh and De Wever, 2004), whereas the southern margin of the

866   CEIM (i.e., the future Sanandaj-Sirjan zone) was characterized by a volcanic arc activity

867   associated with the subduction of the southern branch of the Neo-Tethys below the CEIM

868   (Fig. 15b). To the north of this arc, a continental rifting started in the Early Cretaceous in

869   response to this subduction and evolved to a narrow backarc basin only in the Late Cretaceous

870   (Fig. 15b). The opening of this backarc basin resulted in the formation of the backarc-type

871   oceanic lithosphere now represented by the Dehshir, Shahr-e-Babak, and Baft ophiolites (e.g.,

872   Barrier and Vrielynck, 2008; Shafaii Moghadam et al., 2009).

873   The geochemical models discussed in Section 8.1 show that the Nain-Ashin volcanic rocks

874   and dykes originated from partial melting of depleted peridotites (Fig. 12) that experienced

875   variable extent of chemical contributions from the subducting slab (Figs. 13, 14). The inferred

876   magmatic evolution in the subduction system between the CEIM and the Eurasian plate is

877   shown in Figure 15c. The material released from the subducting slab is represented by water

878   beneath the fore-arc and by melts from the down-going subducting sediments beneath the arc

879   (e.g., Hochstaedter et al., 2001; Elliott, 2003; Ikeda et al., 2016). The contribution from the

880   subducting slab vary from pure aqueous fluid flux for IAT pillow lavas to a mix of aqueous

881   fluids and sediment melts for IAT sheeted dykes, and only sediment melts for CA pillow

882   lavas (Fig. 15c1). We therefore postulate that the different magmatic products found in the

883   Nain-Ashin ophiolites were erupted in different sectors of an arc-forearc setting (Fig. 15c). As

884   commonly observed in convergent plate settings, aqueous fluids are basically released from

885   the slab beneath the fore-arc region, whereas sediment melts are most likely generated

886   beneath the arc (e.g., Hochstaedter et al., 2001; Elliott, 2003; Kelley et al., 2003; Saffer and

887   Tobin, 2011; Ikeda et al., 2016). As a consequence we can postulate that IAT rocks were

888   generated in the forearc and outer arc sectors, whereas, CA rocks were generated in the arc

889   sector. The pressure of crystallization estimated for the different volcanic rock-types also

890   support this conclusion. In fact, the estimated crystallization depths increase from IAT pillow

891   lavas (8 - 19 km) to CA pillow lavas (~23 km). The Mesozoic ophiolites of Nain-Ashin were

892   emplaced before the Paleocene, since they are covered by Paleocene-Eocene sedimentary

893   rocks (Shirdashtzadeh et al., 2011, and references therein).

894

895

896   **9. Conclusions**

897

898   The Nain and Ashin ophiolites consist of "Coloured Mélange" units. They are emplaced onto

899   the westernmost corner of the Central-East Iran microplate (CEIM) at the intersection of two

900   regional-scale transcurrent fault systems, which have been discontinuously active from the

901 Jurassic to present-day. Though volumetrically subordinate these mélanges incorporate

902 distinct tectonic slices consisting of sheeted dykes and pillow lavas. Locally, pillow lavas are

903 stratigraphically associated with radiolarian cherts. The main conclusions obtained from the

904 petrological study of volcanic rocks and dykes, as well as biochronological investigation of

905 the associated cherts can be summarized as follows.

906 1) Volcanic rocks and dykes are largely represented by basalts. Based on whole rock

907 geochemistry and mineral chemistry, these rocks can be divided into two geochemical groups:

908 a) The sheeted dykes and most of the pillow lavas show island arc tholeiitic (IAT) affinity

909 with relatively low contents of Th, Nb, Ta, Ti, coupled with LREE/MREE depletion

910 ($La_N/Sm_N = 0.5 - 1.0$); b) A few pillow lavas from the Nain ophiolites show calc-alkaline

911 (CA) affinity, with comparatively high Th, U, and LREE/MREE ratios ($La_N/Sm_N = 1.9 - 2.6$)

912 coupled with low Nb and Ta contents.

913 2) Cr-Y modeling indicates that both IAT and CA rocks derived from moderate degrees (~8 -

914 ~15%) of partial melting of depleted mantle sources, which experienced previous MORB-

915 melt extraction. REE modeling indicates that mantle sources underwent variable extent of

916 enrichment in subduction-derived components consisting of pure aqueous fluids (for most

917 IAT basalts), pure sediment melts (for CA rocks) and a mix of aqueous fluids and sediment

918 melts (for some IAT sheeted dykes). These conclusions suggest that the studied rocks were

919 formed in an arc-forearc tectonic setting. The radiolarian assemblage in the cherts associated

920 with pillow basalts from the Ashin ophiolites suggest that this volcanic arc setting was active

921 in the Early Cretaceous.

922 3) We propose a new model for the Cretaceous tectonic evolution of the CEIM and

923 surrounding Neo-Tethyan oceanic basins. This model implies that the Nain-Ashin volcanic

924 rocks and dykes were formed, similar to the Sabzevar ophiolites, in a volcanic arc setting

925 located between the northern margin of the CEIM and the southern margin of Eurasia and

926 forming the northwestern prolongation of the Sistan Ocean. This conclusion is also based on

927 recent studies, which have shown that the CEIM underwent a considerable counter-clockwise

928 rotation in the Cenozoic. Therefore, it is reasonable to assume that the Nain-Ashin ophiolites,

929 together with the underlying continental basement, have been displaced in their present day

930 position, along the Great Kavir-Dorouneh fault system, from their northeasternmost original

931 location. Our new model is significantly differing from the currently most accepted

932 hypothesis, which implies that the Nain ophiolites formed, together with the Baft ophiolites,

933 in a backarc basin (the so-called Nain-Baft backarc basin) located to the south of the CEIM

934 during the Late Cretaceous.

935

936

937

938

948

949

950 **Appendix A. Supplementary data.**

951   Supplementary data related to this article can be found at http://_____

952

953

954

955   **References**

956   Allahyari, K., Saccani, E., Rahimzadeh , B., Zeda, O., 2014. Mineral chemistry and petrology
957   of highly magnesian ultramafic cumulates from the Sarve-Abad (Sawlava) ophiolites
958   (Kurdistan, NW Iran): New evidence for boninitic magmatism in intra-oceanic fore-arc
959   setting in the Neo-Tethys between Arabia and Iran. Journal of Asian Earth Sciences 79,
960   312-328.

961   Allègre, C.J., Minster, J.F., 1978. Quantitative models of trace element behaviour in
962   magmatic processes. Earth and Planetary Science Letters 38, 1-25.

963   Angiboust, S., Agard, P., de Hoog, J.C.M., Omrani, J., Plunder, A., 2013. Insights on deep,
964   accretionary subduction processes from the Sistan ophiolitic "mélange" (Eastern Iran).
965   Lithos 156-159, 139-158.

966   Babazadeh, S.A., De Wever, P., 2004. Radiolarian Cretaceous age of Soulabest radiolarites in
967   ophiolite suite of eastern Iran. Bulletin de la Societé géologique de France 175, 121-129.

968   Baroz, F., Macaudiere, J., 1984. La serie volcanosedimentaire du chainon ophiolitique de
969   Sabzevar (Iran). Ofioliti 9, 3–26.

970   Barrier, E., Vrielynck, B., 2008. Palaeotectonic Maps of the Middle East, Tectono-
971   Sedimentary Palinspastic Maps from Late Norian to Piacenzian. Commission for the
972   Geological Map of the World (CGMW), Paris.

973   Barth, M.G., Mason, P.R.D., Davies, G.R., Dijkstra, A.H., Drury, M.R., 2003. Geochemistry
974   of the Othris Ophiolite, Greece: evidence for refertilization? Journal of Petrology 44,
975   1759-1785.

976   Baumgartner, P.O., Bjørklund, K.R., Caulet, J. P., De Wever, P., Kellogg, D., Labracherie,

977   M., Nakaseko, K., Nishimura, A., Schaaf, A., Schimdt-Effing, R., Yao, A., 1981.

978   Eurorad II, 1980. Second European meeting of radiolarian paleontologists: current

979   research on Cenozoic and Mesozoic radiolarians. Eclogae geologicae Helvetiae 74,

980   1027-1061.

981   Beccaluva, L., Macciotta, G., Piccardo, G.B., Zeda, O., 1989. Clinopyroxene compositions of

982   ophiolite basalts as petrogenetic indicator. Chemical Geology 77, 165-182.

983   Beker, J.A., Menzies, M.A., Thirlwall, M.F., Macpherson, C.G., 1997. Petrogenesis of

984   Quaternary intraplate volcanism, Sana'a, Yemen: Implications for plume-Lithosphere

985   interaction and polybaric melt hybridization. Journal of Petrology 38, 1359-1390.

986   Berra, F., Zanchi, A., Angiolini, L., Vachard, D., Vezzoli, G., Zanchetta, S., Bergomi, M.,

987   Javadi, H.R., Kouhpeyma, M., 2017. The upper Palaeozoic Godar-e-Siah Complex of

988   Jandaq: Evidence and significance of a North Palaeotethyan succession in Central Iran.

989   Journal of Asian Earth Sciences 138, 272–290.

990   Bortolotti, V., Chiari, M., Kodra, A., Marcucci, M., Mustafa, F., Principi, G., Saccani, E.,

991   2004. New evidence for Triassic MORB magmatism in the northern Mirdita Zone

992   ophiolites (Albania). Ofioliti 29, 243-246.

993   Camp, V.E., Griffis, R.J., 1982. Character, genesis and tectonic setting of igneous rocks in the

994   Sistan suture zone, eastern Iran. Lithos 15, 221-239.

995   Danelian, T., 2008. Diversity and biotic changes of Arcaeodictyomitrid Radiolaria from the

996   Aptian/Albian transition (OAE1b) of southern Albania. Micropaleontology 54, 3–13.

997   Davoudzadeh, M., 1972. Geology and petrology of the area north of Nain, Central Iran.

998   Geological Survey of Iran, Report No. 1, 89 pp.

999   Delavari, M., Dolati, A., Marroni, M., Pandolfi, L., Saccani, E., 2016. Association of MORB

1000   and SSZ ophiolites along the shear zone between Coloured Mélange and Bajgan

1001   Complexes (North Makran, Iran): evidence from the Sorkhband area. Ofioliti 41, 21–34.

1002   http://dx.doi.org/10.4454/ofioliti.v41i1.440.

1003 Desmons, J., Beccaluva, L., 1983. Mid-Ocean ridge and island-arc affinities in ophiolites

1004   from Iran: Palaeographic implications. Chemical Geology 39, 39-63.

1005 De Wever, P., 1982. Radiolaires du Trias et du Lias de la Téthys (systématique, stratigraphie).

1006   Société Géologique du Nord 7, 1-600.

1007 Dilek, Y., Furnes, H., 2011. Ophiolite genesis and global tectonics: geochemical and tectonic

1008   fingerprinting of ancient oceanic lithosphere. Geological Society of America Bulletin

1009   123, 387-411.

1010 Droop, G.T.R., 1987. A general equation for estimating Fe^{3+} concentrations in

1011   ferromagnesian silicates and oxides from microprobe analyses, using stoichiometric

1012   criteria. Mineralogical Magazine 51, 431-435.

1013 Dumitrica, P., 1970. Cryptocephalic and cryptothoracic Nassellaria in some Mesozoic

1014   deposits of Romania. Revue Roumaine de Géologie, Géophysique et Géographie (série

1015   Géologie) 14, 45-124.

1016 Elliott, T., 2003. Tracers of the slab. In: Eiler, J. (Eds.), Inside the subduction factory.

1017   Geophysical Monograph Series AGU, Washington DC, vol. 138, pp. 23-45.

1018 Ewart, A., Bryan, W.B., Chappell, B.W., Rudnick, R.L., 1994. Regional Geochemistry of the

1019   Lau-Tonga Arc and Backarc Systems. In: Hawkins, J., Parson, L., Allan, J., et al. (Eds.),

1020   Proceedings of the Ocean Drilling Program. Scientific Results 135, College Station, TX

1021   (Ocean Drilling Program), pp. 385-425.

1022 Floyd, P.A., Kelling, G., Gökçen, S.L., Gökçen, N., 1991. Geochemistry and tectonic

1023   environment of basaltic rocks from the Misis Ophiolitic Melange, south Turkey.

1024   Chemical Geology 89: 263-280.

1025 Ghazi, A.M., Hassanipak, A.A., 2000. Petrology and geochemistry of the Shahr-Babak

1026   Ophiolite, central Iran. In: Dilek, Y., Moores, E., Elthon, D., Nicolas, A. (Eds.),

1027   Ophiolites and Oceanic Crust; New Insights from Field Studies and the Ocean Drilling

1028   Program. Geological Society of America, Special Papers 349, pp. 485–497.

1029 Gribble, R.F., Stern, R.J., Bloomer, S.H., Stüben, D., O'Hearn, T., Newman, S., 1996. MORB

1030   mantle and subduction components interact to generate basalts in the southern Mariana

1031   Trough back-arc basin. Geochimica et Cosmochimica Acta 60, 2153-2166.

1032 Hammarstrom, J.M., Zen, E-an., 1986. Aluminium in hornblende: an empirical igneous

1033   geobarometer. American Mineralogist 71, 1297-1313.

1034 Hassanipak, A.A., Ghazi, A.M., 2000. Petrochemistry, $^{40}Ar–^{39}Ar$ ages and Tectonics of the

1035   Naien Ophiolite, Central Iran. GSA Annual Meeting, Reno, Nevada, pp. 237–238.

1036 Hastie, A.R., Kerr, A.C., Pearce, J.A., Mitchell, S.F., 2007. Classification of altered volcanic

1037   island arc rocks using immobile trace elements: development of the Th Co discrimination

1038   diagram. Journal of Petrology 48, 2341-2357.

1039 Hébert, R., Laurent, R., 1990. Mineral chemistry of the plutonic section of the Troodos

1040   ophiolite: new constraints for genesis of arc-related ophiolites. In: Malpas, J., Moores, E.,

1041   Panayiotou, A., Xenophontos, C. (Eds.), Ophiolites-Oceanic Crustal Analogues.

1042   Proceedings of Troodos Ophiolite Symposium, Geological Survey of Cyprus, pp. 149-

1043   163.

1044 Hébert, R., Huot, F., Wang, C., Liu, Z., 2003. Yarlung Zangbo ophiolites (Southern Tibet)

1045   revisited: geodynamic implications from the mineral record. Geological Society London

1046   Special Publications 218, 165-190.

1047 Hochstaedter, A., Gill, J., Peters, R., Broughton, P., Holden, P., Taylor, B., 2001. Across-arc

1048   geochemical trends in the Izu-Bonin arc: Contributions from the subducting slab.

1049   Geochemistry Geophysics Geosystems 2, Paper number 2000GC000105,

1050   https://doi.org/10.1029/2000GC000105.

1051   Hollister, L.S., Grissom, G.C., Peters, E.K., Slowell, H.H., Sisson, V.B., 1987. Confirmation

1052   of the empirical correlation of Al in hornblende with pressure of solidification of calc-

1053   alkaline plutons. American Mineralogist 72, 231-239.

1054   Ikeda, Y., Nagao, K., Ishii, T., Matsumoto, D., Stern, R.J., Kagami, H., Arima, M., Bloomer,

1055   S.H., 2016. Contributions of slab fluid and sediment melt components to magmatism in

1056   the Mariana Arc-Trough system: Evidence from geochemical compositions and Sr, Nd,

1057   and noble gas isotope systematics. Island Arc 25, 253-273.

1058   Johnson, M.C., Rutherford, M.J., 1989. Experimental calibration of the aluminum-in-

1059   hornblende geobarometer with application to Long Valley Caldera (California) volcanic

1060   rocks. Geology 17, 837-841.

1061   Kamenetsky, V.S., Crawford, A.J., Meffre, S., 2001. Factors controlling chemistry of

1062   magmatic spinel: an empirical study of associated olivine, Cr-spinel and melt inclusions

1063   from primitive rocks. Journal of Petrology 42, 655-671.

1064   Kelley, K.A., Plank, T., Ludden, J., Staudigel, H., 2003. Composition of altered oceanic crust

1065   at ODP Sites 801 and 1149. Geochemistry Geophysics Geosystems 4, 1-21.

1066   Kepezhinskas, P.K., Taylor, R.N., Tanaka, H., 1993. Geochemistry of plutonic spinels from

1067   the north Kamchatka arc: comparisons with spinels from other tectonic settings.

1068   Mineralogical Magazine 57, 575-589.

1069   Khalatbari Jafari, M., Sepehr, H., Mobasher, K., 2015. Tectonomagmatic evolution of the

1070   South Dehshir Ophiolite, Central Iran. Geological Magazine 153, 557-577.

1071   doi:10.1017/S0016756815000618.

1072   Lachance, G.R., Traill, R.J., 1966. A practical solution to the matrix problem in X-ray

1073   analysis. Canadian Journal of Spectroscopy 11, 43-48.

1074   Leake, B.E., Woolley, A.R., Arps, C.E.S., Birch, W.D., Gilbert, M.C., Grice, J.D.,

1075   Hawthorne, F.C., Kato, A., Kisch, H.J., Krivovichev, V.G., Linthout, K., Laird, J.,

1076   Mandarino, J.A., Maresch, W.V., Nickel, E.H., Rock, N.M.S., Schumacher, J.C., Smith,

1077   D.C., Stephenson, N.C.N., Ungaretti, L., Whittaker, E.J.W., Youzhi, G., 1997.

1078   Nomenclature of amphiboles: Report of the subcommittee on amphiboles of the

1079   International Mineralogical Association, commission on new minerals and mineral

1080   names. Canadian Mineralogist 35, 219-246.

1081   Lensch, G., Davoudzadeh, M., 1982. Ophiolites in Iran. Neues Jahrbuch für Geologie und

1082   Paläontologie Monatsheft 5, 306–320.

1083   Lensch, G., Mihm, A., Alavi-Tehrani, N., 1979. Major element geochemistry of the ophiolites

1084   north of Sabzevar (Iran). Neues Jahrbuch für Geologie und Paläontologie Monatsheft 7,

1085   415-447.

1086   Leterrier, J., Maury, R.C., Thonon, P., Girard, D., Marchal, M., 1982. Clinopyroxene

1087   composition as a method of identification of the magmatic affinities of paleo-volcanic

1088   series. Earth and Planetary Science Letters 59, 139-154.

1089   Li, G., 2000. Petrologic features and genesis of Cenozoic volcanic rocks, Qiang-tang area,

1090   northern Tibetan Plateau: Geology-Geochemistry 28, 38-44.

1091   Mattei, M., Cifelli, F., Muttoni, G., Zanchi, A., Berra, F., Mossavvari, F., Eshraghi, S.A.,

1092   2012. Neogene block-rotation in Central Iran: evidence from paleomagnetic data.

1093   Geological Society of America Bulletin 124, 943–956.

1094   http://dx.doi.org/10.1130/B30479.1.

1095   Mattei, M., Cifelli, F., Muttoni, G., Rashid, H., 2014. Post-Cimmerian (Jurassic–Cenozoic)

1096   paleogeography and vertical axis tectonic rotations of Central Iran and the Alborz

1097   Mountains. Journal of Asian Earth Sciences 102, 92-101.

1098   http://dx.doi.org/10.1016/j.jseaes.2014.09.038.

1099   Maurel, C., Maurel, P., 1982. Étude expérimental de la distribution de l'aluminium entre bain

1100   silicate basique et spinelle chromifère. Implications pétrogénétiques: teneur en chrome

1101   des spinelles. Bulletin de Minéralogie, 105, 197-202.

1102   McCall, G.J.H., 2002. A summary of the geology of the Iranian Makran. In: Clift, P.D.,

1103   Kroon, D., Gaedicke, C., Craig, J. (Eds.), The Tectonic and Climatic Evolution of the

1104   Arabian Sea Region. Geological Society of London, Special Publication 195, pp. 147–

1105   204.

1106   Mehdipour Ghazi, J., Moazzen, M., Rahgoshay, M., Shafaii Moghadam, H., 2010. Mineral

1107   chemical composition and geodynamic significance of peridotites from Nain ophiolite,

1108   central Iran. Journal of Geodynamic 49, 261-270.

1109   Mibe, K., Kawamoto, T., Matsukage, K.N., Fei, Y., Ono, S., 2011. Slab melting versus slab

1110   dehydration in subduction-zone magmatism. Proceedings of the National Academy of

1111   Sciences 108, 8177-8182.

1112   Morimoto, N., 1989. Nomenclature of pyroxenes. Canadian Mineralogist 27, 143-156.

1113   Murton, B.J., 1989. Tectonic controls on boninite genesis. In: Saunders, A.D., Norry, M.J.

1114   (Eds.), Magmatism in the Ocean Basins. Geological Society of London, Special

1115   Publications 42, pp. 347-377.

1116   O'Dogherty, L., 1994. Biochronology and Paleontology of Mid-Cretaceous Radiolarians from

1117   Northern Apennines (Italy) and Betic Cordillera (Spain). Mémoires de Géologie

1118   (Lausanne) 21, 1-415.

1119   '   rtner, P.O., Matsuoka, A., 2009. Catalogue of Mesozoic radiolarian genera. Part 2:

1120   Jurassic–Cretaceous. Geodiversitas 31, 271–356.

1121   O´Dogherty, L. , Š., Gawlick, H.J., 2017. Middle and Late Jurassic radiolarians from the

1122   Neotethys suture in the Eastern Alps. Journal of Paleontology 91, 25–72.

1123   Omrani, H., Moazzen, M., Oberhänsli, R., Altenberger, U., Lange, M., 2013. The Sabzevar

1124   blueschists of the North-Central Iranian micro-continent as remnants of the Neotethys

1125   related oceanic crust subduction. International Journal of Earth Sciences 102, 1491-

1126   1512.

1127   Parkinson, I.J., Pearce, J.A., 1998. Peridotites from the Izu-Bonin-Mariana forarc (ODP Leg

1128   125): evidence for mantle melting and melt-mantle interaction in a suprasubduction zone

1129   setting. Journal of Petrology 39, 1577-1618.

1130   Pearce, J.A., Norry, M.J., 1979. Petrogenetic implications of Ti, Zr, Y, and Nb variations in

1131   volcanic rocks. Contributions to Mineralogy and Petrology 69, 33-47.

1132   Pearce, J.A., 1982. Trace element characteristics of lavas from destructive plate boundaries.

1133   In: Thorpe, R.S. (Eds.), Andesites. Wiley, New York, pp. 525-548.

1134   Pearce, J.A., 1983. Role of the Sub-continental Lithosphere in Magma Genesis at Active

1135   Continental Margin. In: Hawkesworth, C.J., Norry, M.J. (Eds.), Continental basalts and

1136   mantle xenoliths. Nantwich, Cheshire, Shiva Publications, pp. 230-249.

1137   Pearce, J.A., Parkinson, I.J., 1993. Trace element models for mantle melting: Application to

1138   volcanic arc petrogenesis. Geological Society of London Special Publications 76, 373-

1139   403.

1140   Pearce, J.A., 1996. A user's guide to basalt discrimination diagrams. In: Bailes, A.H.,

1141   Christiansen, E.H., Galley, A.G., Jenner, G.A., Keith, J.D., Kerrich, R., Lentz, D.R.,

1142   Lesher, C.M., Lucas, S.B., Ludden, J.N., Pearce, J.A., Peloquin, S.A., Stern, R.A.,

1143   Stone, W.E., Syme, E.C., Swinden, H.S., Wyman, D.A. (Eds.), Trace element

1144   geochemistry of volcanic rocks: applications for massive sulphide exploration. Short

1145   Course Notes. Geological Association of Canada 12, pp. 79–113.

1146   Pessagno, E.A., Newport, R.L., 1972. A technique for extracting Radiolaria from radiolarian

1147   chert. Micropaleontology 18, 231-234.

1148   Pirnia, T., Arai, S., Torabi, G., 2010. Post-deformational impregnation of depleted MORB in

1149   Nain lherzolite (Central Iran). Journal of Mineralogical and Petrological Sciences 105,

1150   74-79.

1151   Pirnia, T., Arai, S., Torabi, G., 2013. A better picture of the mantle section of the Nain

1152   ophiolite inferred from detrital chromian spinels. Journal of Geology 121, 645-661.

1153   Pirnia, T., Arai, S., Tamura, A., Ishimaru, S., Torabi, G., 2014. Sr enrichment in mantle

1154   pyroxenes as a result of plagioclase alteration in lherzolite. Lithos 196-197, 198-212.

1155   Pirnia, T., Saccani, E., Arai, S., 2018. Spinel and plagioclase peridotites of the Nain ophiolites

1156   (Central Iran): Evidence for the incipient stage of oceanic basin formation. Lithos 310–

1157   311, 1–19. https://doi.org/10.1016/j.lithos.2018.04.001.

1158   Putirka, K.D., 2008. Thermometers and barometers for volcanic systems. In: Putirka, K.D.,

1159   Tepley III, F.J. (Eds.), Minerals, inclusions and volcanic processes. Mineralogical

1160   Society of America, Washington DC, Reviews in Mineralogy and Geochemistry 69, pp.

1161   61–120.

1162   Putirka, K.D., Mikaelian, H., Ryerson, F., Shaw, H., 2003. New clinopyroxene-liquid

1163   thermobarometers for mafic, evolved, and volatile-bearing lava compositions, with

1164   applications to lavas from Tibet and the Snake River Plain, Idaho. American Mineralogist

1165   88, 1542-1554.

1166   Rahmani, F., Noghreyan, M., Khalili, M., 2007. Geochemistry of sheeted dikes in the Nain

1167   ophiolite (Central Iran). Ofioliti 32, 119-129.

1168   Rezaei, Z., Noghreyan, M., Saccani, E., 2018. Petrology and geochemistry of sheeted dykes

1169   and pillow lavas from the Sabzevar ophiolite ophiolitic mélange (northeast Iran): New

1170   constraints for the Late Cretaceous evolution of the Neo-Tethys oceanic basin between

1171   the central Iranian microcontinent and Eurasia. Ofioliti, in press, doi:

1172   0.4454/ofioliti.v43i2.510.

1173 Robertson, A.H.F., 2007. Overview of tectonic settings related to the rifting and opening of

1174   Mesozoic ocean basins in the Eastern Tethys: Oman, Himalayas and Eastern

1175   Mediterranean regions. In: Karner, G.D., Manatschal, G., Pinheiro, L.M. (Eds.), Imaging,

1176   Mapping and Modelling Continental Lithosphere Extension and Breakup. Geological

1177   Society of London, Special Publication 282, pp. 325–388.

1178 Rolland, Y., Galoyan, G., Bosch, D., Sosson, M., Corsini, M., Fornari M., Verati, C., 2009.

1179   Jurassic Back-arc and hot-spot related series in the Armenian ophiolites-Implications for

1180   the obduction process. Lithos 112, 163-187.

1181 Rollinson, H., 2008. The geochemistry of mantle chromitites from the northern part of the

1182   Oman ophiolite: inferred parental melt compositions. Contributions to Mineralogy and

1183   Petrology 156, 273-288.

1184 Rossetti, F., Nasrabady, M., Vignaroli, G., Theye, T., Gerdes, A., Razavi, M., Moin Vaziri,

1185   H., 2010. Early Cretaceous migmatitic mafic granulites from the Sabzevar range (NE

1186   Iran): implications for the closure of the Mesozoic peri-Tethyan oceans in central Iran.

1187   Terra Nova 22, 26-34.

1188 Saccani, E., Photiades, A., Beccaluva, L., 2008a. Petrogenesis and tectonic significance of

1189   IAT magma-types in the Hellenide ophiolites as deduced from the Rhodiani ophiolites

1190   (Pelagonian zone, Greece). Lithos 104, 71-84.

1191 Saccani, E., Bortolotti, V., Marroni, M., Pandolfi, L., Photiades, A., Principi, G., 2008b. The

1192   Jurassic association of backarc basin ophiolites and calc-alkaline volcanics in the

1193   Guevgueli Complex (northern Greece): Implication for the evolution of the Vardar Zone.

1194   Ofioliti 33, 209-227.

1195 Saccani, E., Delavari, M., Beccaluva, L., Amini, S., 2010. Petrological and geochemical

1196   constraints on the origin of the Nehbandan ophiolitic complex (eastern Iran): Implication

1197   for the evolution of the Sistan Ocean. Lithos 117, 209-228.

1198   Saccani, E., Allahyari, K., Rahimzadeh, B., 2014. Petrology and geochemistry of mafic

1199   magmatic rocks from the Sarve-Abad ophiolites (Kurdistan region, Iran): Evidence for

1200   interaction between MORB-type asthenosphere and OIB-type components in the

1201   southern Neo-Tethys Ocean. Tectonophysics 621, 132-147.

1202   Saccani, E., Dilek, Y., Marroni, M., Pandolfi, L., 2015. Continental margin ophiolites of

1203   Neotethys: Remnants of ancient ocean-continent transition zone (OCTZ) lithosphere and

1204   their geochemistry, mantle sources and melt evolution patterns. Episodes 38, 230-249.

1205   doi: 10.18814/epiiugs/2015/v38i4/82418.

1206   Saccani, E., Tassinari, R., 2015. The role of MORB and SSZ magma-types in the formation

1207   of Jurassic ultramafic cumulates in the Mirdita ophiolites (Albania) as deduced from

1208   chromian spinel and olivine chemistry. Ofioliti 40, 37-56.

1209   Saccani, E., Delavari, M., Dolati, A., Marroni, M., Pandolfi, L., Chiari, M., Barbero, E.,

1210   2017a. New insights into the geodynamics of Neo-Tethys in the Makran area: Evidence

1211   from age and petrology of ophiolites from the Coloured Mélange Complex (SE Iran).

1212   Gondwana Research 62, 306–327. http://dx.doi.org/10.1016/j.gr.2017.07.013.

1213   Saccani, E., Dilek, Y., Photiades, A., 2017b. Time-progressive mantle-melt evolution and

1214   magma production in a Tethyan marginal sea: A case study of the Albanide-Hellenide

1215   ophiolites. Lithosphere 10, 35-53. https://doi.org/10.1130/L602.1.

1216   Saffer, D.M., Tobin, H.J., 2011. Hydrogeology and mechanics of subduction zone forearcs:

1217   fluid flow and pore pressure. Annual Review of Earth and Planetary Sciences 39, 157–

1218   186.

1219   Sengör, A.M.C., 1990. A new model for the Late Paleozoic-Mesozoic tectonic evolution of

1220   Iran and implications for Oman. In: Robertson, A.H.F., Searle, M.P., Ries, A.C. (Eds.),

1221   The Geology and Tectonics of the Oman Region. Geological Society London, Special

1222   Publications 49, pp. 797-831.

1223 Shahabpour, J., 2005. Tectonic evolution of the orogenic belt in the region located between

1224   Kerman and Neyriz. Journal of Asian Earth Sciences 24, 405–417.

1225 Shafaii Moghadam, H., Rahgoshay, M., Whitechurch, H., 2008. Mesozoic back-arc extension

1226   in the active margin of the Iranian continental block: constraints from age and

1227   geochemistry of the mafic lavas. Ofioliti 33, 95-103.

1228 Shafaii Moghadam, H., Whitechurch, H., Rahgoshay, M., Monsef, L., 2009. Significance of

1229   Nain-Baft ophiolite belt (Iran): short-lived, transtensional Cretaceous back-arc oceanic

1230   basins over the Tethyan subduction zone. Comptes Rendus Geoscience 341, 1016-1028.

1231 Sharkovski, M., Susov, M., Krivyakin, B., Morozov, L., Kiristaev, V., Romanko, E., 1984.

1232   Geology of the Anarak area (Central Iran). Explanatory Text of the Anarak Quadrangle

1233   Map 1:250000: Tehran, Geological Survey of Iran and Moscow, V/O "Technoexport",

1234   Report No. 19, pp. 143.

1235 Shirdashtzadeh, N., Torabi, G., Arai, S., 2010. Metamorphism and metasomatism in the

1236   Jurassic Nain ophiolite melange, Central Iran. Neues Jahrbuch für Geologie und

1237   Paläontologie Abhandlungen 255, 255-275.

1238 Shirdashtzadeh, N., Torabi, G., Arai, S., 2011. Two Mesozoic oceanic phases recorded in the

1239   basic and metabasic rocks of the Nain and Ashin-Zavar ophiolitic melanges (Isfahan

1240   Province, Central Iran). Ofioliti 36, 191-205.

1241 Shirdashtzadeh, N., Kachovich, S., Aitchison, J.C., Samadi, R., 2015. Mid-Cretaceous

1242   radiolarian faunas from the Ashin Ophiolite (western Central-East Iranian

1243   Microcontinent). Cretaceous Research 56, 110-118.

1244 Shojaat, B., Hassanipak, A.A., Mobasher, K., Ghazi, A.M., 2003. Petrology, geochemistry

1245   and tectonics of the Sabzevar ophiolite, North Central Iran. Journal of Asian Earth

1246   Sciences 21, 1053-1067.

1247   Stevens, R.E., 1944. Composition of some chromites of the western Hemisphere. American

1248   Mineralogist 29, 1-34.

1249   Stöcklin, J., 1974. Northern Iran: Alborz Mountain. In: Spencer, A.M. (Ed.), Mesozoic-

1250   Cenozoic orogenic belts, data for orogenic studies. Geological Society of London

1251   Special Publications 4, 213-234.

1252   Stoneley, R., 1975. On the origin of ophiolite complexes in the southern Tethys region.

1253   Tectonophysics, 25, 303-322.

1254   Sun, S.S., McDonough, W.F., 1989. Chemical and isotopic-systematics of oceanic basalts:

1255   implications for mantle composition and processes. In: Saunders, A.D., Norry, M.J.

1256   (Eds.), Magmatism in Ocean Basins. Geological Society of London, Special

1257   Publications 42, pp. 313-345.

1258   Takin, M., 1972. Iranian geology and continental drift in the Middle East. Nature 235, 147-

1259   150.

1260   Tankut, A., Dilek, Y., Önen, P., 1998. Petrology and geochemistry of the Neo-Tethyan

1261   volcanism as revealed in the Ankara melange, Turkey. Journal of Volcanology and

1262   Geothermal Research 85, 265–284.

1263   Taylor, S.R., McLennan, S.M., 1985. The Continental Crust: its composition and evolution:

1264   an examination of the geochemical record preserved in sedimentary rocks. Oxford,

1265   Blackwell Scientific Publication, 312 pp.

1266   Torabi, G., 2004. Petrology of Anarak area ophiolites (NE of Isfahan Province, Iran). PhD

1267   thesis, Tarbiat Modarres University, pp. 240.

1268   Torabi, G., Abdullahi, E., Shirdashtzadeh, N., 2008. Application of mineral and whole rock

1269   analysis in identification of petrogenesis of pillow lavas in the Nain ophiolite (in Persian

1270   with Abstract in English). Iranian Journal of Crystallography and Mineralogy 16, 295-

1271   312.

1272   Torabi, G., Arai, S., Koepke, J., 2011a. Metamorphosed mantle peridotites from Central Iran

1273   (Jandaq area, Isfahan province). N. J. Geol. Paläont. Abh. 261, 129-150.

1274   Torabi, G., Shirdashtzadeh, N., Arai, S., Koepke, J., 2011b. Paleozoic and Mesozoic

1275   ophiolites of Central Iran: amphibolites from Jandaq, Posht-e-Badam, Nain and Ashin

1276   ophiolites. Neues Jahrbuch für Geologie und Paläontologie Abhandlungen 262, 227-

1277   240.

1278   Valsami, E., Cann, J.R., 1992. Mobility of rare earth elements in zones of intense

1279   hydrothermal alteration in the Pindos ophiolite, Greece. In: Parson, L.M., Murton, B.J.,

1280   Browning, P. (Eds.), Ophiolites and their modern oceanic analogues. Geological Society

1281   of London, Special Publications 60, pp. 219-232.

1282   Winchester, J.A., Floyd, P.A., 1977. Geochemical discrimination of different magma series

1283   and their differentiation products using immobile elements. Chemical Geology 20, 325-

1284   343.

1285   Whitney, D.L., Bernard, W.E., 2010. Abbreviations for names of rock-forming minerals.

1286   American Mineralogist 95, 185-187. doi: 10.2138/am.2010.3371.

1287   Workman, R.K., Hart, S.R., 2005. Major and Trace Element Composition of the Depleted

1288   MORB Mantle (DMM). Earth and Planetary Science Letters 231, 53-72, 2005.

1289   Yuan, C., Sun, M., Zhou, M.F., Xiao, W., Zhou, H., 2005. Geochemistry and petrogenesis of

1290   the Yishak Volcanic Sequence, Kudi ophiolite, West Kunlun (NW China): implications

1291   for the magmatic evolution in a subduction zone environment. Contributions to

1292   Mineralogy and Petrology 150, 195-211.

1293   Zanchetta, S., Malaspina, N., Zanchi, A., Benciolini, L., Martin, S., Javadi, H.R.,

1294   Kouhpeyma, M., 2017. Contrasting subduction-exhumation paths in the blueschists of the

1295   Anarak Metamorphic Complex (Central Iran). Geological Magazine 155, 316-334.

1296   Zanchi, A., Malaspina, N., Zanchetta, S., Berra, F., Benciolini, L., Bergomi, M., Cavallo, A.,

1297   Javadi, H.R., Kouhpeyma, M., 2015. The Cimmerian accretionary wedge of Anarak,

1298   Central Iran. Journal of Asian Earth Sciences 102, 45-72.

1299 Zhou, M.F., Robinson, P.T., Malpas, J., Li, Z., 1996. Podiform chromitites in the Luobusa

1300   ophiolite (southern Tibet): implications for melt-rock interaction and chromite

1301   segregation in the upper mantle. Journal of Petrology 37, 3-21.

1302

1303 **Table captions**

1304

1305 **Table 1.** Major and trace element analyses of pillow lavas and sheeted dykes of the Nain and

1306 Ashin ophiolites. Abbreviations, bas and: basaltic andesite; b.d.l.: below detection limit. Mg#

1307 $= 100 \times Mg/(Mg + Fe^{2+})$. Fe_2O_3 is calculated assuming $Fe_2O_3 = 0.15 \times FeO$. Normalizing

1308 values for REE ratios are from Sun and McDonough (1989).

1309

1310 **Table 2.** Representative analyses of clinopyroxenes in Group 1 (island arc tholeiite) and

1311 Group 2 (calc-alkaline) pillow lavas from the Nain and Ashin ophiolites and estimated

1312 temperature (T°C) and pressure (GPa) of crystallization. Abbreviations, Wo: wollastonite; En:

1313 enstatite; Fs: ferrosilite; Acm: acmite. Mg# $= 100 \times Mg/(Mg + Fe^{2+})$. Fe^{3+} and Fe^{2+}

1314 compositions were calculated from total measured FeO according to Droop (1987).

1315 Temperatures were estimated according to Putirka et al. (2003), whereas pressures were

1316 estimated according to Putirka (2008).

1317

1318 **Table 3.** Representative analyses of chromian spinels (spl) in Group 1 (island arc tholeiite)

1319 pillow lavas from the Nain and Ashin ophiolites. Abbreviations, Al-Chr: Al-chromite

1320 (abbreviation for mineral name is from Whitney and Evans, 2010). Mg# $= 100 \times Mg/(Mg +$

1321 Fe^{2+}); Cr# $= 100 \times Cr/(Cr + Al)$. The Fe^{3+} and Fe^{2+} compositions were calculated from total

1322 measured FeO according to Droop (1987).

1323

1324 **Table 4.** Representative analyses of amphiboles in Group 1 (island arc tholeiite) sheeted

1325 dykes from the Nain ophiolites and pillow lavas from the Ashin ophiolites. Pressures (P GPa)

1326 of crystallization estimated according to different methods are also shown. Abbreviations,

1327 Mhb: magnesio-hornblende (abbreviation for mineral name is from Whitney and Evans,

1328   2010). Mineral classification is from Leake et al. (1997). Atoms per formula units are

1329   calculated based on 23 oxygens with Fe^{2+}/Fe^{3+} estimation assuming 13 cations excluding Ca,

1330   Na, and K. Mg# $= 100 \times Mg/(Mg + Fe^{2+})$.

1331

1332

1333 **Figure captions**

1334

1335 **Figure 1.** (a) Geological map of Iran. Ophiolites and major tectonic units are shown. (b)

1336 Simplified geological map of the Nain ophiolitic mélange (modified after Davoudzadeh,

1337 1972), (c) Simplified geological map of the Ashin ophiolitic mélange (modified from the

1338 Anarak geological map 1:250000, Sharkovski et al., 1984). Sample locations are shown.

1339

1340 **Figure 2.** Field photographs of the upper crust ophiolitic rocks in the Nain and Ashin

1341 ophiolites. (a) Sheeted dyke outcrop in the Nain ophiolite. The dashed lines show the general

1342 trend of dykes; (b), (c) Pillow lavas in the Nain and Ashin ophiolites, respectively; (d) Close

1343 view of the basaltic pillow lavas in the Nain area; (e) Stratigraphic contact between pillow

1344 lavas and radioralian cherts in the Ashin ophiolites; (f) Close view of the contact shown in

1345 Fig. 2e.

1346

1347 **Figure 3.** Albian radiolarians from sample 1010, magnification of all specimens 120x (scale

1348 bar 100 μm).

1349 1. *Acanthocircus* cf. *levis* (Donofrio and Mostler); 2. *Crucella* cf. *euganea* (Squinabol); 3.

1350 *Cryptamphorella conara* (Foreman); 4, 5. *Crococapsa asseni* (Tan); 6. *Napora* cf.

1351 *praespinifera* (Pessagno); 7, 8. *Parvimitrella communis* (Squinabol); 9, 10. *Thanarla*

1352 *brouweri* (Tan); 11, 12. *Thanarla praeveneta* Pessagno; 13, 14. *Thanarla* aff. *praeventa*

1353 Pessagno. This morphotype has stronger constrictions than typical *Thanarla praeveneta*. In

1354 the studied sample, *Thanarla brouweri* and *Thanarla* aff. *praeventa* are two end members

1355 linked by a continuum of transitional forms (*Thanarla praeveneta*) with indistinct

1356 morphological delimitations; 15. *Pseudodictyomitra* cf. *paronai* (Aliev); 16. *Xitus* cf.

1357   *spicularius* (Aliev); 17–23. *Dictyomitra montisserei* (Squinabol) *sensu* O'Dogherty (1994);

1358   24–30. *Mita gracilis* (Squinabol).

1359

1360   **Figure 4.** Photomicrographs of the pillow lavas and dykes from the Nain and Ashin

1361   ophiolites. (a) Olivine (Ol) phenocryst in a groundmass with intersertal texture composed of

1362   plagioclase (Pl) laths and intergranular clinopyroxene (Cpx), and minor glass (Nain pillow

1363   lava, sample NA407); (b) Phenocrysts of Cpx and Pl in a groundmass showing subophitic

1364   texture (Nain pillow lava, sample 229); (c) Coarse-grained doleritic texture with Pl and

1365   hornblende amphibole (Amp) in the Nain sheeted dykes (sample NA538); (d) Euhedral

1366   chromian-spinel (Spl) showing inclusions of altered silicate minerals (Incl) in the Ashin

1367   pillow lavas. (a), (b), (c): cross polarized light; (d): is plane polarized light.

1368

1369   **Figure 5.** Nb/Y vs. Zr/Ti discrimination diagram of Winchester and Floyd (1977) modified

1370   by Pearce (1996) for basaltic pillow lavas and sheeted dykes of the Nain and Ashin ophiolites.

1371

1372   **Figure 6.** Variation in selected major and trace elements vs. Mg# [MgO/MgO + FeO] for

1373   basaltic pillow lavas and sheeted dykes of the Nain and Ashin ophiolites. Major element

1374   oxides are recalculated on anhydrous bases. Arrows indicate general fractionation trends for

1375   the different rock-groups. Abbreviations, Th: Tholeiitic (Group 1); CA: calc-alkaline (Group

1376   2).

1377

1378   **Figure 7.** N-MORB normalized incompatible element patterns (a, c, e, g, i) and chondrite-

1379   normalized REE patterns (b, d, f, h, j) for basaltic pillow lavas and sheeted dykes of the Nain

1380   and Ashin ophiolites. The compositions of basaltic pillow lavas and dykes from the Baft and

1381   Dehshir (Shafaii Moghadam et al., 2009), and Sabzevar (Rezaei et al., 2018) ophiolites are

1382 also shown. The compositions of island arc tholeiites (IAT), calc-alkaline basalts and basaltic

1383 andesites (CAB-BA), and backarc basin basalts (BABB) from various ophiolitic complexes

1384 and modern oceanic settings, as well as modern normal-type mid-ocean ridge basalt (N-

1385 MORB) are shown for comparison in Panels g) and h). Data source, IAT: Saccani et al.

1386 (2008a); Yuan et al. (2005); Ewart et al. (1994); CAB-BA: Saccani et al. (2008b); Ewart et al.

1387 (1994); BABB: Saccani et al. (2008b); Rolland et al. (2009); Yuan et al. (2005); Ewart et al.

1388 (1994). Normalizing values and the compositions of N-MORB are from Sun and McDonough

1389 (1989).

1390

1391 **Figure 8.** Th vs. Co discrimination diagram (Hastie et al., 2007) for basaltic pillow lavas and

1392 sheeted dykes of the Nain and Ashin ophiolites.

1393

1394 **Figure 9.** N-MORB-normalized Th vs. Nb discrimination diagram of Saccani (2015) for

1395 basaltic pillow lavas and sheeted dykes of the Nain and Ashin ophiolites. a) rock types, b)

1396 tectonic setting interpretation. Abbreviations, MORB: mid-ocean ridge basalt, N-: normal

1397 type, E-: enriched type, D-: depleted type, MTB: medium Ti basalt; IAT: island arc tholeiite,

1398 CAB: calc-alkaline basalt; OIB: alkaline oceanic within-plate basalt; SSZ-E: supra-

1399 subduction zone enrichment, AFC: assimilation-fractional crystallization, OIB-CE: OIB

1400 component enrichment, FC: fractional crystallization. Normalization values, as well as the

1401 composition of typical N-MORB, EMORB, and OIB (stars) are from Sun and McDonough

1402 (1989).

1403

1404 **Figure 10.** (a) Ti vs. (Ca+Na), (b) (Ti+Cr) vs. Ca, and (c) Ti vs. Al_{tot} discrimination diagrams

1405 of Leterrier et al. (1982) showing the composition of clinopyroxenes from the Group 1 (island

1406 arc tholeiite) and Group 2 (calc-alkaline) pillow lavas from the Nain and Ashin ophiolites.

1407

1408 **Figure 11.** Mg# vs. Cr# diagram for spinels (spl) from the Group 1 (island arc tholeiite)

1409 pillow lavas from the Nain and Ashin ophiolites. Mg# = Mg/(Mg + Fe^{2+}), Cr# = Cr/(Cr + Al).

1410 The compositional variations of chromian spinels from alkaline basalts, boninites, island arc

1411 tholeiites (IAT), and normal-type mid-ocean ridge basalt (N-MORB) are also shown. Data

1412 from Hébert et al. (2003) and references therein.

1413

1414 **Figure 12.** Cr vs. Y diagram of Pearce (1982) and melting models for basaltic pillow lavas

1415 and sheeted dykes of the Nain and Ashin ophiolites. Abbreviations, DMM: depleted MORB

1416 mantle (Workman and Hart, 2005). Melting paths (with partial melting degrees) for

1417 incremental batch melting are calculated according to Murton (1989). The composition of

1418 depleted mantle lherzolites assumed as possible mantle sources (A19 and EP22) are from

1419 Saccani et al. (2017b). Sources EP22 and A19 represent residual mantle sources after 12%

1420 and 20% MORB melt extraction from the DMM source, respectively. The fractional

1421 crystallization trends are also shown (tick marks indicate 10% fractional crystallization steps).

1422

1423 **Figure 13.** Ba/Th vs. Th/Nb diagram for basaltic pillow lavas and sheeted dykes of the Nain

1424 and Ashin ophiolites. Stars indicate the compositions of average pelitic sediments (APS,

1425 Taylor and McLennan, 1985) and normal-type mid-ocean ridge basalt (N-MORB, Sun and

1426 McDonough (1989).

1427

1428 **Figure 14.** Calculated chondrite-normalized (Sun and McDonough, 1989) rare earth element

1429 patterns for parental melts derived from different mantle sources, assuming various degrees of

1430 non-modal fractional melting according to the parameters (source modes, melting proportions,

1431 etc.) listed in Appendix A2, which also show the compositions of the different inferred mantle

1432 sources.

1433

1434 **Figure 15.** a), b) Early and Late Cretaceous paleotectonic schemes of the Central-East Iran

1435 microcontinent (CEIM) and surrounding areas. a) Based on the extant literature data (redrawn

1436 from Barrier and Vrielynck, 2008); b) Based on the new data presented in this paper

1437 (modified from Barrier and Vrielynck, 2008; Allahyari et al., 2014; Mattei et al., 2014;

1438 Saccani et al., 2014); c) Two-dimensional tectonic reconstruction of the subduction in the

1439 transect from the northern CEIM to the southern Eurasian continental margin at Early

1440 Cretaceous times. Abbreviations, MOR: mid-ocean ridge; HP-LT: high pressure-low

1441 temperature; IAT: island arc tholeiite; CA: calc-alkaline.

1442

1443

1444

1445

1446 **Supplementary material captions**

1447

1448 **Appendix A1**. Accuracy and detection limits for X-Ray Fluorescence (XRF) and Inductively

1449 Coupled Plasma-Mass Spectrometry (ICP-MS) analyses.

1450

1451 **Appendix A2**. Input parameters and inferred mantle source compositions for the partial

1452 melting models used for different rock-types.

1453

Fig. 1
Click here to download high resolution image

Fig. 1

a) Sheeted dikes

b) Pillow lava

c) Pillow lava

d) Pillow lava
1m

e) Pillow lava   Chert

f) Chert
Pillow lava
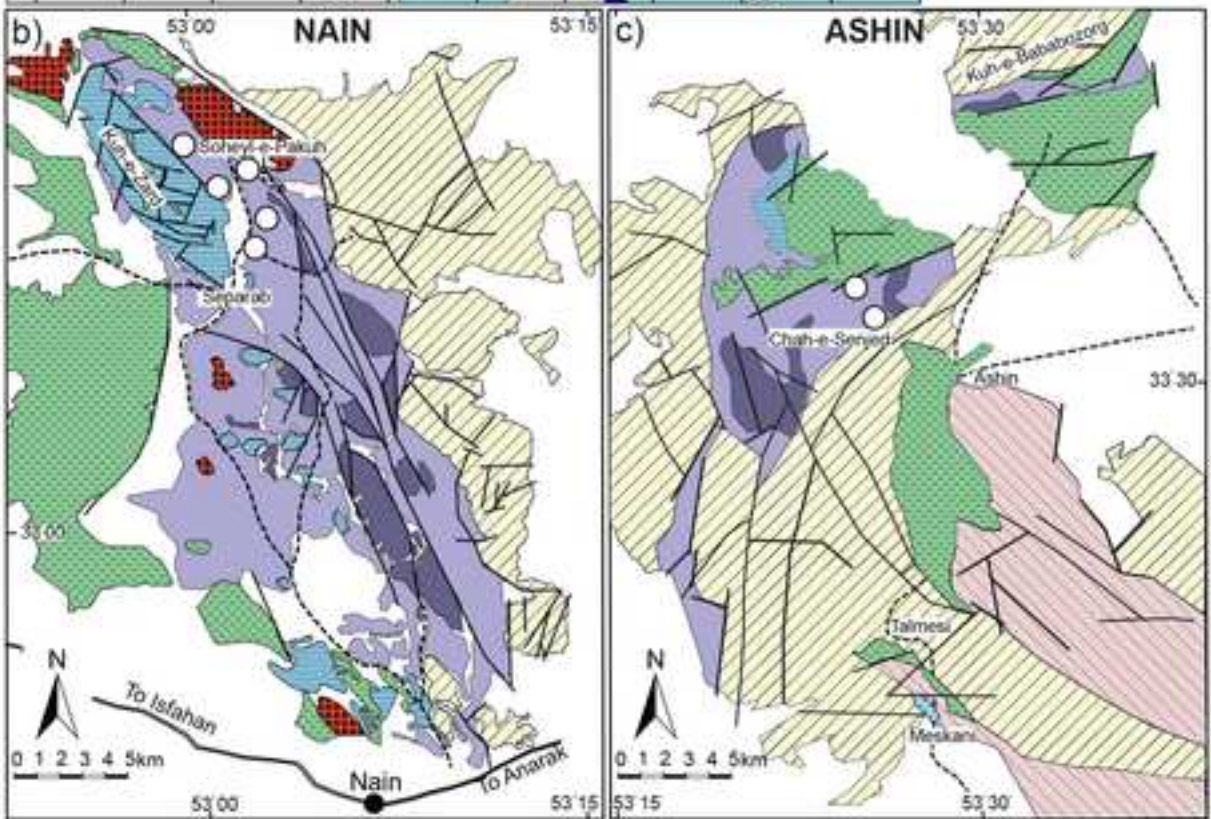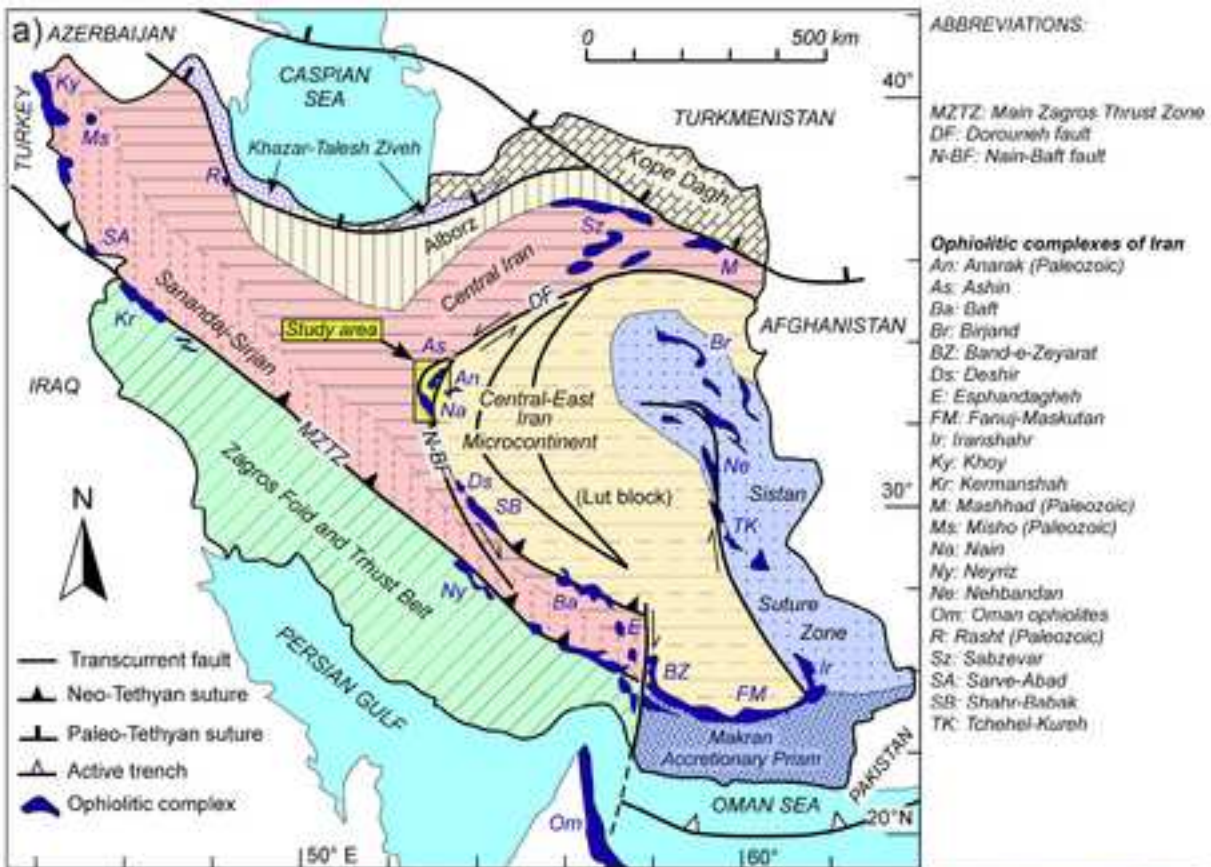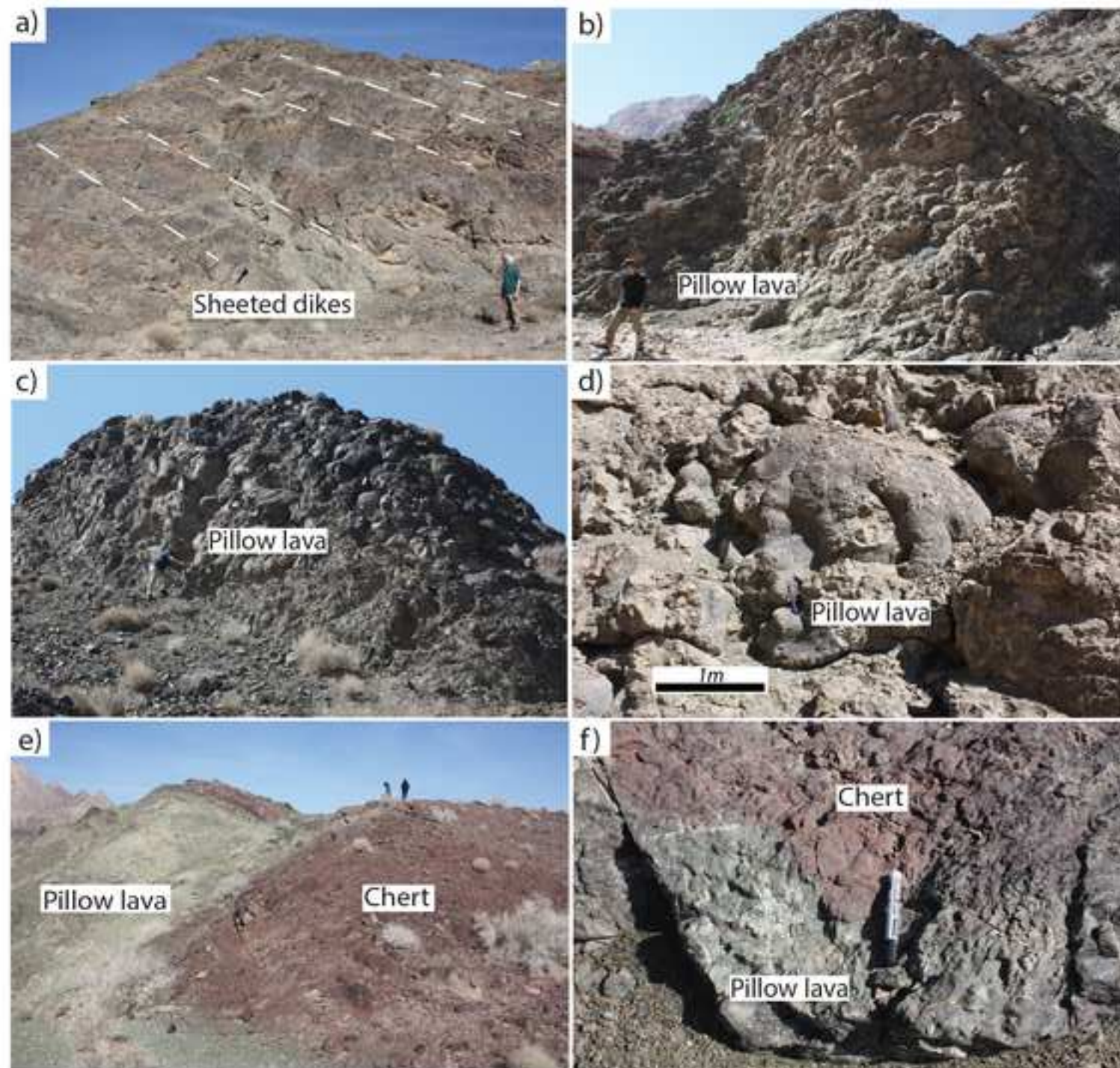
Fig. 3
Click here to download high resolution image
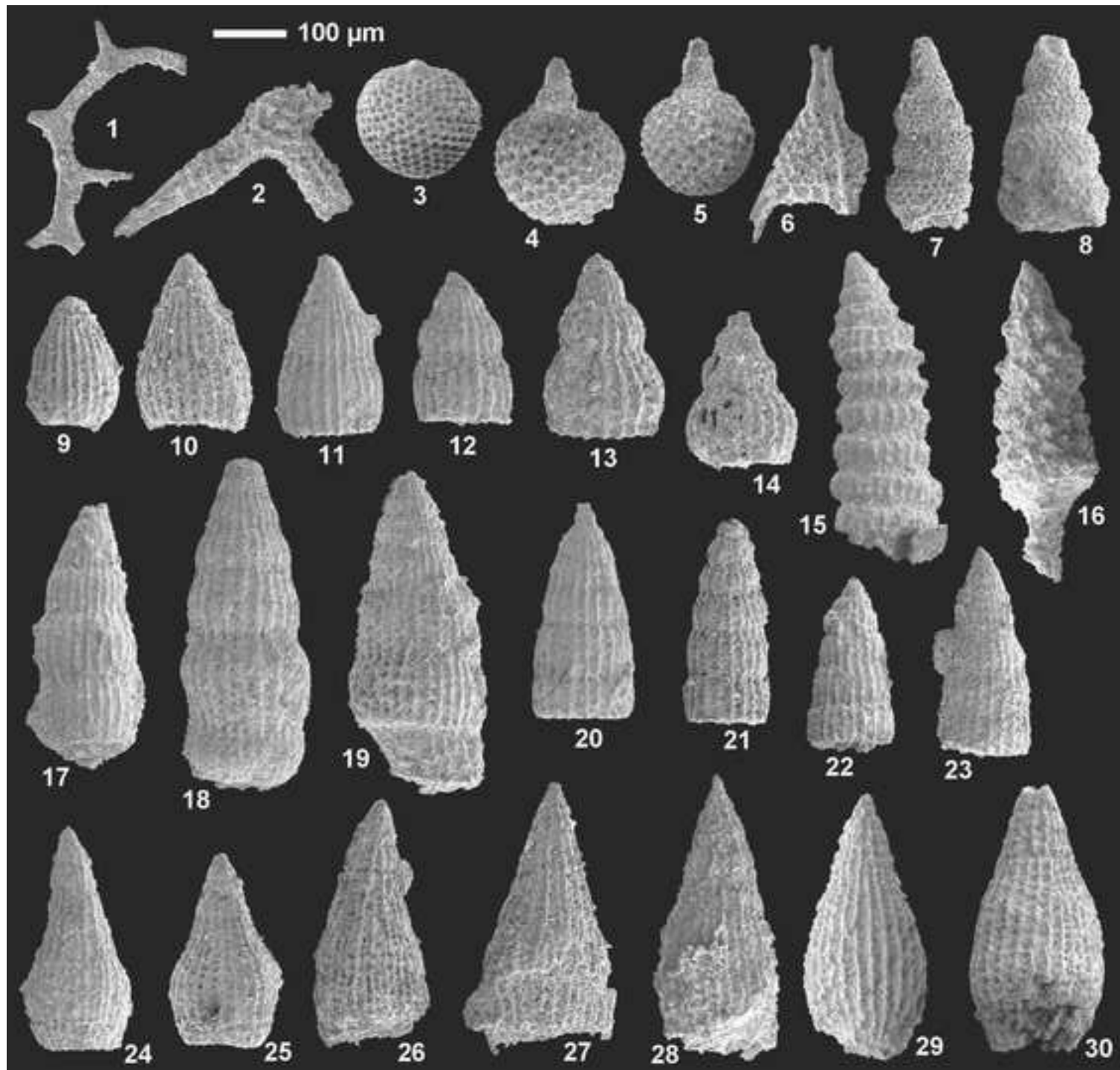
Fig. 4
Click here to download high resolution image
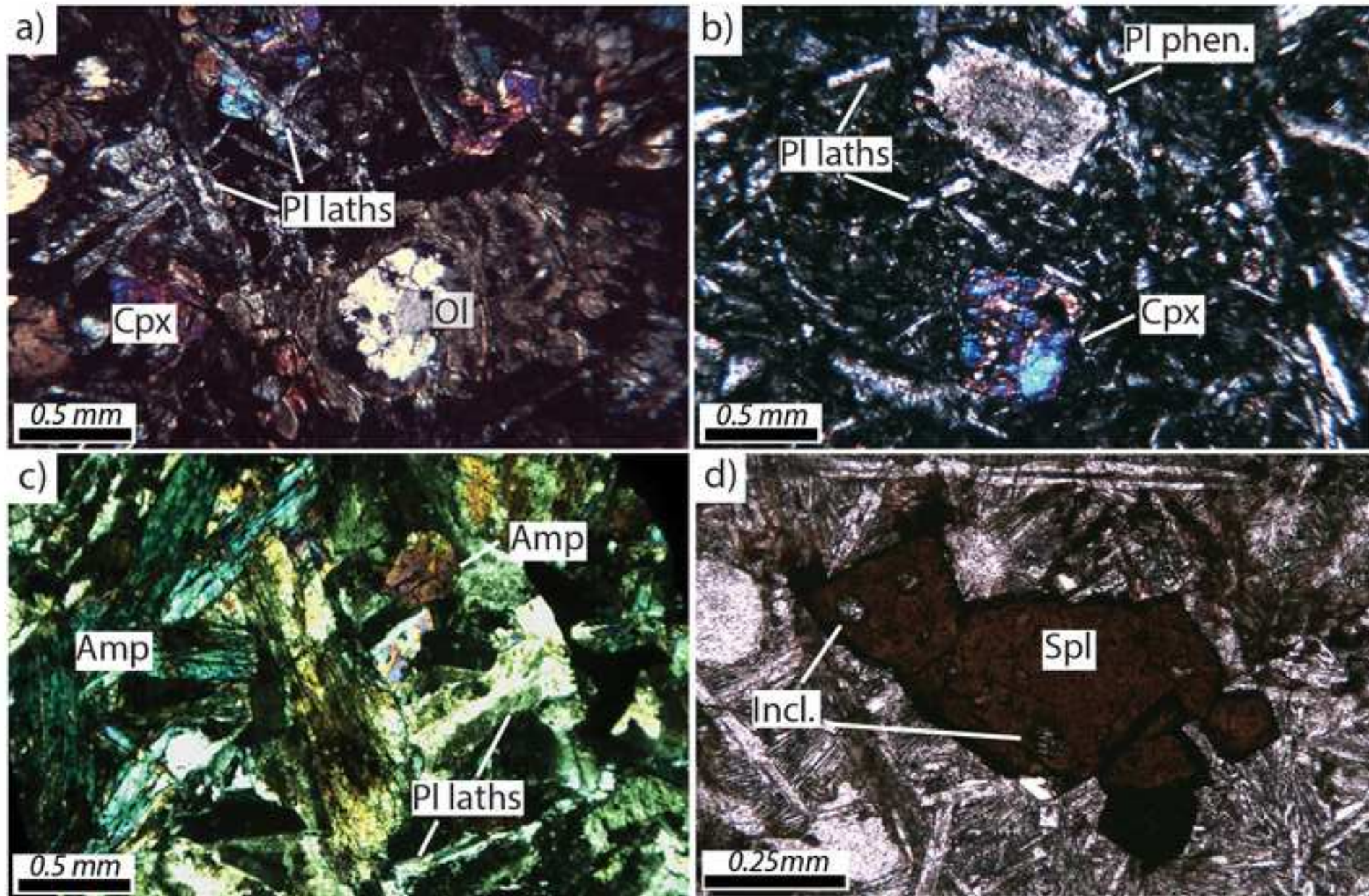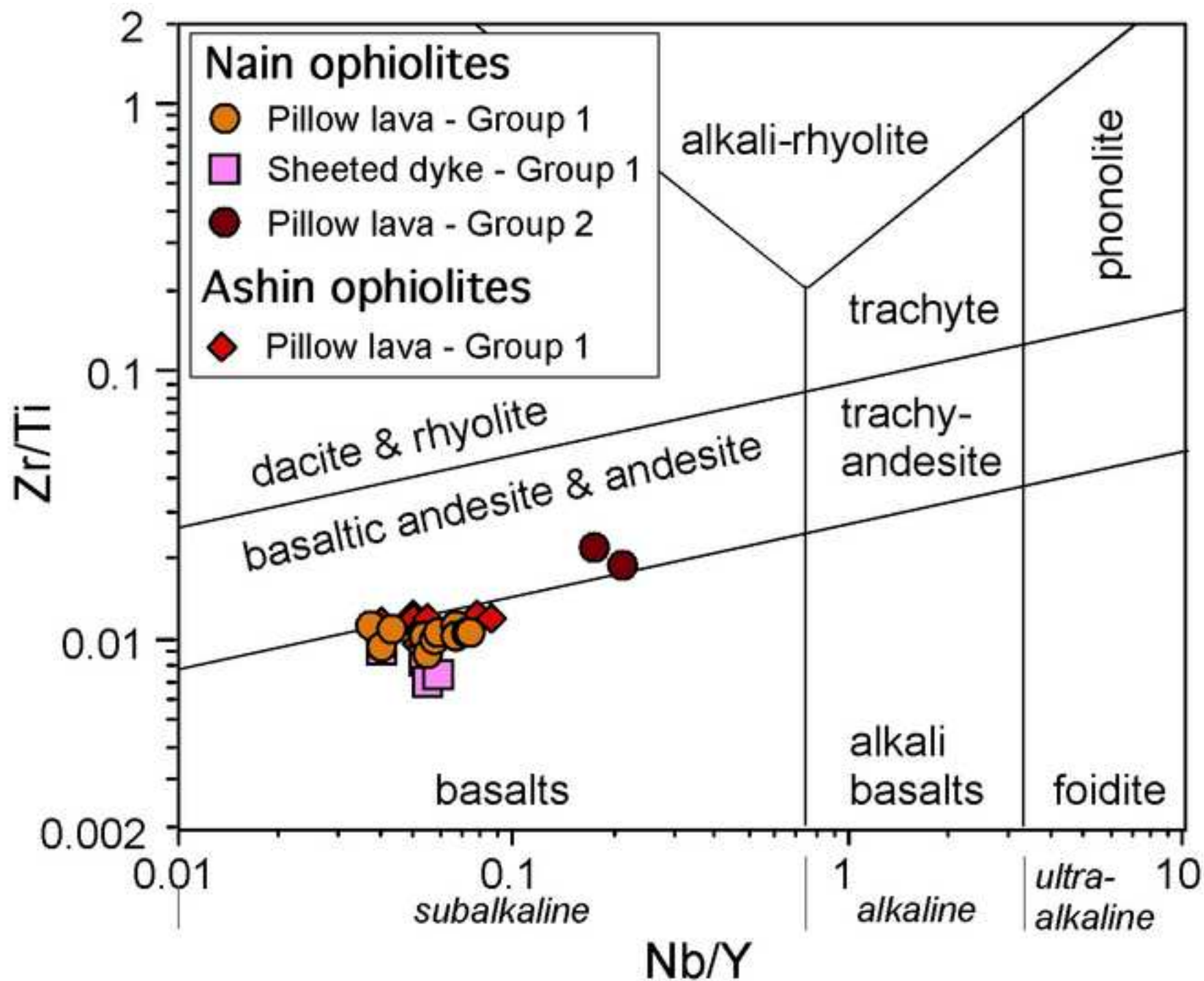
Fig. 6
Click here to download high resolution image
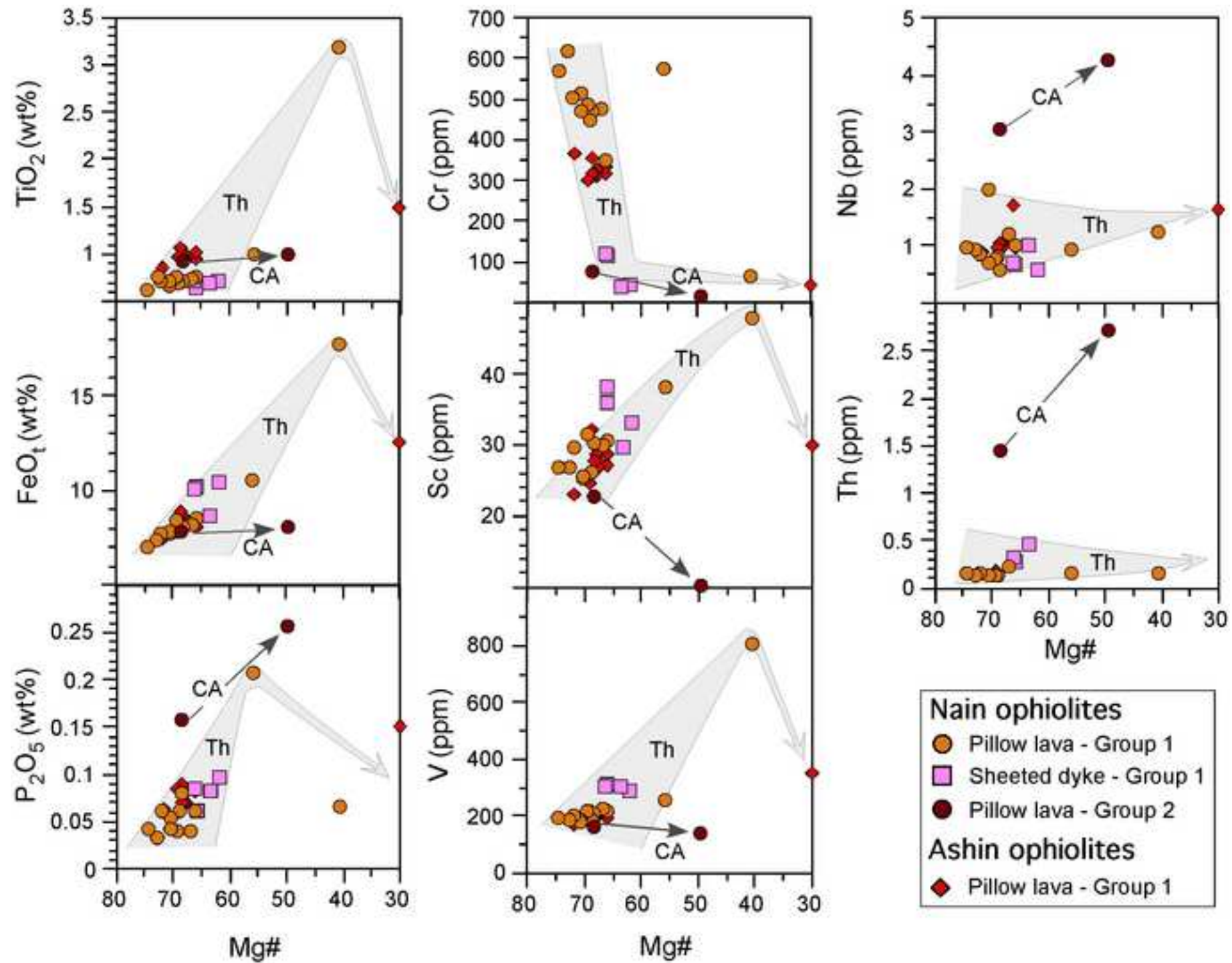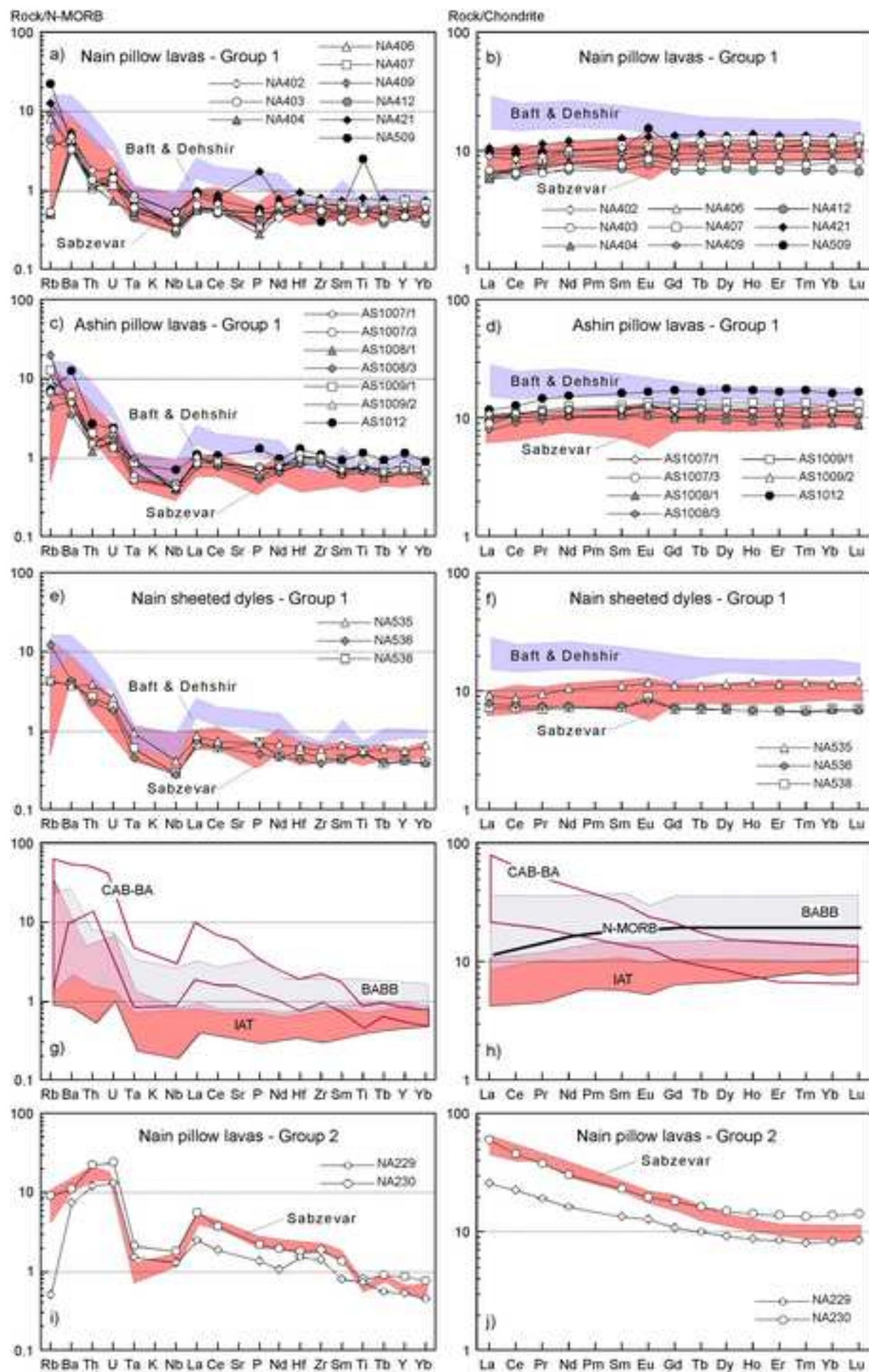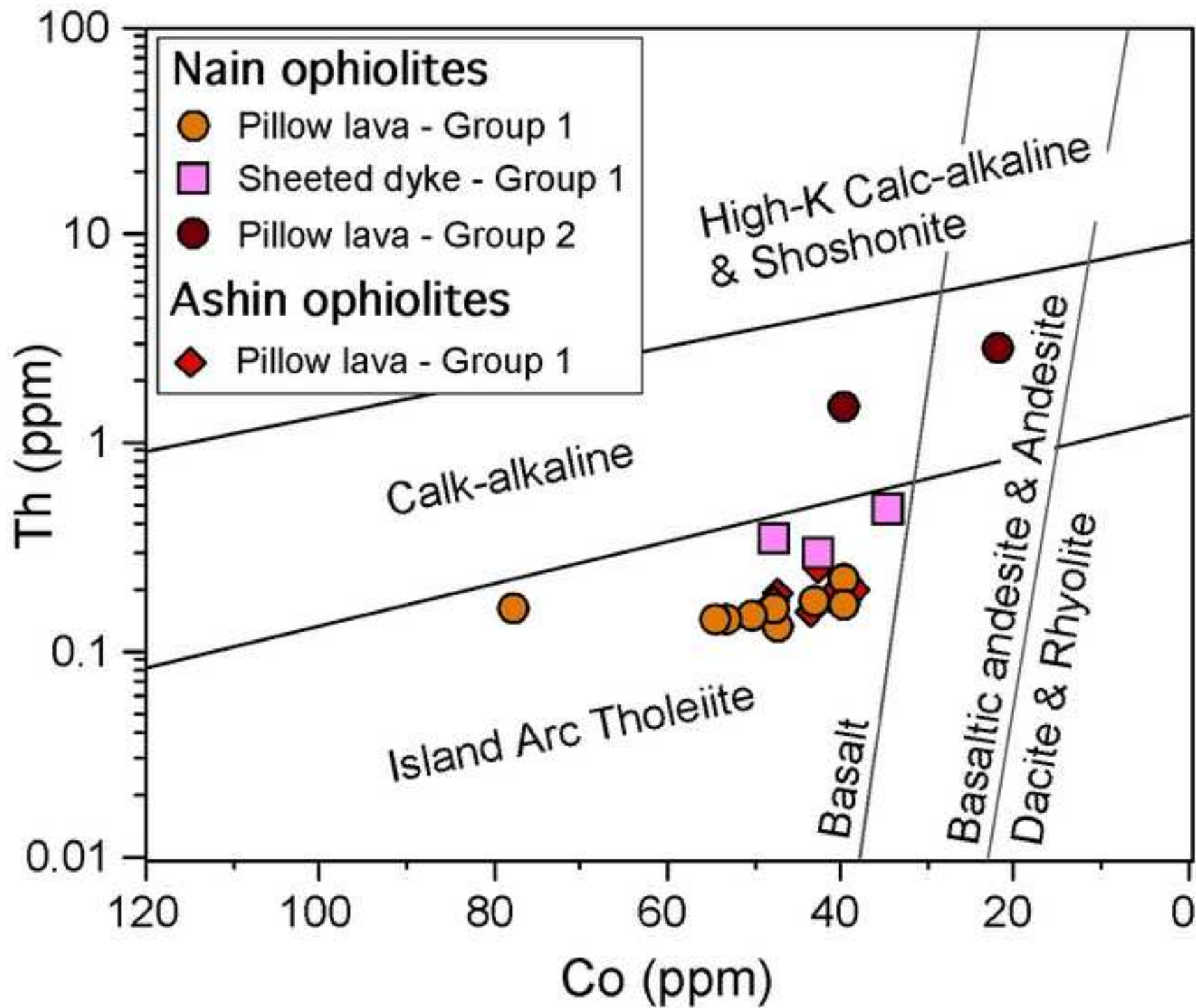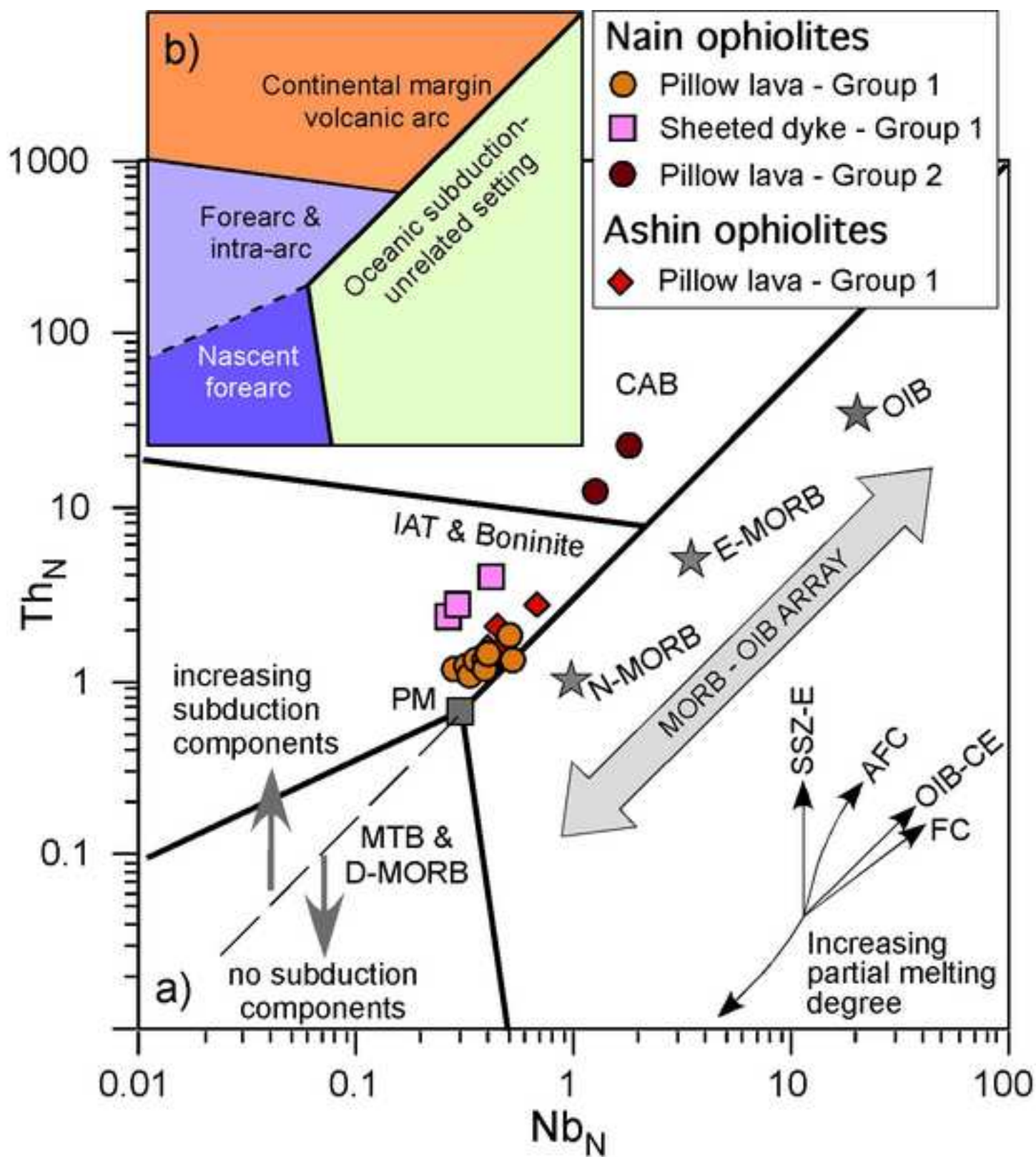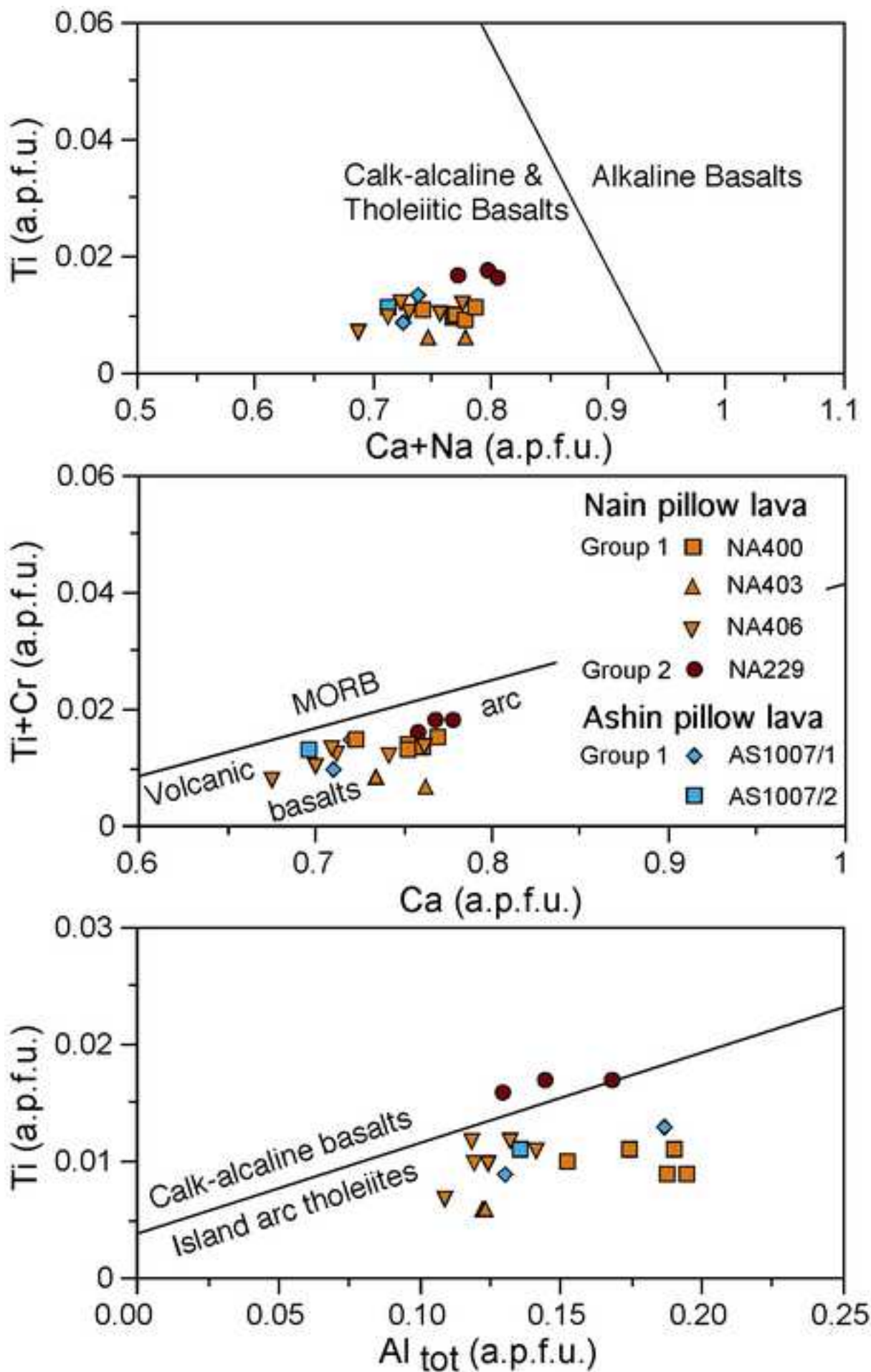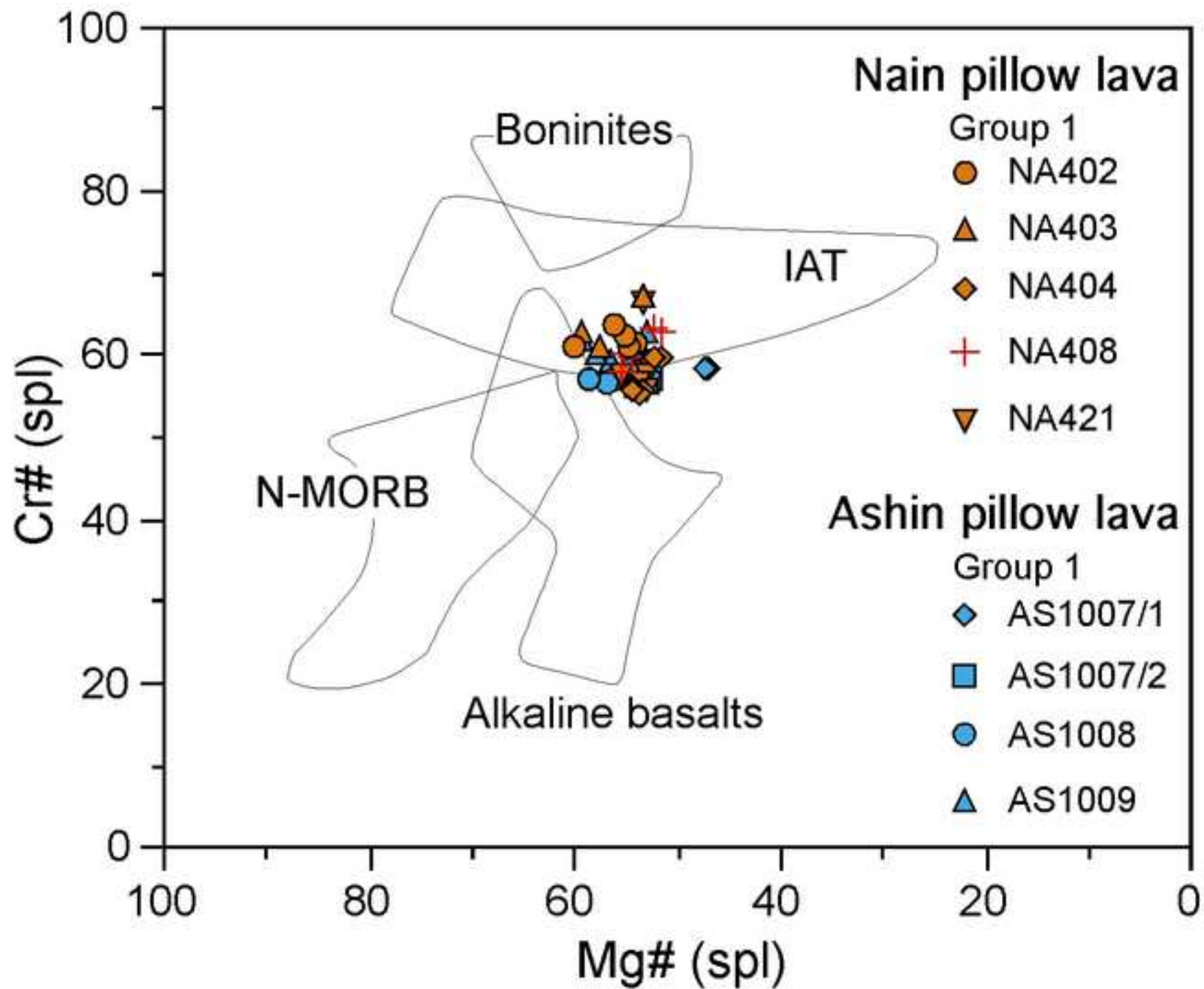
Fig. 13
Click here to download high resolution image

Fig. 14
Click here to download high resolution image

a) Group 1 pillow lavas

b) Group 1 sheeted dykes
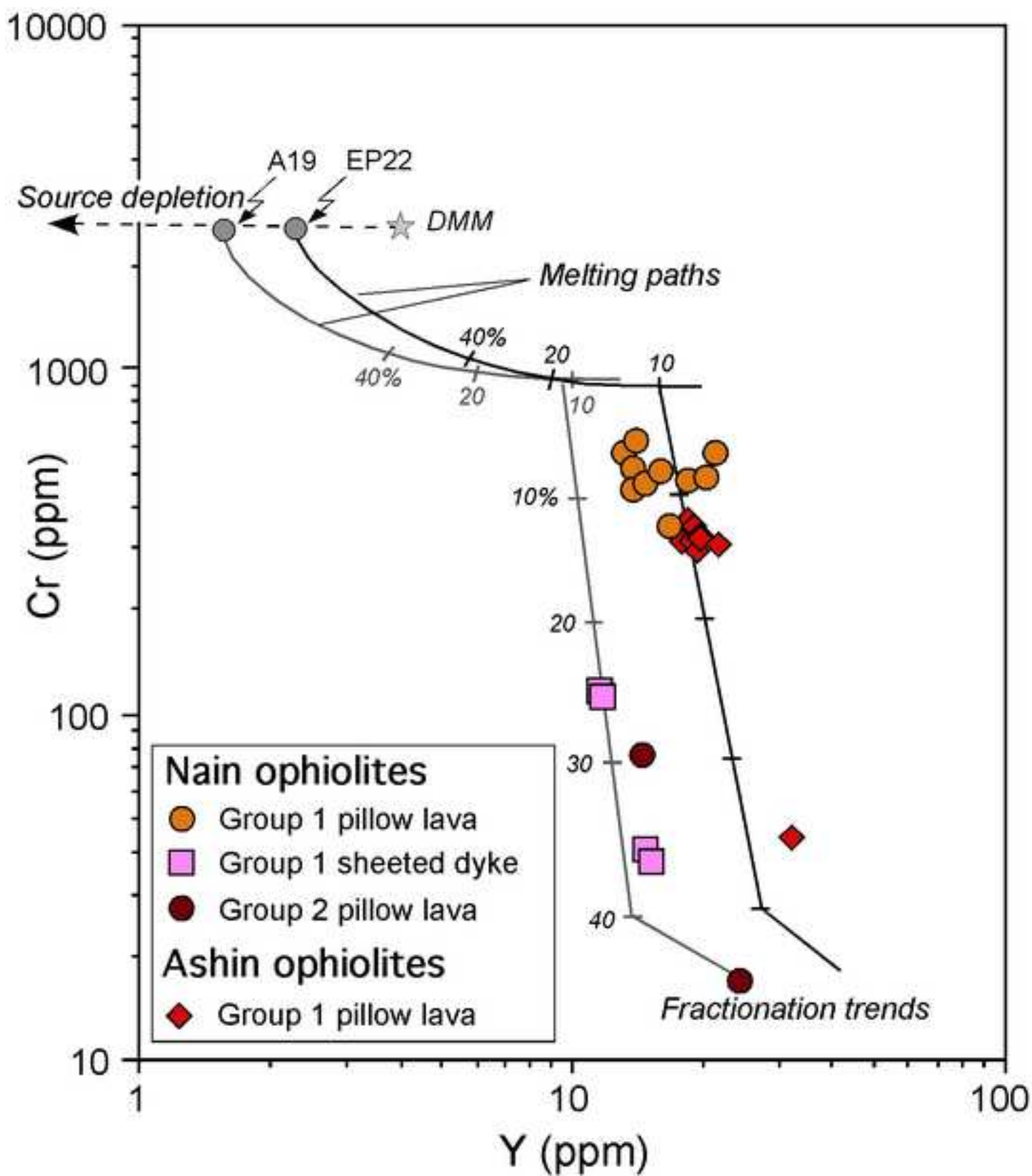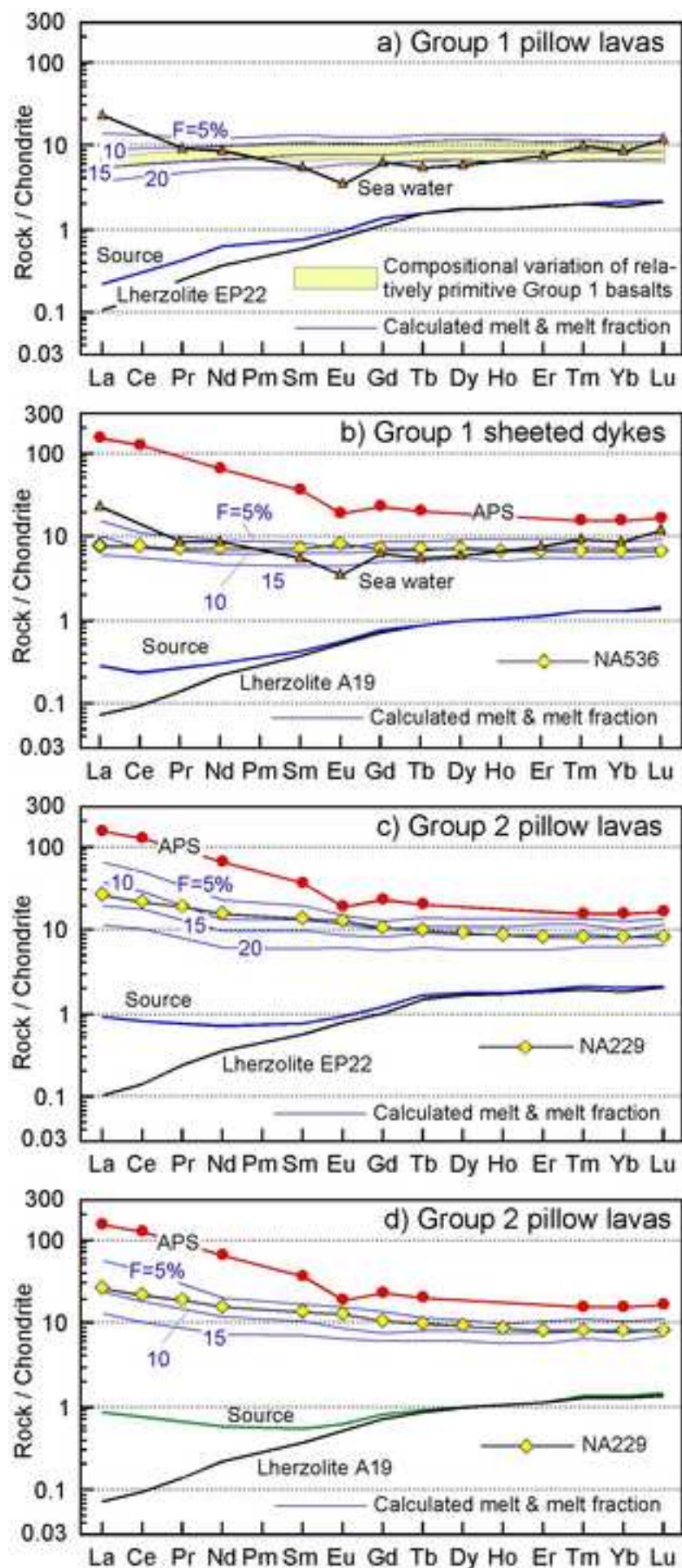
c) Group 2 pillow lavas

d) Group 2 pillow lavas

Fig. 15
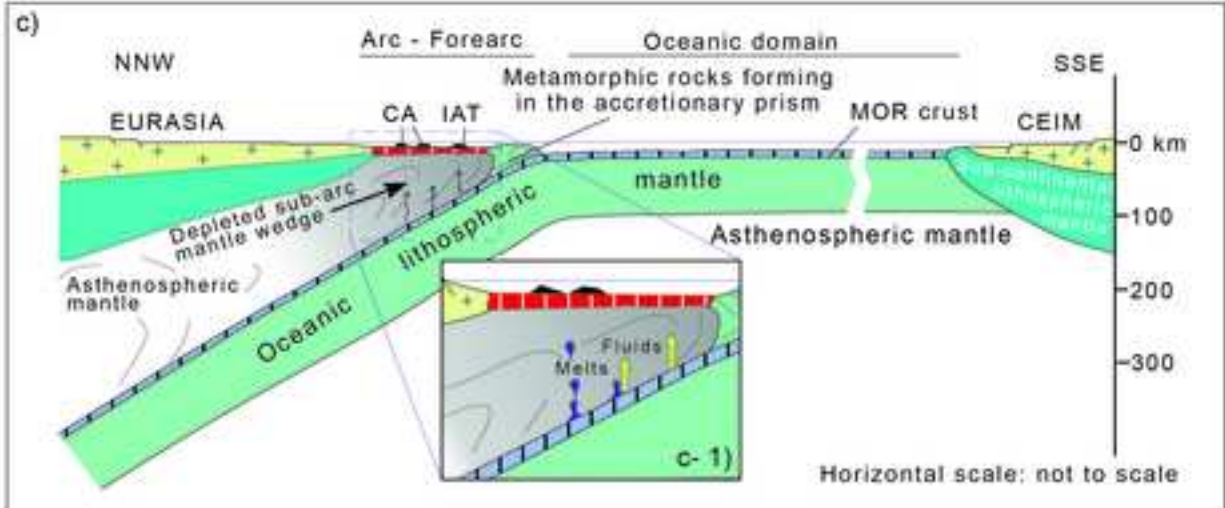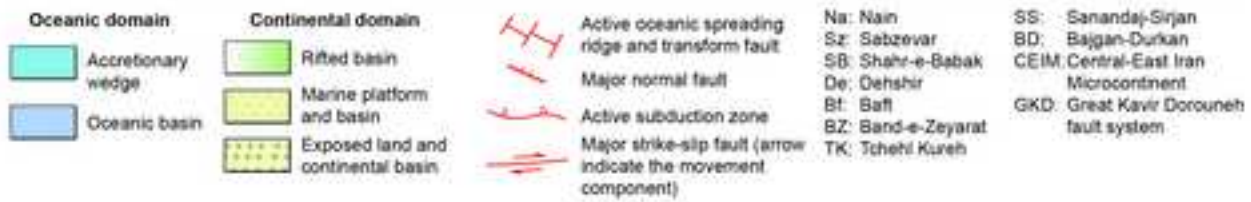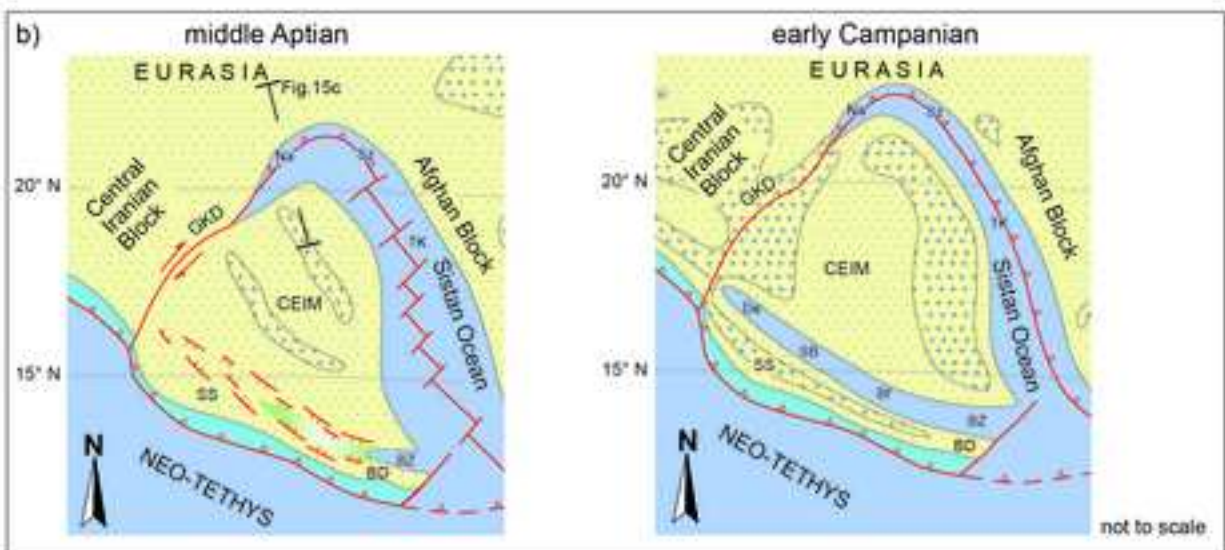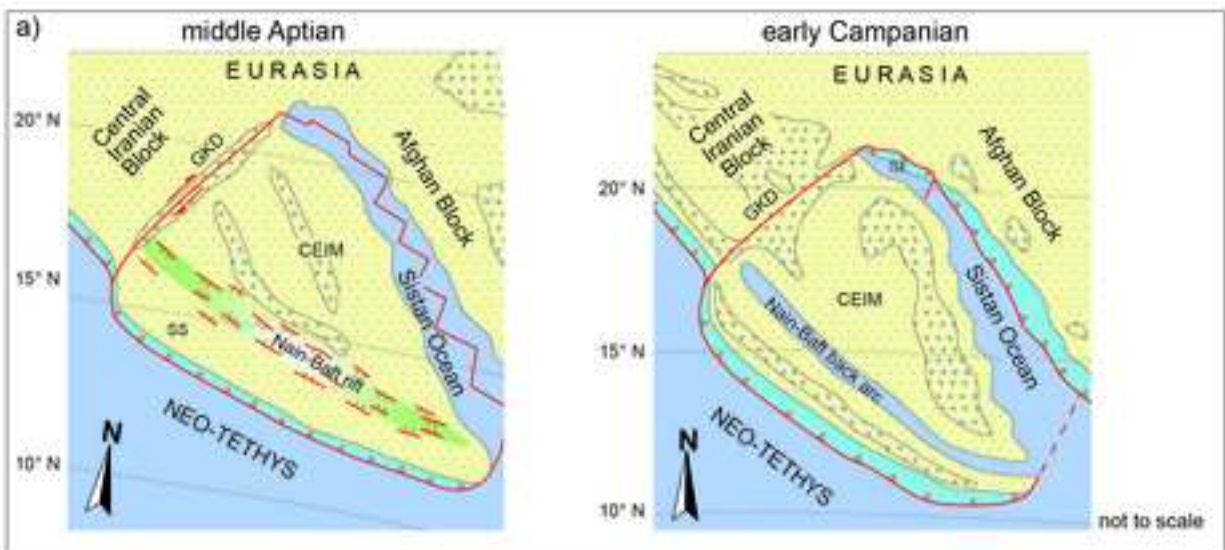
Table 1

Table 1 (1/3).

	Nain Ophiolites									
	Group 1 (IAT) pillow lavas									
Latitude	33°09'36.5"	33°09'36.5"	33°09'36.5"	33°09'36.5"	33°09'36.5"	33°09'36.5"	33°09'36.5"	33°09'36.5"	33°09'36.5"	33°09'36.5"
Longitude	53°00'8.02"	53°00'8.02"	53°00'8.02"	53°00'8.02"	53°00'8.02"	53°00'8.02"	53°00'8.02"	53°00'8.02"	53°00'8.02"	53°00'8.02"
Sample	NA400	NA402	NA403	NA404	NA405	NA406	NA407	NA408	NA409	NA412
Rock	basalt	basalt	basalt	basalt	basalt	basalt	basalt	basalt	basalt	basalt
XRF Analyses:										
SiO_2	47.81	49.19	47.41	50.94	47.84	47.04	49.68	48.37	48.96	45.88
TiO_2	0.73	0.73	0.60	0.75	0.68	0.65	0.76	0.69	0.70	0.64
Al_2O_3	14.26	13.74	12.61	13.92	12.40	14.00	14.69	13.31	14.77	13.25
Fe_2O_3	1.09	1.05	0.88	0.94	0.99	0.99	1.11	1.03	0.99	0.96
FeO	7.29	7.03	5.89	6.27	6.60	6.60	7.38	6.88	6.63	6.40
MnO	0.15	0.15	0.14	0.14	0.13	0.14	0.15	0.14	0.14	0.13
MgO	7.93	7.94	9.65	9.41	8.88	8.20	9.41	8.33	9.59	8.59
CaO	13.36	14.39	15.97	12.13	14.76	13.18	12.86	13.07	11.79	15.16
Na_2O	3.31	2.87	2.28	2.32	2.97	3.50	3.10	3.64	3.25	3.15
K_2O	0.50	0.11	0.03	0.01	b.d.l.	0.56	0.00	0.61	0.54	0.54
P_2O_5	0.06	0.04	0.04	0.03	0.04	0.06	0.04	0.08	0.06	0.05
L.O.I.	4.07	3.56	5.28	2.32	5.16	5.32	1.35	4.60	2.99	4.80
Total	100.56	100.78	100.78	99.19	100.44	100.24	100.52	100.74	100.41	99.56
Mg#	66.0	66.8	74.5	72.8	70.5	68.9	69.5	68.3	72.0	70.5
Zn	64	67	53	57	60	58	72	62	65	55
Cu	53	79	76	80	80	35	82	77	80	80
Sc	31	30	27	27	26	26	31	30	30	25
Ga	12	13	12	12	12	12	13	11	11	12
Ni	69	136	192	220	199	105	169	91	133	134
Co	42	40	43	53	46	47	50	42	48	55
Cr	352	479	570	619	516	451	485	470	504	471
V	218	226	197	185	177	186	219	213	202	188
Ba	27	30	21.4	24	20	20	28	25	22	21
Pb	10	9	9	8	10	7	7	8	10	8
ICP-MS Analyses (= XRF analyses):*										
Rb	4*	2.06	0.305	0.286	5*	4.61	0.280	6*	5.19	2.50
Sr	200*	150	119	112	128*	161	113	183*	154	144
Y	17*	18.6	13.3	14.2	14*	14.0	20.5	15*	16.0	12.6
Zr	49*	51.4	40.3	48.1	45*	41.0	52.7	41*	44.7	36.7
La	b.d.l.*	2.17	1.64	1.37	b.d.l.*	1.50	1.44	b.d.l.*	1.59	1.40
Ce	b.d.l.*	5.23	4.03	4.13	b.d.l.*	4.40	4.45	b.d.l.*	4.35	3.81
Pr		0.862	0.621	0.688		0.724	0.798		0.741	0.640
Nd	4*	4.81	3.37	3.71	b.d.l.*	3.75	4.67	5*	4.17	3.26
Sm		1.64	1.17	1.31		1.29	1.72		1.47	1.08
Eu		0.625	0.491	0.574		0.534	0.638		0.554	0.447
Gd		2.24	1.57	1.78		1.75	2.35		1.96	1.41
Tb		0.412	0.290	0.325		0.326	0.448		0.360	0.261
Dy		2.90	2.00	2.23		2.24	3.18		2.56	1.79
Ho		0.644	0.442	0.484		0.484	0.716		0.574	0.391
Er		1.83	1.30	1.42		1.43	2.03		1.66	1.15
Tm		0.288	0.198	0.217		0.216	0.318		0.260	0.175
Yb		1.87	1.36	1.48		1.46	2.09		1.65	1.18
Lu		0.288	0.204	0.219		0.217	0.322		0.255	0.172
Nb	1*	1.23	0.977	0.946	1*	0.801	0.772	1*	0.854	0.689
Hf		1.30	1.18	1.41		1.31	1.35		1.14	1.13
Ta		0.116	0.080	0.069		0.077	0.105		0.086	0.061
Th	b.d.l.*	0.219	0.167	0.140	b.d.l.*	0.128	0.145	b.d.l.*	0.157	0.137
U		0.085	0.068	0.035		0.071	0.054		0.054	0.059
Ti/V	21	20	19	25	24	22	21	20	21	22
Nb/Y	0.06	0.07	0.07	0.07	0.07	0.06	0.04	0.04	0.05	0.05
$(La/Sm)_N$		0.85	0.90	0.67		0.75	0.54		0.70	0.84
$(Sm/Yb)_N$		0.98	0.95	0.98		0.98	0.91		0.99	1.02
$(La/Yb)_N$		0.83	0.86	0.66		0.74	0.50		0.69	0.85

Table 1 (2/3).

	Nain Ophiolites							
	Group 1 (IAT) pillow lavas		Group 2 (CAB) pillow lavas		Group 1 (IAT) sheeted dyke			
Latitude	33°09'19.2"	33°09'54.9"	33°09'5.6"	33°09'5.6"	33°09'02.7"	33°09'02.7"	33°09'02.7"	33°09'02.7"
Longitude	53°00'40.8"	53°01'00.0"	53°00'36.4"	53°00'36.4"	53°01'55.5"	53°01'55.5"	53°01'55.5"	53°01'55.5"
Sample	NA421	NA509	NA229	NA230	NA535	NA536	NA537	NA538
Rock	basalt	Fe-basalt	basalt	basalt	basalt	basalt	bas and	basalt
XRF Analyses:								
SiO_2	50.89	45.39	50.81	51.53	52.09	51.20	52.61	50.55
TiO_2	0.98	3.06	0.90	0.96	0.69	0.63	0.69	0.69
Al_2O_3	13.89	15.72	16.26	15.32	11.62	14.37	13.48	14.08
Fe_2O_3	1.36	2.25	0.99	1.01	1.12	1.31	1.34	1.29
FeO	9.09	15.03	6.63	6.73	7.46	8.75	8.91	8.62
MnO	0.15	0.17	0.14	0.11	0.17	0.20	0.17	0.20
MgO	6.48	5.78	8.07	3.72	7.27	9.49	8.12	9.47
CaO	8.75	5.03	7.12	8.38	12.42	7.11	6.79	8.03
Na_2O	5.07	3.29	5.05	6.76	4.47	3.29	4.20	3.78
K_2O	0.72	0.50	0.02	0.28	0.14	0.98	0.38	0.40
P_2O_5	0.20	0.06	0.15	0.24	0.08	0.06	0.09	0.08
LOI	3.40	2.96	4.29	4.77	2.59	2.76	2.35	2.69
Total	100.99	99.26	100.44	99.80	100.12	100.15	99.12	99.89
Mg#	55.9	40.7	68.4	49.6	63.5	65.9	61.9	66.2
Zn	189	212	76	68	28	42	49	40
Cu	24	27	106	24	106	50	32	13
Sc	38	48	23	10	30	38	33	36
Ga	12	21	16	20	15	14	13	13
Ni	41	39	12	b.d.l.	13	23	12	22
Co	40	78	40	22	35	43	47	48
Cr	574	68	77	17	38	114	41	117
V	258	807	166	137	306	308	292	303
Ba	34	25	47	71	24	27	24	25
Pb	10	7	14	21	10	7	7	10
ICP-MS Analyses (* = XRF analyses):								
Rb	7.07	12.7	0.289	5.06	2.48	6.71	3*	2.42
Sr	203	253	190	577	109	125	133*	71
Y	21.6	15.8	14.7	24.6	15.5	11.8	15*	11.6
Zr	65.7	33.1	107	136	35.7	27.3	39*	31.5
La	2.51	2.35	6.24	14.15	2.20	1.88	b.d.l.*	1.73
Ce	6.42	5.81	13.87	27.9	5.46	4.65	b.d.l.*	4.48
Pr	1.09	0.920	1.83	3.57	0.908	0.708		0.679
Nd	5.73	4.86	7.70	14.4	5.01	3.52	4*	3.41
Sm	1.95	1.63	2.10	3.58	1.73	1.15		1.13
Eu	0.765	0.896	0.742	1.16	0.681	0.488		0.525
Gd	2.82	2.25	2.23	3.72	2.29	1.50		1.47
Tb	0.523	0.415	0.376	0.608	0.412	0.270		0.264
Dy	3.46	2.93	2.38	3.84	2.94	1.82		1.81
Ho	0.782	0.641	0.504	0.812	0.665	0.393		0.390
Er	2.26	1.82	1.42	2.33	1.91	1.15		1.15
Tm	0.346	0.292	0.209	0.347	0.304	0.173		0.176
Yb	2.26	1.90	1.40	2.34	1.97	1.18		1.21
Lu	0.339	0.298	0.216	0.362	0.309	0.176		0.181
Nb	0.940	1.26	3.05	4.27	0.994	0.645	1*	0.691
Hf	1.97	1.16	3.129	3.709	1.288	0.908		1.148
Ta	0.088	0.109	0.203	0.276	0.126	0.061		0.079
Th	0.159	0.155	1.45	2.72	0.467	0.282	b.d.l.*	0.330
U	0.076	0.060	0.611	1.16	0.123	0.084		0.097
Ti/V	23	24	34	44	14	13	15	14
Nb/Y	0.04	0.08	0.21	0.17	0.06	0.05	0.04	0.06
$(La/Sm)_N$	0.83	0.93	1.92	2.55	0.82	1.06		0.99
$(Sm/Yb)_N$	0.96	0.95	1.66	1.70	0.98	1.08		1.03
$(La/Yb)_N$	0.80	0.88	3.19	4.33	0.80	1.14		1.02

Table 1 (3/3).

	Ashin Ophiolites									
	Group 1 (IAT) pillow lavas									
Latitude	33°31'33.3"	33°31'33.3"	33°31'06.4"	33°31'33.3"	33°31'37.7"	33°31'33.3"	33°31'43.2"	33°31'33.3"	33°31'33.3"	33°31'47.4"
Longitude	53°23'52.8"	53°23'52.8"	53°23'56.0"	53°23'52.8"	53°23'52.7"	53°23'52.8"	53°23'48.9"	53°23'52.8"	53°23'52.8"	53°23'48.4"
Sample	AS1007/1	AS1007/2	AS1007/3	AS1007/4	AS1008/1	AS1008/2	AS1008/3	AS1009/1	AS1009/2	AS1012
Rock	basalt	basalt	basalt	basalt	basalt	basalt	basalt	basalt	basalt	bas and
XRF Analyses:										
SiO_2	46.57	47.68	49.42	47.22	48.55	48.96	47.32	48.54	46.83	54.39
TiO_2	0.94	0.98	1.05	0.96	0.95	0.94	0.81	0.95	0.91	1.48
Al_2O_3	15.41	15.63	14.39	15.40	15.34	15.29	15.51	15.74	13.67	14.37
Fe_2O_3	1.07	1.09	1.15	1.08	1.06	1.06	0.95	1.09	1.03	1.65
FeO	7.12	7.26	7.68	7.18	7.08	7.03	6.33	7.26	6.86	10.99
MnO	0.13	0.17	0.14	0.14	0.14	0.14	0.13	0.12	0.13	0.17
MgO	8.94	7.93	9.43	8.48	8.51	8.60	9.04	8.48	7.47	2.66
CaO	11.85	10.94	9.70	12.26	11.64	11.46	11.85	11.05	14.47	5.82
Na_2O	3.29	3.59	4.02	3.42	3.65	3.75	3.25	3.55	4.01	7.24
K_2O	0.33	0.71	0.32	0.31	0.28	0.27	0.59	0.44	0.26	0.28
P_2O_5	0.08	0.08	0.09	0.08	0.07	0.07	0.06	0.07	0.08	0.15
LOI	3.85	3.31	2.72	3.82	2.96	3.13	3.94	3.29	5.22	0.85
Total	99.57	99.36	100.11	100.35	100.24	100.70	99.79	100.58	100.94	100.05
Mg#	69.1	66.0	68.6	67.8	68.2	68.5	71.8	67.6	66.0	30.1
Zn	64	67	75	66	68	65	54	67	70	108
Cu	64	66	71	68	71	71	69	70	68	22
Sc	25	27	32	27	29	28	23	28	29	30
Ga	14	14	12	14	13	13	13	14	14	11
Ni	81	75	59	75	71	65	119	77	66	
Co	48	51	41	43	44	37	48	43	39	49
Cr	298	334	355	328	317	317	368	309	315	44
V	194	193	219	205	205	201	172	200	207	348
Ba	32	35.5	40	41	33	32	22	36	42	81
Pb	10	6	8	10	6	9	8	7	11	13
ICP-MS Analyses (* = XRF analyses):										
Rb	3.80	7*	3.70	2*	2.57	2*	11.2	7.11	5.39	4.10
Sr	297	211*	219	277*	222	244*	335	279	262	332
Y	19.7	20*	19.3	20*	19.0	18*	18.8	21.9	23.8	32.4
Zr	71.2	74*	78.2	71*	64.7	71*	59.8	73.0	66.7	87.1
La	2.59	b.d.l.*	2.15	b.d.l.*	2.48	b.d.l.*	1.92	2.34	2.52	2.80
Ce	6.91	8*	6.63	6*	6.40	6*	5.71	6.74	6.77	7.86
Pr	1.10		1.10		1.01		0.936	1.13	1.11	1.39
Nd	5.60	5*	5.61	6*	5.03	5*	4.80	5.83	5.61	7.32
Sm	1.84		1.87		1.63		1.61	1.96	1.88	2.49
Eu	0.738		0.722		0.621		0.661	0.779	0.764	0.975
Gd	2.42		2.47		2.08		2.13	2.79	2.50	3.57
Tb	0.439		0.454		0.376		0.396	0.489	0.470	0.639
Dy	3.00		3.07		2.51		2.72	3.46	3.24	4.49
Ho	0.650		0.659		0.536		0.590	0.767	0.718	0.987
Er	1.90		1.92		1.54		1.74	2.17	2.11	2.78
Tm	0.289		0.287		0.232		0.263	0.342	0.323	0.439
Yb	1.96		1.94		1.56		1.82	2.16	2.25	2.81
Lu	0.290		0.284		0.226		0.269	0.333	0.337	0.426
Nb	0.979	2*	1.06	1*	0.984	1*	0.911	1.08	0.955	1.65
Hf	2.06		2.26		1.81		1.70	2.148	1.880	2.719
Ta	0.080		0.071		0.070		0.131	0.113	0.110	0.112
Th	0.182	b.d.l.*	0.178	b.d.l.*	0.147	b.d.l.*	0.168	0.244	0.187	0.332
U	0.109		0.065		0.081		0.073	0.065	0.097	0.112
Ti/V	30	32	29	29	28	29	30	29	27	26
Nb/Y	0.05	0.09	0.06	0.05	0.05	0.08	0.05	0.05	0.04	0.05
$(La/Sm)_N$	0.91		0.74		0.98		0.77	0.77	0.87	0.73
$(Sm/Yb)_N$	1.04		1.07		1.16		0.98	1.01	0.93	0.99
$(La/Yb)_N$	0.95		0.80		1.14		0.76	0.78	0.80	0.71

Table 2

Table 2.

	NA400			NA403		NA406			NA229			AS1007/1		AS1007/2
Locality - Unit	Nain ophiolites - Pillow lavas											Ashin ophiolites - Pillow lavas		
Rock Group	Group 1 (Island Arc Tholeiite)								Group 2 (Calc-alkaline)			Group 1 (Island Arc Tholeiite)		
Sample	NA400			NA403		NA406			NA229			AS1007/1		AS1007/2
Rock type	basalt			basalt		basalt			basalt			basalt		basalt
Mineral	cpx 1-19	cpx 3-22	cpx 10-28	cpx 5-1	cpx 5-2	cpx 4-3	cpx 8-10	cpx 9-11	cpx 1-1	cpx 1-2	cpx 8-10	cpx 10-20	cpx 11-21	cpx 1-1
Mineral type	Augite	Augite	Augite	Augite	Augite	Augite	Augite	Augite	Augite	Augite	Augite	Augite	Augite	Augite
SiO_2	51.31	51.00	51.17	52.25	53.78	53.06	52.77	52.84	52.30	52.06	51.56	51.29	53.26	51.90
TiO_2	0.40	0.35	0.34	0.21	0.22	0.27	0.44	0.37	0.63	0.58	0.61	0.48	0.32	0.41
Al_2O_3	4.02	3.49	4.49	2.88	2.90	2.58	3.11	2.90	3.35	3.00	3.93	4.37	3.03	3.13
Cr_2O_3	0.15	0.12	0.16	0.04	0.09	0.03	0.07	0.08	0.04	0.07	0.05	0.06	0.04	0.07
FeO	7.24	8.57	5.92	5.44	5.10	5.70	5.34	7.07	6.40	6.28	6.74	7.15	5.49	7.60
MnO	0.18	0.23	0.18	0.17	0.15	0.21	0.14	0.20	0.17	0.10	0.20	0.14	0.22	0.21
MgO	16.62	16.23	17.33	18.88	19.31	20.64	18.75	18.05	17.05	17.32	17.67	18.02	18.61	18.19
CaO	19.53	18.93	19.06	19.57	19.07	17.51	19.73	19.10	19.63	19.82	19.13	18.49	18.19	17.71
Na_2O	0.27	0.25	0.23	0.23	0.19	0.20	0.22	0.25	0.42	0.41	0.39	0.26	0.22	0.26
K_2O	0.00	0.00	0.00	0.00	0.01	0.00	0.00	0.00	0.00	0.00	0.00	0.00	0.00	0.00
Total	99.72	99.17	98.89	99.66	100.82	100.20	100.57	100.86	99.98	99.64	100.27	100.25	99.37	99.49
Fe_2O_3	1.76	2.08	1.10	3.00	0.53	2.64	1.91	1.73	1.05	1.95	2.82	2.82	0.00	1.91
FeO	5.65	6.70	4.93	2.74	4.62	3.33	3.62	5.51	5.45	4.53	4.20	4.61	5.49	5.88
Total	99.89	99.38	99.00	99.96	100.87	100.46	100.77	101.03	100.09	99.84	100.56	100.54	99.37	99.68
Si	1.885	1.892	1.884	1.899	1.931	1.909	1.903	1.912	1.910	1.906	1.873	1.863	1.941	1.903
Ti	0.011	0.010	0.009	0.006	0.006	0.007	0.012	0.010	0.017	0.016	0.017	0.013	0.009	0.011
Al	0.174	0.153	0.195	0.123	0.123	0.109	0.132	0.124	0.144	0.129	0.168	0.187	0.130	0.135
Cr	0.004	0.004	0.005	0.001	0.003	0.001	0.002	0.002	0.001	0.002	0.002	0.002	0.001	0.002
Fe^{3+}	0.049	0.058	0.031	0.082	0.014	0.071	0.052	0.047	0.029	0.054	0.077	0.077	0.000	0.053
Fe^{2+}	0.174	0.208	0.152	0.083	0.139	0.100	0.109	0.167	0.166	0.139	0.128	0.140	0.167	0.180
Mn	0.006	0.007	0.006	0.005	0.004	0.006	0.004	0.006	0.005	0.003	0.006	0.004	0.007	0.007
Mg	0.910	0.898	0.951	1.023	1.033	1.107	1.008	0.974	0.928	0.945	0.957	0.976	1.011	0.994
Ca	0.768	0.752	0.752	0.762	0.734	0.675	0.762	0.740	0.768	0.777	0.745	0.720	0.710	0.696
Na	0.019	0.018	0.016	0.016	0.013	0.014	0.015	0.018	0.030	0.029	0.027	0.018	0.015	0.019
K	0.000	0.000	0.000	0.000	0.000	0.000	0.000	0.000	0.000	0.000	0.000	0.000	0.000	0.000
Total	4.000	4.000	4.000	4.000	4.000	4.000	4.000	4.000	4.000	4.000	4.000	4.000	3.992	4.000
Al (iv)	0.115	0.108	0.116	0.101	0.069	0.091	0.097	0.088	0.090	0.094	0.127	0.137	0.059	0.097
Al (vi)	0.059	0.045	0.079	0.022	0.053	0.018	0.035	0.036	0.055	0.035	0.042	0.050	0.071	0.038
Wo (%)	40.0	38.9	39.5	38.8	37.9	34.3	39.2	38.1	40.0	40.0	38.5	37.3	37.3	35.8
En (%)	47.4	46.4	50.0	52.0	53.5	56.3	51.8	50.0	48.3	48.6	49.5	50.5	53.1	51.2
Fs (%)	11.6	13.7	9.6	8.4	7.9	8.7	8.3	11.0	10.2	9.9	10.6	11.2	8.8	12.0
Acm (%)	1.0	0.9	0.9	0.8	0.7	0.7	0.8	0.9	1.6	1.5	1.4	0.9	0.8	1.0
Mg#	80.4	77.2	83.9	86.1	87.1	86.6	86.2	82.0	82.6	83.1	82.4	81.8	85.8	81.0
T(°C)*	1195 ± 3			1223 ± 7		1192 ± 5			1223 ± 6			1224 ± 8		1205
P(GPa)*	0.29 ± 0.06			0.29 ± 0.08		0.22 ± 0.05			0.61 ± 0.03			0.54 ± 0.01		0.52

Table 3

Table 3 (1/3)

Locality - unit	Nain - Pillow lavas													
Sample	NA402 basalt					NA403 basalt			NA404 basalt				NA408 basalt	
Mineral	spl 1c	spl 1r	spl 2c	spl 2r	spl 4c	spl 9c	spl 10c	spl 11c	spl 1c	spl 1r	spl 8c	spl 8r	spl 9c	spl 9r
Mineral type	Al-Chr	Al-Chr	Al-Chr	Al-Chr	Al-Chr	Al-Chr	Al-Chr	Al-Chr	Al-Chr	Al-Chr	Al-Chr	Al-Chr	Al-Chr	Al-Chr
TiO_2	0,30	0,26	0,27	0,29	0,29	0,23	0,25	0,20	0,26	0,32	0,35	0,29	0,28	0,31
Al_2O_3	19,72	19,99	18,96	18,20	20,09	19,88	16,44	19,32	23,67	23,22	21,17	20,99	21,77	20,70
Cr_2O_3	46,27	46,04	45,66	46,52	45,98	45,33	49,37	47,79	42,50	43,09	45,54	45,77	43,90	44,66
V_2O_3	0,08	0,09	0,17	0,11	0,14	0,15	0,12	0,09	0,20	0,17	0,27	0,17	0,18	0,12
FeO	21,91	22,19	22,61	22,73	20,12	21,53	22,15	19,86	20,91	21,05	21,56	21,64	22,53	22,26
MnO	0,26	0,24	0,31	0,24	0,31	0,19	0,35	0,29	0,29	0,32	0,29	0,26	0,23	0,23
MgO	11,61	11,88	11,75	12,01	12,94	12,36	11,23	12,74	11,62	11,79	11,10	11,29	12,12	11,74
CaO	0,00	0,00	0,00	0,00	0,00	0,00	0,00	0,00	0,00	0,00	0,00	0,00	0,00	0,00
ZnO	0,00	0,01	0,04	0,00	0,03	0,05	0,03	0,07	0,01	0,04	0,00	0,01	0,04	0,05
NiO	0,14	0,06	0,13	0,04	0,12	0,16	0,12	0,11	0,05	0,13	0,15	0,12	0,05	0,12
Total	100,28	100,75	99,90	100,14	100,01	99,89	100,05	100,46	99,51	100,14	100,42	100,55	101,09	100,18
Ti	0,007	0,006	0,006	0,007	0,007	0,005	0,006	0,005	0,006	0,007	0,008	0,007	0,006	0,007
Al	0,726	0,731	0,701	0,673	0,733	0,730	0,616	0,706	0,863	0,843	0,777	0,769	0,786	0,759
Cr	1,142	1,129	1,133	1,153	1,126	1,116	1,241	1,172	1,040	1,049	1,121	1,125	1,064	1,098
V	0,002	0,002	0,004	0,003	0,003	0,004	0,003	0,002	0,005	0,004	0,007	0,004	0,004	0,003
Fe^{3+}	0,116	0,126	0,149	0,158	0,124	0,139	0,128	0,111	0,080	0,089	0,080	0,089	0,133	0,126
Fe^{2+}	0,456	0,449	0,444	0,438	0,397	0,421	0,461	0,404	0,461	0,454	0,482	0,474	0,445	0,453
Mn	0,007	0,006	0,008	0,006	0,008	0,005	0,009	0,008	0,008	0,008	0,008	0,007	0,006	0,006
Mg	0,540	0,549	0,550	0,561	0,598	0,574	0,532	0,589	0,536	0,541	0,515	0,523	0,554	0,544
Ca	0,000	0,000	0,000	0,000	0,000	0,000	0,000	0,000	0,000	0,000	0,000	0,000	0,000	0,000
Zn	0,000	0,000	0,001	0,000	0,001	0,001	0,001	0,002	0,000	0,001	0,000	0,000	0,001	0,001
Ni	0,003	0,001	0,003	0,001	0,003	0,004	0,003	0,003	0,001	0,003	0,004	0,003	0,001	0,003
Total	3,000	3,000	3,000	3,000	3,000	3,000	3,000	3,000	3,000	3,000	3,000	3,000	3,000	3,000
Fe_2O_3	4,92	5,41	6,31	6,70	5,31	5,95	5,35	4,75	3,44	3,82	3,40	3,80	5,76	5,38
FeO	17,48	17,32	16,93	16,71	15,34	16,18	17,34	15,58	17,82	17,61	18,50	18,22	17,35	17,42
Total	100,77	101,30	100,54	100,81	100,54	100,48	100,58	100,93	99,86	100,52	100,76	100,93	101,67	100,72
Mg#	54,21	55,01	55,31	56,17	60,06	57,65	53,58	59,30	53,76	54,40	51,68	52,48	55,46	54,56
Cr#	61,15	60,71	61,76	63,16	60,56	60,47	66,83	62,39	54,63	55,45	59,06	59,39	57,49	59,14
TiO_2 (liquid)	0,75	0,69	0,70	0,73	0,72	0,62	0,66	0,57	0,68	0,77	0,81	0,72	0,71	0,76
Al_2O_3 (liquid)	14,50	14,55	14,37	14,23	14,57	13,75	12,71	13,59	15,14	15,08	14,75	14,72	14,85	14,67
TiO_2 (rock)	0,74					0,60			0,77				0,71	
Al_2O_3 (rock)	13,73					12,61			14,37				13,84	

Table 3 (2/3)

Locality - unit	Nain - Pillow lavas								Ashin - Pillow lavas					
Sample	NA408 basalt				NA421 basalt				AS1007/1 basalt					
Mineral	spl 13c	spl 13r	spl 18c	spl 18r	spl 14c	spl 14r	spl 18c	spl 18r	spl 1c	spl 1r	spl 6c	spl 6r	spl 8c	spl 8r
Mineral type	Al-Chr	Al-Chr	Al-Chr	Al-Chr	Al-Chr	Al-Chr	Al-Chr	Al-Chr	Al-Chr	Al-Chr	Al-Chr	Al-Chr	Al-Chr	Al-Chr
TiO_2	0,25	0,28	0,29	0,29	0,47	0,46	0,42	0,44	0,53	0,43	0,35	0,38	0,42	0,39
Al_2O_3	19,82	20,12	18,84	19,04	22,24	21,69	23,21	22,68	21,33	21,42	21,07	20,48	22,12	22,19
Cr_2O_3	45,67	44,46	47,03	46,72	44,20	44,14	42,78	43,15	43,36	43,67	45,86	45,80	44,31	44,14
V_2O_3	0,28	0,18	0,15	0,24	0,13	0,17	0,15	0,23	0,22	0,29	0,14	0,16	0,20	0,17
FeO	22,85	22,53	22,75	23,02	21,05	21,60	21,24	21,61	23,80	23,85	21,67	21,55	20,79	21,26
MnO	0,22	0,26	0,27	0,38	0,32	0,32	0,28	0,31	0,33	0,38	0,26	0,25	0,24	0,27
MgO	11,80	11,81	11,20	10,99	11,47	11,38	11,52	11,70	10,07	10,11	11,29	11,66	11,85	11,41
CaO	0,00	0,00	0,00	0,00	0,00	0,00	0,00	0,00	0,00	0,00	0,00	0,00	0,00	0,00
ZnO	0,03	0,09	0,00	0,02	0,10	0,03	0,03	0,03	0,06	0,05	0,03	0,00	0,01	0,00
NiO	0,09	0,04	0,04	0,05	0,14	0,12	0,13	0,12	0,07	0,02	0,09	0,02	0,01	0,12
Total	101,01	99,77	100,56	100,75	100,13	99,92	99,77	100,28	99,78	100,21	100,75	100,30	99,95	99,94
Ti	0,006	0,007	0,007	0,007	0,011	0,011	0,010	0,010	0,013	0,010	0,008	0,009	0,010	0,009
Al	0,724	0,741	0,696	0,703	0,813	0,796	0,847	0,825	0,791	0,791	0,770	0,751	0,808	0,812
Cr	1,118	1,099	1,166	1,157	1,083	1,087	1,047	1,052	1,079	1,082	1,125	1,127	1,085	1,084
V	0,007	0,004	0,004	0,006	0,003	0,004	0,004	0,006	0,006	0,007	0,003	0,004	0,005	0,004
Fe^{3+}	0,139	0,143	0,121	0,121	0,079	0,092	0,083	0,097	0,099	0,099	0,085	0,100	0,083	0,081
Fe^{2+}	0,453	0,446	0,475	0,482	0,467	0,471	0,467	0,460	0,528	0,526	0,477	0,461	0,456	0,471
Mn	0,006	0,007	0,007	0,010	0,008	0,009	0,007	0,008	0,009	0,010	0,007	0,007	0,006	0,007
Mg	0,545	0,550	0,523	0,513	0,530	0,528	0,532	0,538	0,473	0,472	0,522	0,541	0,547	0,528
Ca	0,000	0,000	0,000	0,000	0,000	0,000	0,000	0,000	0,000	0,000	0,000	0,000	0,000	0,000
Zn	0,001	0,002	0,000	0,001	0,002	0,001	0,001	0,001	0,001	0,001	0,001	0,000	0,000	0,000
Ni	0,002	0,001	0,001	0,001	0,003	0,003	0,003	0,003	0,002	0,000	0,002	0,000	0,000	0,003
Total	3,000	3,000	3,000	3,000	3,000	3,000	3,000	3,000	3,000	3,000	3,000	3,000	3,000	3,000
Fe_2O_3	5,98	6,07	5,13	5,13	3,38	3,92	3,57	4,18	4,17	4,20	3,66	4,26	3,55	3,47
FeO	17,47	17,07	18,13	18,40	18,01	18,07	18,04	17,85	20,05	20,08	18,37	17,71	17,60	18,13
Total	101,61	100,38	101,07	101,27	100,47	100,31	100,13	100,70	100,19	100,63	101,11	100,72	100,31	100,29
Mg#	54,62	55,23	52,40	51,57	53,17	52,88	53,24	53,88	47,24	47,29	52,27	53,98	54,54	52,86
Cr#	60,71	59,71	62,61	62,21	57,14	57,72	55,28	56,07	57,70	57,76	59,35	60,00	57,33	57,16
TiO_2 (liquid)	0,66	0,71	0,73	0,73	0,99	0,97	0,92	0,95	1,07	0,93	0,82	0,86	0,92	0,88
Al_2O_3 (liquid)	14,52	14,57	14,35	14,38	14,92	14,83	15,20	14,99	14,77	14,79	14,73	14,63	14,90	14,91
TiO_2 (rock)	0,71				0,98				0,94					
Al_2O_3 (rock)	13,84				13,89				15,41					

Table 3 (3/3)

Locality - unit	Ashin - Pillow lavas													
Sample	AS1007/2 basalt				AS1008 basalt				AS1009 basalt					
Mineral	spl 2c	spl 2r	spl 13c	spl 13r	spl 2c	spl 2r	spl 3c	spl 3r	spl 4c	spl 4r	spl 5c	spl 5r	spl 7c	spl 7r
Mineral type	Al-Chr	Al-Chr	Al-Chr	Al-Chr	Al-Chr	Al-Chr	Al-Chr	Al-Chr	Al-Chr	Al-Chr	Al-Chr	Al-Chr	Al-Chr	Al-Chr
TiO_2	0,38	0,43	0,45	0,49	0,47	0,44	0,45	0,40	0,38	0,43	0,36	0,41	0,46	0,47
Al_2O_3	21,27	22,41	22,44	22,57	22,22	21,47	22,05	22,10	20,61	20,71	20,40	21,00	19,03	19,58
Cr_2O_3	45,55	43,13	42,56	42,08	42,85	43,71	42,95	42,27	45,87	45,70	45,02	44,41	46,77	46,16
V_2O_3	0,24	0,25	0,28	0,22	0,10	0,06	0,20	0,19	0,19	0,14	0,15	0,21	0,08	0,12
FeO	21,17	22,12	22,31	22,62	22,07	22,07	21,07	21,30	21,15	21,34	20,96	21,82	21,96	20,92
MnO	0,33	0,21	0,29	0,25	0,27	0,32	0,21	0,22	0,32	0,29	0,25	0,23	0,30	0,33
MgO	11,36	11,43	11,50	11,75	12,25	11,77	12,80	12,33	11,54	11,81	12,48	12,30	11,32	12,88
CaO	0,00	0,00	0,00	0,00	0,00	0,00	0,00	0,00	0,00	0,00	0,00	0,00	0,00	0,00
ZnO	0,00	0,02	0,02	0,10	0,02	0,03	0,00	0,01	0,03	0,06	0,03	0,02	0,05	0,04
NiO	0,06	0,06	0,06	0,09	0,10	0,07	0,10	0,07	0,06	0,01	0,08	0,05	0,17	0,14
Total	100,36	100,06	99,90	100,18	100,35	99,95	99,83	98,90	100,15	100,48	99,73	100,45	100,15	100,63
Ti	0,009	0,010	0,010	0,011	0,011	0,010	0,010	0,009	0,009	0,010	0,008	0,010	0,011	0,011
Al	0,779	0,818	0,820	0,821	0,806	0,786	0,800	0,811	0,757	0,757	0,748	0,764	0,705	0,713
Cr	1,119	1,057	1,043	1,027	1,042	1,073	1,046	1,040	1,131	1,121	1,107	1,084	1,162	1,127
V	0,006	0,006	0,007	0,005	0,002	0,002	0,005	0,005	0,005	0,004	0,004	0,005	0,002	0,003
Fe^{3+}	0,078	0,099	0,109	0,124	0,128	0,118	0,128	0,125	0,089	0,099	0,125	0,128	0,110	0,135
Fe^{2+}	0,473	0,474	0,470	0,460	0,439	0,455	0,415	0,429	0,462	0,455	0,421	0,436	0,467	0,405
Mn	0,009	0,006	0,008	0,007	0,007	0,008	0,006	0,006	0,008	0,008	0,007	0,006	0,008	0,009
Mg	0,526	0,528	0,532	0,541	0,562	0,545	0,588	0,572	0,536	0,546	0,578	0,566	0,530	0,593
Ca	0,000	0,000	0,000	0,000	0,000	0,000	0,000	0,000	0,000	0,000	0,000	0,000	0,000	0,000
Zn	0,000	0,000	0,000	0,002	0,001	0,001	0,000	0,000	0,001	0,001	0,001	0,000	0,001	0,001
Ni	0,001	0,001	0,001	0,002	0,002	0,002	0,002	0,002	0,001	0,000	0,002	0,001	0,004	0,004
Total	3,000	3,000	3,000	3,000	3,000	3,000	3,000	3,000	3,000	3,000	3,000	3,000	3,000	3,000
Fe_2O_3	3,33	4,24	4,67	5,35	5,53	5,07	5,53	5,34	3,81	4,23	5,32	5,50	4,63	5,83
FeO	18,18	18,31	18,11	17,81	17,09	17,51	16,10	16,50	17,72	17,54	16,17	16,87	17,79	15,68
Total	100,69	100,49	100,36	100,71	100,91	100,46	100,38	99,43	100,53	100,90	100,26	101,01	100,61	101,22
Mg#	52,69	52,68	53,10	54,05	56,10	54,51	58,64	57,13	53,71	54,54	57,90	56,52	53,15	59,42
Cr#	58,96	56,36	55,99	55,57	56,40	57,73	56,65	56,20	59,89	59,68	59,68	58,66	62,24	61,27
TiO_2 (liquid)	0,86	0,93	0,96	1,01	0,99	0,95	0,96	0,90	0,86	0,93	0,83	0,91	0,97	0,99
Al_2O_3 (liquid)	14,76	14,95	14,95	14,97	14,92	14,80	14,89	14,90	14,65	14,67	14,62	14,72	14,38	14,48
TiO_2 (rock)	0,98				0,95				0,91					
Al_2O_3 (rock)	15,63				15,34				13,67					

Table 4

Table 4.

Locality - unit	Nain - Sheeted dykes										Ashin - Pillow lavas	
Sample Rock type	NA537 basaltic andesite						NA538 basalt				AS1007/2 basalt	AS1008 basalt
Mineral Mineral type	am 2-5c Mhb	am 2-5r Mhb	am 10-2c Mhb	am 10-2r Mhb	am 12-1c Mhb	am 12-1r Mhb	am 4-4c Mhb	am 4-4r Mhb	am 10-9c Mhb	am 10-9r Mhb	am 8-3c Mhb	am 7-11c Mhb
SiO_2	51.08	50.69	49.99	51.02	50.77	50.71	50.15	50.56	50.89	50.17	50.07	50.30
TiO_2	0.59	1.09	0.85	1.14	0.65	0.93	0.51	0.68	0.36	0.52	1.11	2.18
Al_2O_3	6.46	7.86	7.84	8.09	8.17	7.77	8.00	7.49	8.09	8.26	11.07	11.08
FeO	9.07	10.68	10.21	10.00	10.32	10.42	12.18	12.03	12.04	11.69	8.98	8.13
MnO	0.31	0.36	0.18	0.35	0.22	0.41	0.20	0.43	0.25	0.40	0.23	0.08
MgO	16.72	14.56	14.92	14.42	14.47	14.70	14.47	14.78	14.67	14.75	14.49	14.96
CaO	11.94	10.57	11.46	10.19	10.56	10.06	10.95	10.43	10.95	10.07	10.69	10.84
Na_2O	1.11	1.31	1.02	1.22	1.09	1.49	0.57	0.53	0.52	0.71	0.75	0.62
K_2O	0.16	0.33	0.11	0.28	0.23	0.35	0.08	0.16	0.08	0.14	0.24	0.01
Cr_2O_3	0.00	0.00	0.03	0.00	0.09	0.00	0.29	0.05	0.01	0.01	0.22	0.57
NiO	0.02	0.04	0.01	0.00	0.00	0.01	0.02	0.00	0.00	0.00	0.00	0.02
Total	97.45	97.49	96.63	96.70	96.56	96.84	97.42	97.14	97.86	96.72	97.85	98.79
Fe_2O_3	3.73	4.34	3.39	4.02	4.36	5.29	8.44	10.04	8.53	10.86	5.38	5.01
FeO	5.71	6.78	7.16	6.38	6.40	5.66	4.58	3.00	4.36	1.92	4.14	3.62
Total	99.95	100.04	99.06	99.21	99.10	99.48	100.39	100.27	100.85	99.94	100.55	101.47
Si	7.224	7.182	7.154	7.244	7.226	7.201	7.076	7.114	7.125	7.058	6.966	6.910
Ti	0.062	0.116	0.091	0.121	0.069	0.099	0.054	0.072	0.038	0.055	0.116	0.225
Al (iv)	0.776	0.818	0.846	0.756	0.774	0.799	0.924	0.886	0.875	0.942	1.034	1.090
Al (vi)	0.301	0.495	0.476	0.597	0.596	0.502	0.407	0.356	0.460	0.427	0.782	0.703
Fe^{3+}	0.397	0.462	0.365	0.429	0.467	0.565	0.897	1.063	0.899	1.149	0.563	0.518
Fe^{2+}	0.676	0.803	0.857	0.758	0.761	0.673	0.541	0.352	0.511	0.226	0.482	0.416
Mn	0.037	0.044	0.022	0.042	0.027	0.049	0.024	0.051	0.030	0.048	0.027	0.009
Mg	3.525	3.076	3.183	3.052	3.069	3.112	3.044	3.100	3.062	3.093	3.005	3.064
Ca	1.809	1.604	1.757	1.550	1.610	1.531	1.655	1.572	1.643	1.518	1.594	1.595
Na	0.304	0.361	0.284	0.335	0.301	0.409	0.156	0.143	0.141	0.193	0.202	0.165
K	0.030	0.059	0.021	0.051	0.041	0.064	0.014	0.029	0.014	0.025	0.043	0.001
Cr	0.000	0.000	0.004	0.000	0.010	0.000	0.032	0.006	0.001	0.001	0.024	0.062
Ni	0.002	0.005	0.001	0.000	0.000	0.001	0.003	0.000	0.000	0.000	0.000	0.003
Total	15.143	15.024	15.062	14.937	14.952	15.004	14.825	14.745	14.797	14.737	14.839	14.761

Appendix A1. Comparison of major and trace element concentrations in reference samples analyzed using X-Ray Fluorescence spectrometry and Inductively Coupled Plasma-Mass Spectrometry, as well as detection limits for both analytical methods.

		BE-N			BHVO-1			
		Recomm.	Measured Mean Values (n=30)	Relative Error (%)	Recomm.	Measured Mean Values (n=13)	Relative Error (%)	Detection limits
X-Ray Fluorescence spectrometry (XRF)	*(wt%)*							
	SiO2	38.48	38.58	-0.3	49.94	49.57	0.74	0.05
	TiO2	2.63	2.62	0.3	2.71	2.75	-1.48	0.01
	AL2O3	10.14	9.81	3.3	13.80	14.02	-1.59	0.05
	Fe2O3	12.93	12.78	1.2	12.23	12.52	-2.37	0.10
	MnO	0.20	0.19	7.4	0.17	0.17	0.00	0.05
	MgO	13.25	13.60	-2.7	7.23	6.90	4.56	0.01
	CaO	13.97	13.73	1.7	11.40	11.52	-1.05	0.04
	Na2O	3.20	3.30	-3.0	2.26	2.36	-4.42	0.01
	K2O	1.40	1.36	2.9	0.52	0.50	3.85	0.01
	P2O5	1.06	1.00	5.4	0.27	0.25	7.41	0.01
	(ppm)							
	Zn	120	116	3.3	105	98	6.67	2
	Cu	72	73	-0.8	136	140	-2.94	3
	Sc	22	21	2.3	31.8	32	-0.63	3
	Ga	17	16	4.4	21	22	-4.76	3
	Ni	267	260	2.6	121	124	-2.48	2
	Co	60	63	-5.0	45	46	-2.22	2
	Cr	360	351	2.5	289	298	-3.11	2
	V	235	231	1.7	317	312	1.58	2
	Rb	47	47	0.2	11	10	9.09	1
	Ba	1025	999	2.5	139	145	-4.32	3
	Pb	4	n.d.		2.6	n.d.		5
	Sr	1370	1360	0.7	403	408	-1.24	2
	Zr	260	268	-3.1	179	172	3.91	2
	Y	30	28	5.3	27.6	28	-1.45	1
	La	82	79	3.7	15.8	18	-13.9	5
	Ce	152	160	-5.3	39	42	-7.69	5
	Nd	67	65	3.7	25.2	24	4.76	3
	Nb	105	105	-0.1	19	18	5.26	1
	Th	10.4	11	-2.7	1.08	1	7.41	1
Inductively Coupled Plasma-Mass Spectrometry (ICP-MS)	*(ppm)*							
	Rb				11	10.9	1.4	0.020
	Sr				403	410	-1.7	0.020
	Y				27.6	28.4	-2.8	0.003
	Zr				179	190	-6.1	0.020
	La				15.8	16.0	-1.3	0.010
	Ce				39	37.6	3.7	0.002
	Pr				5.7	5.57	2.3	0.004
	Nd				25.2	26.1	-3.7	0.002
	Sm				6.2	6.53	-5.3	0.006
	Eu				2.06	2.10	-1.9	0.002
	Gd				6.4	6.25	2.3	0.001
	Tb				0.96	0.93	3.6	0.002
	Dy				5.2	5.42	-4.2	0.001
	Ho				0.99	1.05	-6.1	0.002
	Er				2.4	2.57	-7.1	0.001
	Tm				0.33	0.32	4.5	0.003
	Yb				2.02	2.16	-6.9	0.001
	Lu				0.291	0.31	-6.9	0.005
	Nb				19	18.5	2.7	0.001
	Hf				4.38	4.29	2.1	0.001
	Ta				1.23	1.30	-5.7	0.005
	Th				1.08	1.13	-4.6	0.0015
	U				0.42	0.45	-7.1	0.002

Recommended values for international reference materials BE-N and BHVO-1 are from Govindaraju (1994, Geostandard Newsletter, Special Issue, v. 118, 158 p.). Abbreviations: Recomm. = recommended values; n.d. = not detected. Detection limits were estimated using 29 international reference standards and 3 internal standards run as unknowns.

Appendix A2

Appendix A2. Input parameters for the partial melting models used for different rock-types (see Figs. 12, 14)

	Composition of mantle peridotites and subduction-related additional components					Composition of the theoretical mantle sources calculated by the addition of various proportions of subduction-related components to depleted peridotities			
	Depleted Lherzolite EP22	Depleted Lherzolite A19	APS	Sea water		Group 1 pillow lava	Group 1 sheeted dykes	Group 2 pillow lava	Group 2 pillow lava
					Mantle peridotite	EP22	A19	EP22	A19
					Fluid Component	0.5% Sea water	0.2% Sea water	-	-
					Melt Component	-	0.1% APS	0.5% APS	0.5% APS
La	0.026	0.018	38	5.6		0.054	0.067	0.216	0.207
Ce	0.090	0.059	80	1.6		0.098	0.142	0.490	0.459
Pr	0.024	0.013		0.87		0.028	0.015	0.023	0.013
Nd	0.179	0.106	32	4.2		0.199	0.146	0.327	0.265
Sm	0.097	0.055	5.6	0.84		0.100	0.063	0.118	0.083
Eu	0.047	0.030	1.1	0.21		0.048	0.031	0.052	0.035
Gd	0.221	0.148	4.7	1.3		0.227	0.155	0.244	0.171
Tb	0.051	0.031	0.77	0.21		0.051	0.032	0.060	0.035
Dy	0.384	0.246		1.5		0.390	0.248	0.382	0.245
Ho	0.098	0.060		0.45		0.100	0.060	0.098	0.059
Er	0.300	0.183		1.3		0.305	0.185	0.298	0.182
Tm	0.052	0.032	0.4	0.25		0.052	0.033	0.053	0.034
Yb	0.320	0.214	2.8	1.5		0.326	0.219	0.333	0.227
Lu	0.054	0.035	0.43	0.32		0.055	0.036	0.055	0.037
Cr	2580	2464				2580	2464	2580	2464
Y	2.12	1.66				2.17	1.70	2.22	1.76

Source mode: ol 0.65 - opx 0.28 - cpx 0.06 - spl 0.08

Melting proportions: ol 0.1 - opx 0.64 - cpx 0.25 - spl 0.02

Partition coefficients. REE: McKenzie and O'Nions (1991); Y: Ulmer (1989); Cr in ol, opx, cpx: Ewart et al. (1973); Cr in spl: Klemme et al. (2006)

Abbreviations, ol: olivine; opx: orthopyroxene; cpx: clinopyroxene; spl: spinel; REE: rare earth elements. The compositions of lherzolites EP22 and A19 are from Saccani et al. (2017). The compositions of average pelitic sediments (APS) and sea water are from Taylor and McLennan (1985) and Li (2000), respectively. Source mode and melting proportions are from Kostopoulos and

References

Ewart, A., Bryan, W.B., Gill, J.B., 1973. Mineralogy and Geochemistry of the Younger Volcanic Islands of Tonga, S.W. Pacific. Journal of Petrology 14, 429-465.

Klemme, S., Gunther, D., Hametner, K., Prowatke, S., Zack, T., 2006. The partitioning of trace elements between ilmenite, ulvospinel, armalcolite and silicate melts with implications for the early differentiation of the moon. Chemical Geology 234, 251-263. doi: 10.1016/j.chemgeo.2006.05.005.

Kostopoulos, D.K., Murton, B.J., 1992. Origin and distribution of components in boninite genesis: significance of the OIB component. In: Parson, L.M., Murton, B.J., Browning, P. (Eds.), Ophiolites and their modern oceanic analogues: Geological Society of London, Special Publication 60, pp. 133-154.

Li Y.H., 2000. A Compendium of Geochemistry: from Solar Nebula to the Human Brain. Princeton University Press, Princeton, NJ.

McKenzie, D., O'Nions, R.K., 1991. Partial melt distributions from inversion of rare earth element concentrations. Journal of Petrology 32, 1021-1091.

Saccani E., Dilek Y., Photiades A., 2017. Time-progressive mantle-melt evolution and magma production in a Tethyan marginal sea: A case study of the Albanide-Hellenide ophiolites. Lithosphere 10, 35-53. https://doi.org/10.1130/L602.1.

Taylor, S.R., McLennan, S.M., 1985. The Continental Crust: its composition and evolution: an examination of the geochemical record preserved in sedimentary rocks. Oxford, Blackwell Scientific Publication, 312 pp.

Ulmer, P., 1989, Partitioning of high field strength elements among olivine, pyroxenes, garnet and calc alkaline picrobasalt: experimental results and an application. International Journal of Mass Spectrometry and Ion Physics, 42-47.